2007-08-28

# Optimization of Control Source and Error Sensor Locations in Free Field Active Noise Control

Connor Raymond Duke
*Brigham Young University - Provo*

# OPTIMIZATION OF CONTROL SOURCE AND ERROR SENSOR LOCATIONS IN FREE FIELD ACTIVE NOISE CONTROL

by

Connor R. Duke

A thesis submitted to the faculty of

Brigham Young University

in partial fulfillment of the requirements for the degree of

Master of Science

Department of Physics and Astronomy

Brigham Young University

December 2007

BRIGHAM YOUNG UNIVERSITY

GRADUATE COMMITTEE APPROVAL

of a thesis submitted by

Connor R. Duke

This thesis has been read by each member of the following graduate committee and, by majority vote, has been found to be satisfactory.

| | |
|---|---|
| _____ | _____ |
| Date | Scott D. Sommerfeldt, Chair |
| _____ | _____ |
| Date | Kent L. Gee |
| _____ | _____ |
| Date | Scott L. Thomson |

BRIGHAM YOUNG UNIVERISTY

As chair of the candidate's graduate committee, I have read the thesis of Connor R. Duke in its final form and have found that (1) its format, citations, and bibliographical style are consistent and acceptable and fulfill university and department style requirements; (2) its illustrative materials including figures, tables, and charts are in place; and (3) the final manuscript is satisfactory to the graduate committee and is ready for submission to the university library.

_____ _____

Date

Scott D. Sommerfeldt
Chair, Graduate Committee

Accepted for the Department

_____ _____

Date

J. Ward Moody, Graduate Coordinator
Department of Physics and Astronomy

Accepted for the College

_____ _____

Date

Thomas W. Sederberg, Associate Dean
College of Physical and Mathematical Sciences

# ABSTRACT

## OPTIMIZATION OF CONTROL SOURCE AND ERROR SENSOR LOCATIONS IN FREE FIELD ACTIVE NOISE CONTROL

Connor R. Duke

Department of Physics and Astronomy

Master of Science

Previous work has shown that active noise control (ANC) can be applied to axial cooling fans. Optimization of the control source and error sensor placement is desired to maximize the attenuation using ANC. A genetic algorithm was developed to find the optimal placement of control sources for a given primary source. The optimal configuration of control sources around a single primary source was shown to be a linear arrangement of the sources. This holds true for both two-dimensional as well as three-dimensional configurations. The higher-order radiation of the linear arrangement has also been verified experimentally, but the improvement in the experimental apparatus was not as dramatic as the theoretical model. Multiple flow visualization techniques have been used to find optimal near field error sensor locations. When there is little obstruction to the flow field of the fan, minimal airflow is found along the near field null that is created by minimizing the sound power of the system. Surface mounting of the

error sensors can lead to a small increase in the signal-to-noise ratio of the error sensors if vortices exist in the near field of the fan due to obstructions in the main flow. It has also been shown that the introduction of the ANC system does not affect the flow field of the fan.

# ACKNOWLEDGMENTS

I would like to sincerely express my gratitude to the following people for their support and guidance through this work. This work would not have been accomplished without:

- Scott D. Sommerfeldt, for his mentoring and guidance in this research as well as in my goals and career choice
- Kent L. Gee, for his genuine concern and hard-work in the completion of this research
- Scott L. Thomson, for his patience and sacrifice in teaching me the techniques used in this research
- Timothy W. Leishman, for his deep interest in my education
- Brian B. Monson, Benjamin M. Faber, and Matthew J. Green for their time and concern in teaching me
- Cole V. Duke for his eternal friendship and his help every step of the way
- Benjamin M. Schafer for his sincerity and enthusiasm
- David W. Krueger for his diligence to learn and work
- The BYU Acoustics Research Group for their support
- Diann Sorensen and Nan Ellen Ah You for their helpful administration
- Mikila for her love, support, and companionship
- Jon, Shauna, Clint, Amy, Carl, Mary Ann, and Lacey Duke for their support

## TABLE OF CONTENTS

## LIST OF TABLES

### Chapter 5



### Chapter 6

## LIST OF FIGURES

**Chapter 1**



**Chapter 2**



**Chapter 3**

**Chapter 4**



**Chapter 5**

**Chapter 6**

**Appendix 2**

# Chapter 1

# Introduction

## 1.1 Background

### 1.1.1 Fan Noise

Active noise control (ANC) of computer fan noise has emerged as an area of increasing interest in the past 10 to 15 years because of the growing use of personal computers at home and in the workplace. With computers becoming faster and processors becoming hotter, more fan-driven heat dissipation is needed. This often results in a louder cooling system. Other consumer electronics have followed similar trends.

Numerous studies have been performed to understand the noise radiation mechanisms in air moving devices.[1-5] Monopole and dipole sources caused by blade thickness noise and blade forces have been found to be the two major sources of discrete noise emissions.[6, 7]

Control of the sound emissions from air moving devices has taken many different approaches. Passive control through duct linings and fan shapes has been the most common approach.[8, 9] These passive methods of noise control tend to be more effective at higher frequencies. Speed control can also be an effective way to reduce noise emissions when the full capability of the fan is not needed.[10] Installation effects have also been a large area of research. Acoustically transparent fan testing plenums have become common to test the noise emissions at different operating points.[2, 11, 12] Enclosure modifications have been shown to be effective in controlling operating points of air moving devices.[13, 14] While the effectiveness of passive noise control is limited by

frequency range, available space, or cost, active noise control can potentially be used to further reduce noise emissions from air moving devices.

### 1.1.2 Active Noise Control

The noise emissions from typical air moving devices are characterized by a broadband noise floor with blade passage frequency (BPF) related discrete components above the broadband noise floor. Feed-forward ANC can be used to control the discrete components of the spectrum using the rotation of the fan as a reference. Feedback control is most often used to control the broadband component of the emitted fan noise.

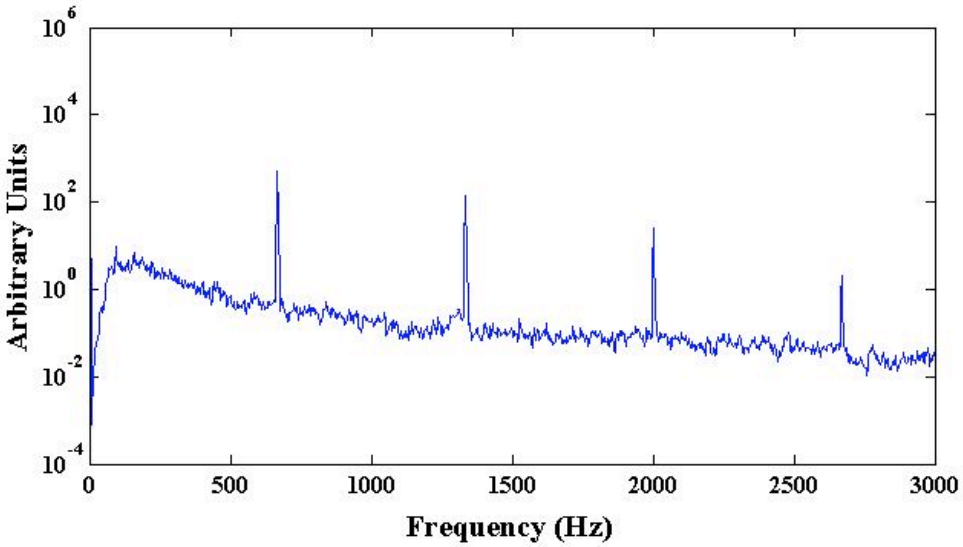


**Figure 1.1 Typical fan noise spectrum**

Global free-field ANC is implemented by changing the radiation impedance of the primary source by using secondary sources. In the case of fan noise, the fan is the primary noise source. Secondary or control sources are placed in the near field and driven to create a mutual impedance upon the primary noise source. The mutual impedance on one source due to another source is

$$Z(kd) = \frac{jk^2\rho_o c}{4\pi}\left(\frac{e^{-jkd}}{kd}\right), \tag{1.1}$$

where $k$ is the wavenumber, $d$ is the distance between the two sources, $\rho_o$ is the density of the radiation medium, and $c$ is the speed of sound in the medium. The self impedance is found by letting $kd \to 0$, giving:

$$Re[Z_\phi] = \frac{k^2 \rho_o c}{4\pi} . \tag{1.2}$$

The total radiation impedance of a single source becomes the sum of the self impedance and mutual impedance from each of the other sources.

$$Z_{tot} = Z_\phi + \sum_n Z_n(kd_n) \tag{1.3}$$

The radiation impedance "seen" by the fan will dictate the noise emission from the fan into the far field, since the radiated sound power is proportional to the real part of the radiation impedance.[15]

Source strengths of each control source can be found to minimize the radiated sound power of the entire system.[15, 16] The minimized sound power field will depend upon the number of control sources, the configuration of the sources, and frequency. In application, a reference signal and error sensors dictate the complex source strengths of the control sources. A reference signal is used to identify the noise emission from background components. Through the use of an adaptive algorithm, the source strength of the control sources are optimized relative to the reference signal to obtain the desired error signal.

The amount of far field control achieved is constrained by various parameters of the system. Optimization of various parameters of the overall system will not have a uniform effect on the overall attenuation achieved. This concept is illustrated by Snyder[17] in Figure 1.2. However independent optimization of the physical control source

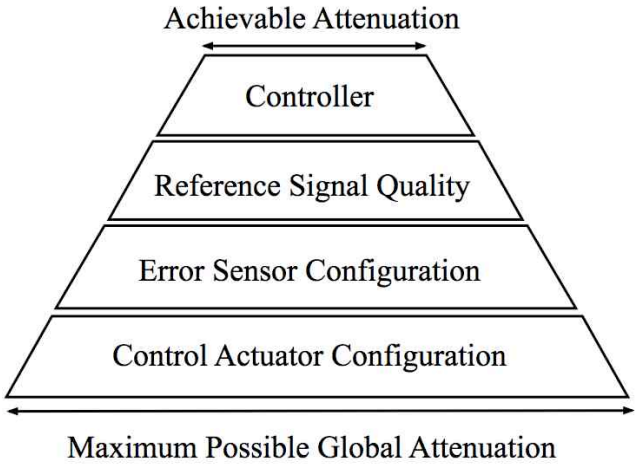


**Figure 1.2 Limiting factors in active noise control[17]**

configuration will result the greatest increase in achievable attenuation. Once the optimal control source configuration has been achieved, the error sensor placement in turn will usually become the limiting factor in the overall achievable attenuation.

### 1.1.3 Applications of ANC to Air Moving Devices

Numerous groups have shown that active noise control can be used to reduce the noise emissions from air moving devices. Various control techniques have been successfully used on different types of air moving devices. For example, Neise[18] and Koopman[19] showed that active noise control can be used to attenuate noise radiation from a centrifugal blower. In their research, control actuators were used to control the radiation of the blower into a duct. The BPF and harmonics were significantly reduced throughout the duct. Quinlan's[20, 21] work with an axial fan also showed significant far field reduction of the BPF and harmonics using one control source in the near field of the axial fan. Wang *et al.*[22] and Gerard *et al.*[23] showed similar results in a similar setup. In their study significant sound power reduction of the tonal components of the axial fan were achieved.

Alternatives to using loudspeakers as control sources have also been investigated. Lauchle *et al.*[24] used the fan as the actuator. In this study, a shaker was attached to the fan hub allowing the fan blades to be moved. Attenuation of the BPF as well as the harmonics were achieved by allowing a filtered-X algorithm to control the movement of the fan. In a second variation, air jets near the blade tip clearance were used to control the flow around the blade tips in a study by Schulz *et al.*[25] These jets were used as aeroacoustic sources to suppress the discrete noise emissions. Reductions were achieved on the BPF and harmonics, as well as high-frequency broadband levels.

Multichannel global control has also been studied by many groups. Gee and Sommerfeldt[26-28] showed that the BPF and harmonics can be globally controlled by use of multiple control sources in the near field of an axial fan. Near field error placement was also investigated to compress the size of the system. Similar results were observed by Monson and Sommerfeldt[29] using smaller fans in a reverberant sound field. Feedback active noise control was shown to attenuate the BPF and harmonics in a study by Green and Sommerfeldt.[30] Modest low frequency broadband reduction was also achieved using the feedback controller technique.

### 1.1.4 Fan Source Localization

To adequately model the fan for theoretical analysis, noise sources of the fan must be identified and located, to identify discrete components of the radiated noise. Theoretically, optimal control source placement and error sensor placement are both dependent upon the source characteristics of the fan noise. In previous research, error sensor placement has been determined by modeling the discrete noise radiation from a fan as a monopole.[26, 29] This may not be a valid model in all cases, but various studies

have yielded significant results. Monopole radiation characteristics will be assumed for this research, as has been previously accepted.

### 1.1.5 Control Source Placement

Control source placement can be a physically limiting parameter in an active control system. As a general rule, the closer a control source is to the primary source relative to a wavelength, the more attenuation can be achieved.

When a single control source is used, the distance between the primary and control source is minimized to maximize attenuation at a given frequency. When more than one control source is used, the traditional approach employs a symmetric array of control sources. Each control source is placed at a characteristic distance, $d$, from the primary source. A constant characteristic distance allows for analytical solutions of the achievable attenuation to be a function of $kd$, where $k$ is the wavenumber. for a specified number of control sources. The maximum attenuation for symmetric configurations of control sources around a single primary source can be seen in Figure 1.3.

These curves give the absolute bound on the achievable attenuation for the symmetric control source configuration.[16] These are not necessarily the absolute bounds for the specified number of control sources, they are only the bounds for the symmetrically configured case and sources in two-dimensions. Finding the optimal control source configuration depends on the distance between each source, primary and control. Many variables as well as the nature of the control source optimization function will yield many locally optimal configurations.

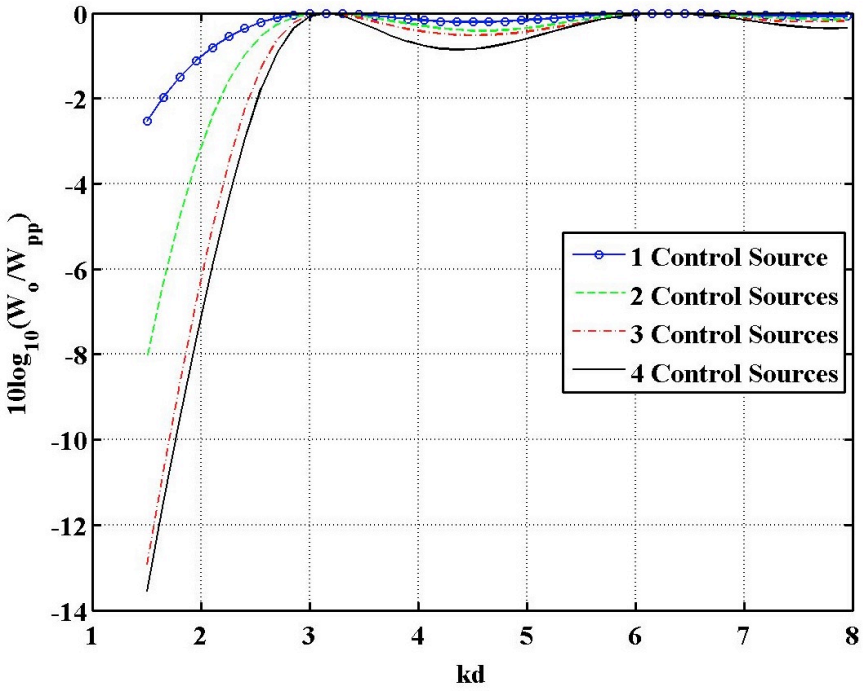


**Figure 1.3 Maximum sound power attenuation for multiple control sources in a symmetric configuration[31]**

To overcome the tendency of finding a local optimum in control source optimization using a gradient descent method, genetic and simulated annealing algorithms have been used. These algorithms can effectively search a large design space for the global optimum solution. Genetic and stimulated annealing algorithms use a model, similar to that in a natural selection environment, to find the "fittest" design in a model.[32] The "fittest" design, in this case, is the control source configuration that will give the most attenuation for a specified number of control sources.

Genetic algorithms have been used for this purpose in many different active noise and vibration control applications.[33] In vibration control, the primary sources may be distributed over a large area. In a study by Wang,[34] far field sound radiation from a simply supported beam was optimized by using a genetic algorithm. Not only was the position of the control sources studied, but the number of control sources and microphones was also researched. The use of the genetic algorithm converged to better

solutions than arbitrarily selected positions. Work done by Howard *et al.*[35] showed good results from genetic algorithms in finding locations, stiffnesses, and masses of tuned mass dampers and Helmholtz resonators in a vibro-acoustic system. They also compared the convergence of binary and integer representations of the design configurations. Martin and Roure[36] were able to achieve attenuation of an electronic transformer by the optimization of control source locations in the near field of the primary source. In their research, control was achieved in a free field using discrete control source locations.

Extensive work has also been done using genetic algorithms for control source and error sensor location placement in enclosed sound fields. Pottie and Botteldooren[37] worked on location of control source placement within a duct. A cylinder with a floor, similar to that of a commercial airplane cabin, is a frequently studied enclosed sound field using genetic algorithms. Many groups have achieved favorable results using a genetic algorithm approach for the cylinder with a floor because of the high number of possible of configurations.[38-42] Li and Hodgson[43] have also shown that genetic algorithms can include boundaries with arbitrary impedances with the introduction of image sources. In their study, the potential acoustic energy in a room was minimized by the optimization of control source locations using a genetic algorithm. Reasonable results were achieved with a limited number of image sources.

Multiple groups have done studies on the types of genetic algorithms that can be used for discrete variable control source placement.[44-46] Various kinds of genetic algorithms were studied and found suitable for active noise control applications. The speed and accuracy of convergence is largely dependent upon the user-defined

parameters of the algorithm. The optimal parameters may vary for each specific application of the algorithm.

### 1.1.6 Error Sensor Placement

Once control source location has been optimized, error sensor location will usually become the limiting factor in reaching the optimal achievable level of attenuation. The control algorithm is based upon minimizing an acoustic quantity only at the error sensors. If the error sensor positions are not optimized, the actively controlled sound field may not be a field with optimal attenuation. Optimization of error sensor placement was shown to be important in a study by Zander and Hansen.[47]

Far field radiation from a source will usually be more spatially uniform than the near field. For this purpose, error sensors are usually placed in the far field of the primary source. However, locating error sensors in the far field of the primary source is not always practical.

Various studies have shown that genetic algorithms can be used to optimize error sensor placement.[22, 34, 38-41] Even though these studies used discrete placement, this is not necessary. Error sensor placement can be optimized over a continuous interval rather than discrete positions.

Strategies using near field sensors were shown to be feasible by Berry *et al*.[48] Gee and Sommerfeldt[26-28] showed that optimal near field error sensor location can be found by mapping the minimized pressure field. The minimized pressure field for many multi-channel active noise control applications has near field pressure nulls. If error sensors are placed in the location of these near field pressure nulls, the control algorithm will drive the pressure at these points to a minimum and recreate the minimized pressure field.

Having the error sensors in the near field has a practical application advantage of allowing the system to be compact but introduces other concerns. In the application of active noise control to an axial-flow fan, the flow field must also be considered. The flow field can introduce flow-induced noise into the error signal. This flow-induced noise will not be correlated to the reference signal and will provide a bound on the achievable attenuation. The signal to noise ratio, $SNR(\omega)$, is related to the coherence of the signal at the error sensor to the reference signal, $\gamma_{er}$ by

$$SNR(\omega) = \frac{\gamma_{er}^2(\omega)}{1-\gamma_{er}^2(\omega)}. \tag{1.4}$$

The coherence will limit the amount of control that can be achieved. The ratio of the power spectral density of the error signal with control $S_c(\omega)_{\min}$ (linear scale) and the power spectral density of the error signal with no control $S_n(\omega)$ (linear scale) [15] is related to the coherence, $\gamma_{er}$, by

$$\frac{S_c(\omega)_{min}}{S_n(\omega)} = 1-\gamma_{er}^2(\omega). \tag{1.5}$$

Locating the error sensors as close to the primary source as possible will allow for a compact system but may result in increased flow-induced noise giving rise to a higher signal to noise ratio. The optimal error sensor location will depend upon the interaction of these seemingly two competing goals of maximizing signal to noise ratio and keeping the system compact.

## 1.2 Objectives

The research developed in this thesis will focus on optimizing the control source configuration as well as the error microphone placement for an axial cooling fan. Two cooling fans were chosen to represent two notably different fan types of similar size.

### 1.2.1 Control Source Optimization

The optimization of the control sources is important to get the most attenuation from a system as possible. Since the control source configuration will give a physical limit on the amount of control that can be obtained, optimizing the control source configuration may be the most important parameter to optimize in an active control system. To optimize the control source configuration, the following questions will need to be addressed:

- What types of genetic algorithms will work best to find the optimal control source configurations?
- Will the algorithm converge to a single solution in a reasonable number of generations?
- Is the symmetric control source configuration optimal when constrained to two dimensions?
- If the symmetric control source configuration is not optimal, what is the best configuration?
- Is the optimal control source configuration strongly frequency-dependent?
- If the configuration is allowed to expand into three dimensions, will the optimal configuration change dramatically?
- Do the experimental data confirm the optimal control source configuration?

- Will the optimal control source configuration change dramatically when the active noise control system is placed near a reflective surface?

The answers to these questions will lead to better understanding of the optimization of the control source configuration.

### 1.2.2 Error Sensor Optimization

The error sensor optimization that will be presented in this research will use optimization done in previous research as a basis. Error sensors will be constrained to the near field to keep the ANC system compact in size. Feasible positions in the near field will be based on research performed by Gee and Sommerfeldt.[26-28] Two characteristic fans of the same size, with some notable differences, will be used to yield more general information about near field flow effects. Information from these two fan configurations will allow us to optimize error sensor location by answering the following questions:

- Is the flow field of the two fans appreciably different?
- Are there better positions along the near field pressure nulls due to flow-induced noise?
- What is the speed of the airflow from the fans in the near field of the fan?
- Is the flow in the near field of the fan highly turbulent, causing flow-induced noise?
- Will placing the error sensors farther from the fan keep the error sensors outside of the majority of the airflow?
- Will surface mounting the error sensors change the effect of turbulence on the error sensors?

While answering these questions relating to the flow field of the fan, the effects of ANC on the flow of the system will also be investigated. Because air-moving devices' primary

function is dependent on the flow field they create, any changes in the flow field due to ANC should be considered if the ANC system is to be realistically implemented.

### 1.3 Limitations in Scope

The results and experimental verification will not be comprehensive in this study. Limitations on this research are based on time and experimental setup limitations. These limitations are listed below.

#### 1.3.1 Control Source Optimization

Optimization of control source placement is dependent upon the primary source distribution and number. Because of the large number of possible primary source configurations, control source optimization will only be done for a limited number of primary source configurations. The single primary source, or single axial fan, is a popular cooling technique and will be the primary source configuration that will be most thoroughly investigated. The single primary source will also be the configuration used in the investigation of primary sources near reflective surfaces. Multiple primary sources will be investigated briefly but will not be thoroughly presented.

Installation of air-moving devices can be done in a variety of ways. A common technique is to use the air-moving device at the edge of the enclosure or plenum that is need of cooling. In the case of axial fans, the fan will be placed on a side of the enclosure and used to produce a pressure drop, and corresponding airflow. The mounting of an axial fan on the surface makes the mounting of control sources on the same surface easily implemented. To keep the mounting of control sources as straightforward as possible, the control source configuration will be constrained to two dimensions. Reductions in

sound power radiation may be improved by optimizing in three dimensions, but the resulting configuration may have limited practical application.

### 1.3.2 Error Sensor Optimization

Limitations in the error sensor optimization are based mostly on the equipment available during the study. The most significant of these limitations is the time resolution that can be achieved by the laser used in the particle image velocimetry (PIV) measurements. The laser used in this study is limited to 5 pulse pairs per second. This resolution in time will allow for quantitative measurements in time, but will not provide detailed information about the phase-dependent evolution of the flow.

The investigation of the flow field will also include limitations to two dimensions. Even though measurements will be taken in a plane parallel to the mounting of the fan as well as normal to this plane, three-dimensional images will not be created from the two-dimensional data. Even though the full characterization of the flow field from the fans used in this research is important, only limited studies on the turbulence of the flow will be necessary to answer the questions posed about the error sensor placement.

For the turbulence calculations to be meaningful, assumptions about the time harmonicity of the fan flow need to be made. The low time resolution of the PIV system will not allow for a measurement to be taken every revolution of the fan. If the fan is assumed to (1) have blades that are uniformly spaced and (2) have time harmonic flow, then measurements of the airflow can be triggered using the BPF with a low time resolution. These two assumptions were adopted in this study. Even though uniform blade spacing may be a reasonable assumption, this is not always the case in real-world applications and can lead to inadvertent time averaging.

## 1.4 Organization of Thesis

Chapter 2 consists of a more detailed discussion on how genetic algorithms are used in control source optimization and how genetic algorithms were implemented in this research. Chapter 3 introduces the methods used to investigate the flow field from the characteristic fans used and the relationship of the flow field to the error sensor optimization. The methods used in the active noise control will be discussed in Chapter 4. Results from the control source optimization and the error sensor placement will be in Chapters 5 and 6, respectively. Chapter 7 will outline the conclusions from the study as well as recommendations for further study. Error analysis of this study will be available in the appendices.

# Chapter 2

# Genetic Algorithm Methods

## 2.1 Introduction

In many optimization problems, gradient-based optimization techniques cannot be used because of various limitations. Some of these limitations include discrete values for the optimization variables, non-differentiable functions in the optimization, a large number of optimization variables, or local minima, maxima, and saddle points. In these cases, gradient-based optimization will find optimal solutions that are strongly dependent upon the starting design but may not be indicative of the global optimum.[49]

When gradient-based methods are not available, other options for optimization include exhaustive search, simulated annealing, branch and bound, and genetic algorithms. Exhaustive search will always be effective but will usually require too many resources. Simulated annealing and branch and bound can be effective for discrete variable optimization but will be inferior to genetic algorithms, except in isolated cases.[49]

Genetic algorithms simulate a natural selection environment in the optimization variable space. First, combinations of the optimization variables are randomly selected and a new set of combinations are created based upon the first group, and the process is then repeated. Characteristics of the previous group are passed to the next group based on how the characteristics affect the optimization goal. Each combination of optimization variables is called a "chromosome" and each individual variable is called a "gene" in that chromosome. A group of chromosomes is called a "generation". The quality, or fitness, of each chromosome is based upon the optimization function(s). Each generation goes through a four-step process illustrated in Figure 2.1. The algorithm

simulates a natural selection environment to find the optimal or "most fit" design in the optimization variable space.

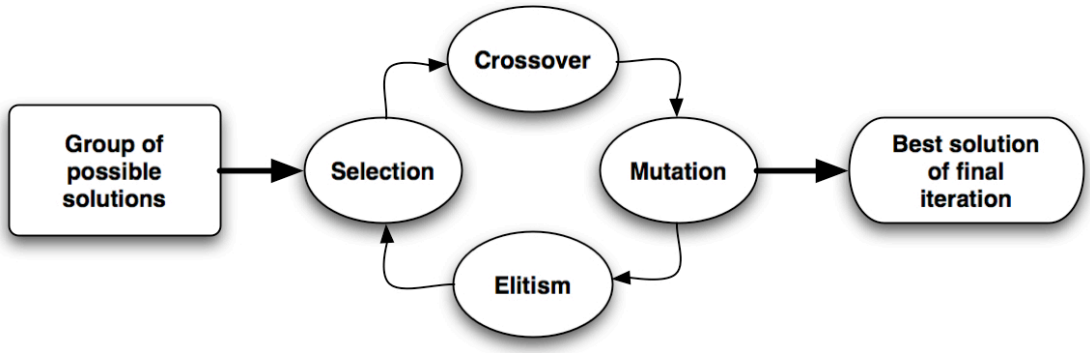


**Figure 2.1 Flow chart of a typical genetic algorithm**

## 2.2 Genes, Chromosomes and Generations

### 2.2.1 Genes

The variables of the optimization problem each constitute a single gene in the genetic algorithm. In many cases genetic algorithms are used because the optimization variable(s) is/are discrete. This is the case for many of the groups that have used genetic algorithms in ANC. Using a binary representation can be effective but will be limited in resolution by the number of discrete bits used in the representation and the size of the continuous interval. However, discrete variables are not necessary in a genetic algorithm. Continuous variables can also be made to become discrete by using a binary representation of the continuous interval.

### 2.2.2 Chromosomes

A set of specific values for each variable in the optimization problem constitutes a single chromosome. If more than a single variable exists in the optimization problem,

each variable will be represented in the chromosome. Each chromosome is a possible solution to the optimization problem.

### 2.2.3 Generations

Multiple chromosomes are placed into a group, or generation. Each generation will be used to create new chromosomes that will have some similar traits to those of the previous generation. Only computational resources limit the generation size.

### 2.2.4 Implementation of Chromosomes

The optimization of control source placement could be set up in a number of ways. In this implementation, the variables of the genetic algorithm, or the genes, are the locations of each control source. For cases in which two-dimensional optimization was performed, the location of each control source is indicated using two genes. The position is on a continuous interval specified by the user. The locations of image sources are identical to control sources, but are based upon the position of the original control sources and boundaries of the system. The number of control sources is not an optimization variable, but instead is set by the user to avoid the algorithm using more sources than is practical. All possible control source arrangements, for a specified number of control sources, can be represented by the complete set of chromosomes.

## 2.3 Fitness

Each chromosome is only as good as the amount of attenuation that can be achieved by the system. The fitness, or how fit a chromosome is, is based upon the amount of attenuation that is theoretically possible. The attenuation is found by comparing the sound power output of the system with no control sources to the sound

power output of the system with the control sources at optimal source strength. The sound power output of the system is based on (1)the frequency of interest, (2)the distance between each source in the system, and (3)the complex source strength of each of the sources. The frequency of interest is input by the user of the algorithm. The distance between each source in the system is unique to each chromosome. Unique distances for each chromosome will define unique complex source strengths for each of the control sources to minimize sound output.

The complex source strength for each control source is found by minimizing the radiated sound power of the system. The source strength can be found if the mutual impedance and self impedance of each control source and primary source in the field is known. The mutual impedance of source one on source two or vice versa is

$$Z_{12} = \frac{k^2 \rho c}{4\pi}\left[\frac{sin(kd_{12})}{kd_{12}} + j\frac{cos(kd_{12})}{kd_{12}}\right] \tag{2.1}$$

where $k$ is the wave number, $\rho$ is the density of air, $c$ is the speed of sound in air, and $d_{12}$ is the distance between the two point sources.[15,16,50] The self impedance is found by using $d_{11} = d_{22} \to 0$.[50] This gives a self impedance of

$$Re\left\{\hat{Z}_{11}\right\} = Re\left\{\hat{Z}_{22}\right\} = \frac{k^2 \rho c}{4\pi} \tag{2.2}$$

$$Im\left\{\hat{Z}_{11}\right\} = Im\left\{\hat{Z}_{22}\right\} = \frac{1}{ka}. \tag{2.3}$$

The impedance of each primary source can be described using a matrix $\hat{\mathbf{Z}}_{pp}$ for convenience. The size of $\hat{\mathbf{Z}}_{pp}$ is an M x M matrix where M is the number of primary sources in the system. The same can be done for the control sources where $\hat{\mathbf{Z}}_{cc}$ is an N x

N matrix where N is the number of control sources. The mutual impedance of each primary and control source is described by the M x N matrix, $\hat{\mathbf{Z}}_{pc}$. Using the notation

$$\mathbf{A} = \frac{1}{2} Re\left\{\hat{\mathbf{Z}}_{cc}\right\}, \tag{2.4}$$

$$\mathbf{B} = \frac{1}{2} Re\left\{\hat{\mathbf{Z}}_{pc}\right\}\hat{\mathbf{Q}}_{p}, \tag{2.5}$$

$$\mathbf{C} = \frac{1}{2}\hat{\mathbf{Q}}_{p}^{H} Re\left\{\hat{\mathbf{Z}}_{pp}\right\}\hat{\mathbf{Q}}_{p}, \tag{2.6}$$

where $\hat{\mathbf{Q}}_{p}$ is the vector of the complex source strengths of the primary sources and the superscript *H* denotes Hermitian transpose, the complex source strength of the control sources can be found.[50] This is done by minimizing the radiated power, giving the equation

$$\hat{\mathbf{Q}}_{c} = -\mathbf{A}^{-1}\mathbf{B}. \tag{2.7}$$

The radiated power of the system with only the primary sources is

$$W_{p} = \frac{1}{2}\hat{\mathbf{Q}}_{p}^{H} Re\left\{\hat{\mathbf{Z}}_{pp}\right\}\hat{\mathbf{Q}}_{p} = C, \tag{2.8}$$

and the power radiated from the system with the introduction of the control sources is

$$W_{radiated} = \mathbf{C} - \mathbf{B}^{H}\mathbf{A}^{-1}\mathbf{B}. \tag{2.9}$$

The radiated power with the control sources at their optimal source strength is used as the fitness in the genetic algorithm. The control source configuration that will give the smallest radiated sound power will be the best configuration.

### 2.4 Selection

The creation of a new generation begins with choosing a set of chromosomes to compose the new generation. Not all of the existing chromosomes will be used because their fitness will be inferior to other designs. On the other hand, a wide variety of designs must to be used to keep the population diverse. Increased diversity will allow the algorithm to find the global minimum rather than a local minimum. Two major ways of accomplishing selection are tournament and roulette-wheel selection.[49]

#### 2.4.1 Tournament Selection

Tournament selection takes a random subset, or tournament, of the existing population and selects the best design out of the subset. The chromosomes with better fitness scores will win more tournaments and will be used more often in the creation of a new generation of chromosomes.

The size of the tournaments is a user-defined parameter that will affect the diversity of the next generation. The larger the tournament size, the more the fitness of each chromosome will effect the next generation. If the tournament size is relatively small, the next generation will be less affected by the fitness of each chromosome, and will thus be a more random sample of the existing generation. The benefit of having a smaller tournament size is the higher diversity of the generation. If the tournament size is too small, the best chromosomes will have less opportunity to pass characteristics to the next generations and the convergence can take much longer.[49]

#### 2.4.2 Roulette-Wheel Selection

Roulette-wheel selection uses multiple random selections from the current generation to choose the next generation. The probability of being randomly selected is

related to the fitness, such that the higher the fitness score of a chromosome, the higher the probability of being selected. Each chromosome is assigned a scaled fitness based on the summation of the fitness of the entire generation, $\Lambda$. The fitness of each chromosome $F_i$ is related to the fitness of the generation as a whole by

$$\Lambda = \sum_i F_i \,. \tag{2.10}$$

The scaled fitness of each chromosome, $\Gamma_i$, is obtained by dividing the fitness by the fitness of the generation as a whole, according to

$$\Gamma_i = \frac{F_i}{\Lambda} \tag{2.11}$$

with the characteristics

$$\sum_i \Gamma_i = 1 \tag{2.12}$$

$$0 < \Gamma_i < 1. \tag{2.13}$$

The user can then determine how much pressure the fitness has on the subinterval, $I_i$,

$$I_i = \left(\frac{1}{\Gamma_i}\right)^{\gamma} \tag{2.14}$$

through a user-defined parameter $\gamma$.[49] Each chromosome has a fitness-related subinterval. A random number is generated between the interval of zero and the sum of all of the subintervals that corresponds to a single chromosome. The next generation of designs will be randomly selected, but will be influenced by the fitness to choose the more fit chromosomes. This will allow the generation to be diverse while allowing the algorithm to converge to the global minimum.

## 2.5 Crossover

After the selection process, a new generation can be created from the selected designs. This process is called crossover. Crossover must allow the new generation to keep characteristics of the designs chosen in the selection process. The type of crossover used usually depends on the nature of the optimization variables. If the optimization variables are converted to a binary representation, the crossover techniques are different than those for continuous-range variables. The most common types of crossover are:[49]

1. Single or double point crossover,
2. Uniform crossover, and
3. Blend crossover

For reasons described below, these types of crossover were not effective in this application. A new type of crossover, which we refer to as "parthenogenesis", was developed to overcome the shortcomings of the previous methods when applied to this application.

### 2.5.1 Single or Double Point Crossover

Single or double point crossover is generally used for discrete-value or binary-based chromosomes. The implementation of the single point crossover technique is performed by choosing a random integer corresponding to the number of genes in the chromosome. The two chromosomes selected as parents, during the selection process, are split at the point corresponding to the random integer. The two split chromosomes then interchange sections of the chromosomes as illustrated in Figure 2.2. The resulting two chromosomes have inherited characteristics of each parent chromosome but also

have significant differences. A double point crossover uses two points of crossover similar to the single point crossover.[49]

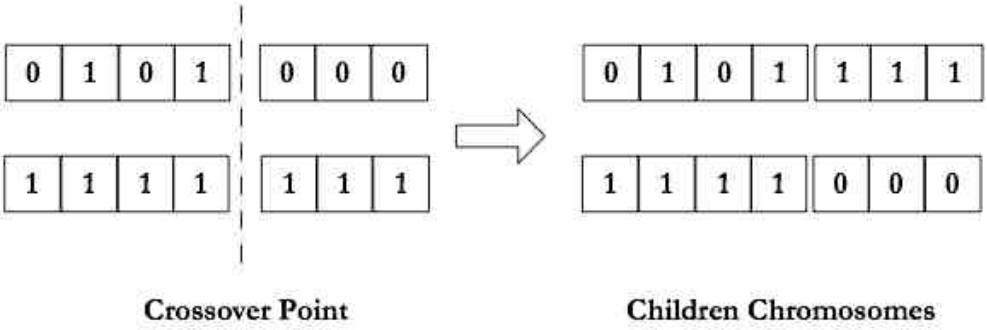


**Figure 2.2 Single point crossover for seven-gene chromosomes**

### 2.5.2 Uniform Crossover

Uniform crossover is another technique that is effective when used for discrete-valued or binary chromosomes. It is similar to single and double point crossover but can have more than two crossover points. In this technique, each gene of the set of two parents is either unchanged or switched. A random number is drawn for each gene. If the resulting number exceeds a user-defined threshold then the genes are switched between the parents. The amount of crossover is then dependent upon the threshold as well as the random numbers used.[49]

### 2.5.3 Blend Crossover

Blend crossover, like uniform crossover, is done gene by gene, but does not use the value of one gene or the other. Blend crossover is used for value-based genetic algorithms and cannot be used for binary genetic algorithms. In this technique, the two genes from each parent chromosome are blended to make two new children genes. A random number, $r$, is chosen between 0 and 1 for each gene. If $r \leq .5$ then the blend factor, $a$, is

$$a = \frac{(2r)^{\frac{1}{\eta}}}{2} \tag{2.15}$$

where $\eta$ is a user-defined parameter of blending. If $r > .5$ then

$$a = 1 - \frac{(2-2r)^{\frac{1}{\eta}}}{2}. \tag{2.16}$$

The blend factor is used to find the genes of the children, $y_1$ and $y_2$, from the parent genes, $x_1$ and $x_2$ by

$$y_1 = (a)x_1 + (1-a)x_2 \tag{2.17}$$

$$y_2 = (1-a)x_1 + (a)x_2. \tag{2.18}$$

As $\eta \to 0$ the blend crossover becomes uniform crossover. As $\eta \to \infty$ the blend factor $a \to .5$ and the blend crossover becomes an average crossover where the children genes are the average of the parent genes.[49]

### 2.5.4 Parthenogenesis

Depending on the system, the values may favor a value-based problem while the constraints of the system may not favor the blend crossover technique. For these cases we developed a single parent crossover technique which we called "parthenogenesis".[a] This type of crossover is used for value-based chromosomes where entire generations may become infeasible. This situation is illustrated in Figure 2.3. The red circle represents the area of the fan while the blue and green circles are the control sources. The genetic algorithm tries to get the control sources as close to the fan as possible without entering the area of the fan. To make the next generation the first control source of the first parent will blend with the first control source of the second parent. Almost all

[a] The term "parthenogenesis" is a common biology term used to describe a distinct type of asexual reproduction

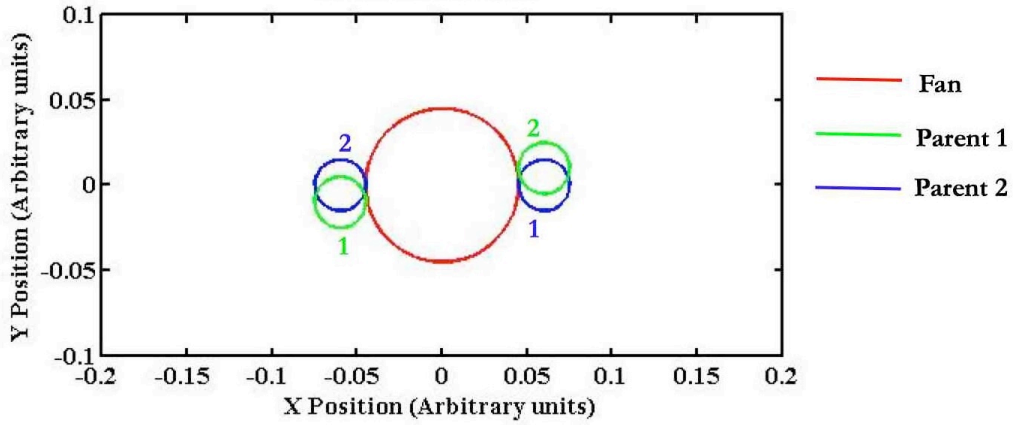


**Figure 2.3 Example of two configurations with mostly infeasible children**

of the blended children will be infeasible because of the nature of the constraints and the configuration of the control sources in each of the parents. This would not be the case in a binary representation due to the crossover techniques available.

Parthenogenesis uses a single parent to make a single child. This is done by taking a random number that is normally distributed around zero, $r_n$, with a user defined standard deviation. The larger the standard deviation of $r_n$, the more the child will be different relative to the parent. The random number is used to make a child by the equation

$$y = \alpha r_n + x, \tag{2.19}$$

where x is the parent gene, y is the child gene, and $\alpha$ is a dynamic factor which varies the amount of change of each generation. The dynamic factor is

$$\alpha = \left(1 - \frac{n-1}{N}\right)^{\beta} \tag{2.20}$$

with $n$ being the current generation, $N$ the total number of generations, and $\beta$ a user defined parameter which weights the dynamic nature of the function. If $\beta$ is set to zero then $\alpha = 1$ for every generation and the function becomes uniform over each generation.

If $\beta$ is greater than zero then the closer the current generation gets to the final generation, the smaller $\alpha$ gets and the less perturbation is allowed to the child chromosome.[49]

The parthenogenesis crossover allows the children to be mostly feasible while introducing diversity into the next generation. The dynamic nature of the crossover also allows the final generation to "settle" into the global minimum with precision. Since the parthenogenesis crossover only accepts traits from a single parent, a high mutation probability is needed to provide the needed diversity in the system.

## 2.6 Mutation

Similar to a natural selection environment, genetic algorithms also employ the process of mutation. Mutation is a random changing of genes to other chosen values. Mutation adds more diversity to the generation than is evident in the previous generation. This diversity is needed for global optimum convergence.

In a binary representation of values, mutation is the random changing of a single chromosome from a 0 to a 1 or vice versa (see Figure 2.4). In this case a change to a single gene in the chromosome can drastically change the representative value of the binary chromosome. Since a single gene mutation will introduce a large change in the gene, the probability of having a gene mutate can be much lower than a value-based genetic algorithm.

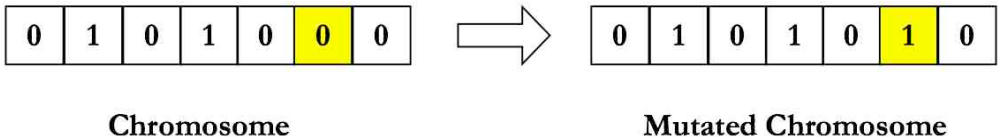


**Figure 2.4 Binary mutation**

In value-based genetic algorithms, the probability that a gene will mutate needs to be much higher to introduce a comparable amount of diversity into the generation as a

binary representation. If a gene is selected to be mutated through a random process, a random number, $r_{mut}$, is chosen, that is within the bounds of the variable space. If the random number is less than the gene, $r_{mut} \leq x$, the gene is mutated using the equation

$$x_{new} = x_{min} + (r_{mut} - x_{min})^{\alpha}(x - x_{min})^{1-\alpha}. \quad (2.21)$$

The mutation can also be dynamic using the same dynamic factor, $\alpha$, used in the parthenogenesis. The $x_{\min}$ variable is the minimum value that can be assigned to the specific gene. If $r_{mut} > x$ then the equation for the mutation is

$$x_{new} = x_{max} - (x_{max} - r_{mut})^{\alpha}(x_{max} - x)^{1-\alpha}. \quad (2.22)$$

The dynamic nature forces the mutation to favor the current value of the gene as the current generation reaches the final generation.[49]

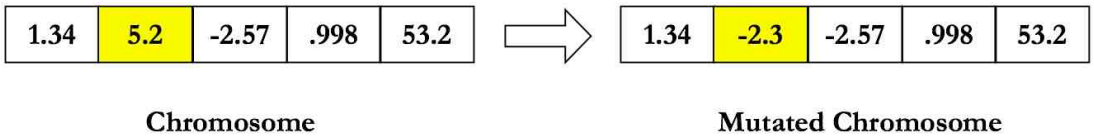


**Figure 2.5 Value-based mutation**

## 2.7 Elitism

Elitism allows competition between the children and the parent generations. When a new generation is made, the parent generation can be combined with the child generation to make a pool of chromosomes that are twice as large as a normal generation. The pool can then be sorted by fitness and the best half of the pool used for the next generation. Using elitism keeps fit designs in the gene pool that will be used to create new designs. Elitism can quickly diminish the amount of diversity in a generation if selection and mutation parameters are not used correctly.[49]

## 2.8 Constraints of the System

In this application, there are constraints to the system that need to be met by the global minimum. The constraints include having a limited space to place the primary and secondary sources. This constraint is due to the system having a limited space for speakers around a fan. If this application was made to a computer fan the control sources need to be placed within the area of the computer face. Another constraint of the system is that multiple sources cannot occupy the same space. A configuration that violates constraints is illustrated in Figure 2.6.

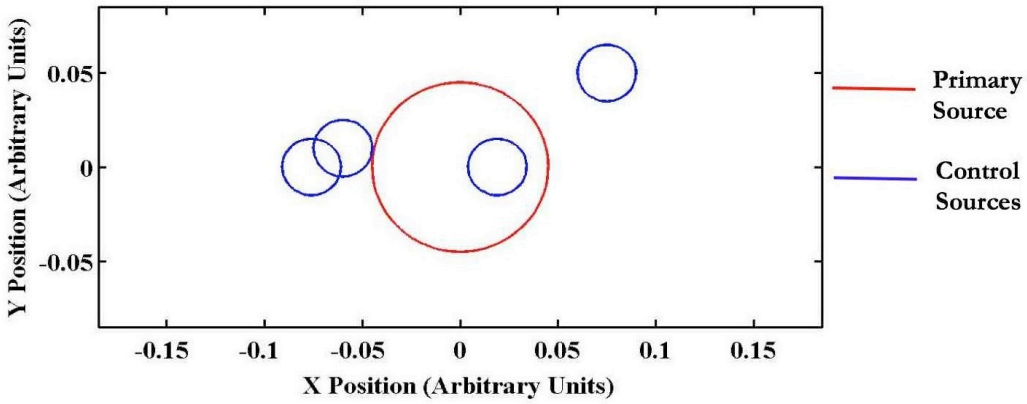


**Figure 2.6 Configuration with violated constraints**

The first of these constraints can be met in the two-dimensional algorithm by defining the variable space: $x_{\min}, x_{\max}, y_{\min}$, and $y_{\max}$. In the genetic algorithm, values below or above these values will never be used. Since values that violate these constraints are never introduced into the system, the chromosomes will never violate these constraints. A similar technique is used in the three-dimensional algorithm.

The second constraint was not as easily addressed. There are two common ways of dealing with constraints in genetic algorithms: a penalty function or a sudden death routine. In the penalty function approach, the fitness of each design is modified by violation of any constraints.[49] For example, if two of the control sources were too close

together, the achievable attenuation would be penalized. By using a penalty function, the algorithm will naturally choose designs that do not violate any constraints. In contrast, the sudden death approach will eliminate any designs that violate constraints and a new design will be created which meets the constraints. The sudden death approach requires more time for the algorithm to run, but will provide more feasible designs. This in turn will increase the probability of convergence to the global optimum.

### 2.8.1 Implementation of Constraints

A sudden death approach was used when constraints were violated. The constraint of two sources occupying the same space was implemented by defining a diameter of each source, control and primary. When a chromosome is defined, by random selection, for the first generation or by crossover for proceeding generations, each source in the configuration is analyzed to see if it meets the constraints. The constraints are met when the diameter of each source does not lie within the diameter of another source. If the constraints are met, the chromosome is kept and used in the algorithm. If the constraint is not met, the chromosome is discarded and the steps used to make the eliminated chromosome are repeated until the constraints are finally met.

### 2.8.2 Limitations of Constraints

Some realistic constraints of the system were not included in the model. The two major constraints not included are the frequency dependence of the control sources and the radiation characteristics of the control sources. The first of these constraints, the frequency dependence of the control sources, is a result of using non-ideal sources. In this study, small loudspeakers were used in the interest of space and separation distance. These small speakers have a limited frequency range that must be considered in the

implementation of the system. The second realistic constraint is the modeling of the control sources as monopoles. Similar to the previous constraint, this constraint is due to the nature of the control actuator used. The monopole nature of the loudspeakers is a good approximation of the source at low frequencies but breaks down as the frequency is increased. Small actuators are desired to decrease the distance between sources and to maintain the monopole radiation of the actuator, but small actuators typically have limited source strength at low frequency.

## 2.9 Implementation of the Algorithm

Matlab was used for the coding and implementation of this algorithm. The algorithm is designed to allow the user to input the number of primary sources, the diameter of each primary source, the complex source strength of each primary source, the number of control sources, the diameter of each control source, the frequency of the tone to be controlled, the feasible space where sources can be placed, and the genetic algorithm parameters.

### 2.9.1 Primary and Control Sources

A good representation of the primary sources is critical for the genetic algorithm to yield useable results. In this algorithm, the primary source can be modeled through a set of monopoles with complex source strengths, but for this study a single monopole will be studied. The complex source strengths give the flexibility to add multiple monopoles to the system to create multi-pole systems. The diameters of the primary sources are only used as a constraint on how close the control sources can be placed to the primary sources. This constraint is not used in the separation of the primary sources. Primary

sources can be placed as close together as needed. In contrast, the control sources can only be modeled as monopoles. The diameter of the control sources only effects the placement of the control sources and not the radiation characteristics. If higher order sources must be used for control sources, these can be modeled, but the algorithm must be modified. The source strength of the control sources is calculated by minimizing the radiated sound power from the system.

### 2.9.2 Frequency Dependence

The algorithm only optimizes the system for a single frequency. However, in many applications of ANC, the control system must control multiple frequencies. In the case where multiple frequencies must be controlled, only a single frequency can be run in the algorithm at a time. Additional code will give a plot of the frequency-dependent sound power reduction for a specific configuration. Referring to the *kd* plot (Figure 1.3), if the characteristic distance, *d*, were defined, then the reduction becomes only frequency dependent.

### 2.9.3 Algorithm Parameters

These parameters are used to specify the type of genetic algorithm that is used. In the selection process, the user must specify whether to use the tournament selection or the roulette wheel selection. If tournament selection is used, the size of the tournament must be specified. If the roulette wheel selection is used, the roulette exponent must be specified. Each of these parameters will determine the diversity that will exist in later generations. The crossover technique must also be specified. In most cases, the parthenogenesis crossover should be used. The standard deviation of the random numbers used for the process must also be defined. This value should not exceed 50% of

any dimension of the system to allow the crossover technique to pass on characteristics of previous generations. The mutation parameters will include the dynamic factor used in the parthenogenesis as well as in the mutation. The mutation probability is also set by the user and must be higher than would normally be the case in a binary genetic algorithm. Elitism can be used but is not required. Finally, the size and number of generations that will be used is specified. Using a larger generation size and/or more generations will lead to better convergence but will require more computation time.

### 2.9.4 Reflective Surfaces

The addition of reflective surfaces was included to account for near field reflections when a system is placed near walls or other barriers. To include the effects of the reflective surfaces, image sources were included into the analysis. Image sources were introduced into the analysis depending upon the system's position relative to the reflective surfaces. The sound power of the system was calculated based upon the output of the original system and the introduced image sources. Image sources are placed as though the sound rays that reflect off of surfaces originated behind the surface.

# Chapter 3

# Flow Field Investigation Methods

## 3.1 Introduction

Qualitative flow visualization techniques were used to investigate the characteristics of the flow field before quantitative particle image velocimetry techniques were used to investigate the flow field.

## 3.2 Flow Visualization

To obtain a qualitative understanding of the airflow, a flow visualization technique was used. In our case, the flow field from two different fans were compared and the experimental method for a quantitative technique determined. Flow visualization is performed by seeding the flow with small particles, illuminating the particles, and acquiring images of the illuminated particles. For the technique to be useful, the camera must be able to distinguish the illuminated particle flow from the background.

### 3.2.1 Flow Visualization Setup

To achieve a dark background and to allow for simultaneous acquisition of acoustical data, the flow visualization experiments were performed inside of an anechoic chamber with the lights off. In one set of tests, a glycerin-based fog machine was used to seed the flow inside of a mock computer enclosure. The test fan was mounted on the outside of the enclosure and moved the air from inside to the surrounding anechoic chamber. In a second set of tests, the flow was seeded outside of the enclosure. To accomplish this, the fog machine was placed next to the enclosure.

A strobe light was used instead of a continuous light. This gave a light burst for each frame of the video camera that was shorter in time than the shutter speed. The shutter on the camera could stay open for a longer period of time but received the most light from the strobe flash. This was necessary to prevent flow seed particles from moving a significant distance in a single frame, yielding "blurry" images.

**Figure 3.1 Photograph of flow visualization experimental setup**

A Panasonic 3CCD 4ECM video camera was used for the flow visualization image acquisition. This camera does not have a variable frame rate so the use of the strobe light at a different frequency than the set frame rate could lead to aliasing and blank frames. The camera does not have the resolution to resolve each particle of the flow field but does give good visualization of the flow field as a whole.

### 3.2.2 Forward Scattering

Flow visualization can only be accomplished if enough light is allowed to enter the camera for each frame. The contrast of the illuminated particles to the background light must also be high. To achieve sufficient contrast, the principle of forward scattering was used.[51] Forward scattering gives a better contrast of the particles to the background

light than would result from the use of either side or back scattering. Three different configurations were used, each of which took advantage of forward scattering, as shown in Figure 3.2.

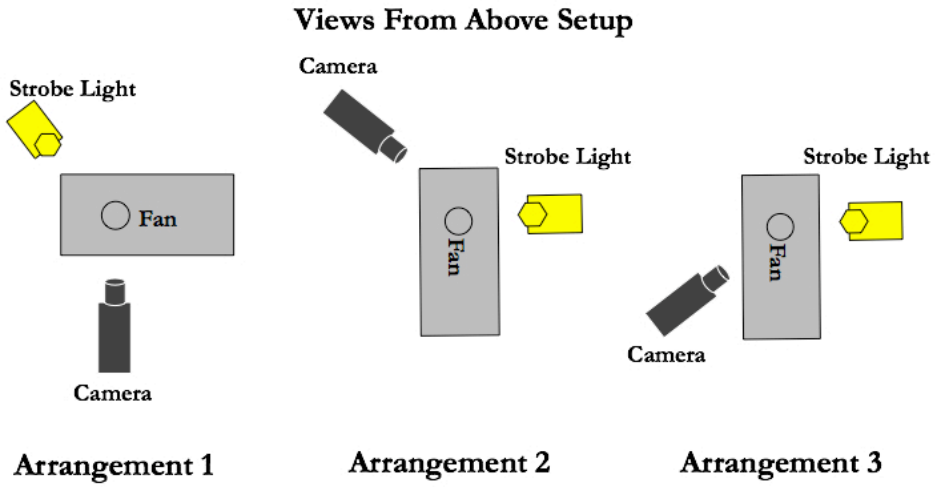


**Figure 3.2 Flow visualization arrangements**

### 3.3 Particle Image Velocimetry

Particle image velocimetry (PIV) was used to obtain quantitative measurements of the flow downstream of the fan. This data was desired to determine not only if the airspeed near the error sensors is turbulent but also if the speed is fast enough to generate a significant Doppler shift, thus introducing non-linearities into the ANC system. If a significant Doppler shift is introduced, the signal at the error sensor may no longer correlate with the reference signal

#### 3.3.1 Particle Image Velocimetry Theory

The theory behind PIV is to acquire two high-resolution images of particle-laden flow with a known time separation and perform correlation analysis with the images to determine a probable movement of the particles in the flow. Dividing the motion of the particles by the time difference will yield velocity. Correlation analysis in this manner over the entire image will yield a calibrated velocity vector field.[52] Typically, pulsed

laser sheets are used to obtain high-intensity particle illumination in a short period of time.

### 3.3.2 Particle Image Velocimetry Setup

PIV measurements were acquired using a commercial system (LaVision), including a laser, specialized digital CCD camera and data acquisition computer. The double-pulsed Nd:YAG laser produced a sheet of green light (532 nm wavelength); a lens system produced a two-dimensional sheet. The camera used was a double-shuttered charged coupled device (CCD). The double-pulsed laser and the double-shuttered camera were synchronized. This allowed for image pairs to be taken with a short time interval. The shutter time for the second exposure on the camera was longer to allow the timing of the second laser pulse to dictate the time difference between the two images. The camera and laser introduce limitations on the frequency resolution that will be present in the system. The highest frequency that the image pairs could be acquired was 5 Hz. This limited the frequency range that could be investigated, but was adequate to show changes in flow speed and direction.

Olive oil particles were used to seed the flow field. A LaVision seed generator was used to create aerosol particles with a size on the order of 1μm. This size of particle yielded low errors due to sedimentation and inertial effects. The terminal velocity from the sedimentation effects was only 27 $\mu m/\text{sec}$ while velocities of over 2 $m/\text{sec}$ were common, resulting in an error of less than 0.01%. Inertial effects resulted in the particles reaching 98% of the fluid speed in about 0.1 msec (see Appendix 1).

The results of the flow visualization indicated that seeding from the inside of the mock computer enclosure alone would not produce sufficient seed particles for PIV

analysis. This is because unseeded air originating from outside of the enclosure became entrained with the main column of air originating from within the enclosure. To overcome this challenge, the air around the mock enclosure was seeded as well as the inside of the enclosure. A large plenum was constructed with a medium density fiberboard frame covered with a green plastic film as seen in Figure 3.4. The dimensions of the plenum were 1.22 m x 1.22 m and 1.52 m tall. A .91 m x 1 m opening in the front of the plenum was made to allow the main flow from the fan to proceed unimpeded. A .3 m x .3 m hole was cut in the plenum, allowing the camera or laser to be used inside of the plenum. The use of the plenum allowed the entrained air to be investigated without seeding the entire lab.

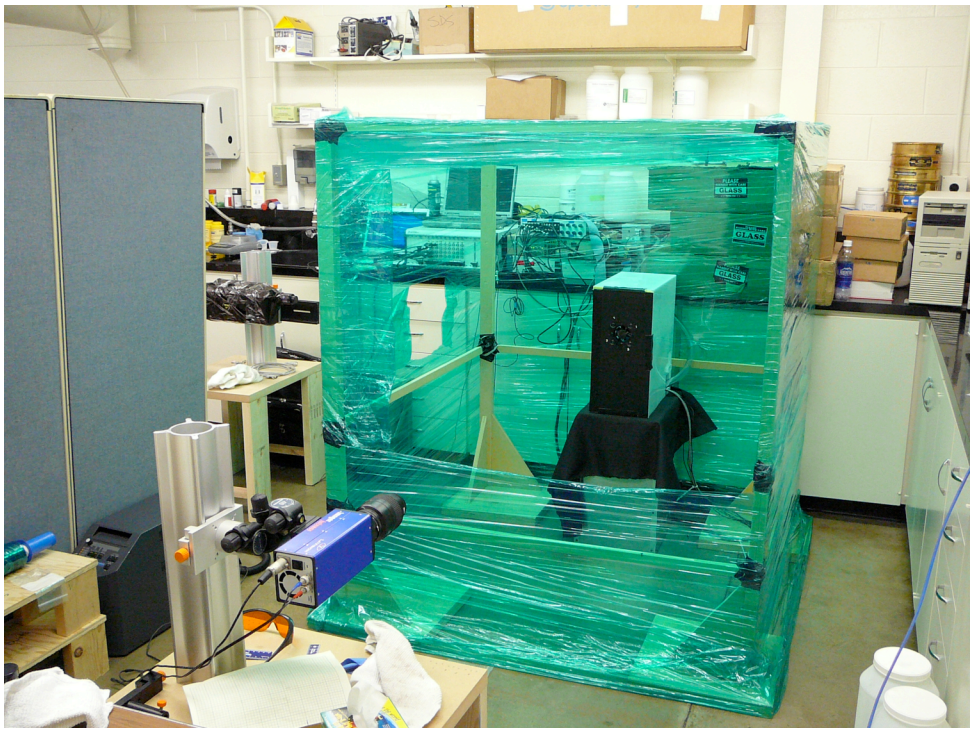

**Figure 3.3 Photograph of seeding plenum**

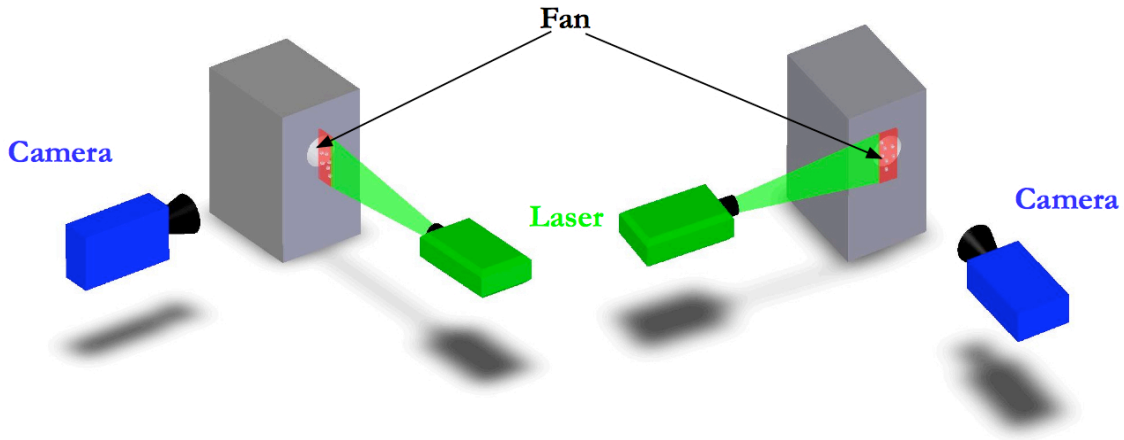


**Figure 3.4 PIV equipment orientations, orientation 1 (left) and orientation 2 (right)**

The PIV camera and laser were oriented to allow for vector fields to be made from two different orientations as shown in Figure 3.4. The two different orientations gave the vertical (orientation 1) as well as horizontal (orientation 2) flow relative to the fan. This is important because the turbulent air could be manifest in either direction. If only one orientation was used, the turbulent nature of a jet stream would be inadequately characterized. Since orientation 1 exhibits only a cross section of the overall flow column, two different planes using orientation 1 were used, with each containing a near field microphone. The location of the two planes normal to the fan are indicated in Figure 3.5 by white lines. The planes extend from the face of the fan out of the page. The orientation 2 plane lies parallel to the fan, 6 mm away from the plate.

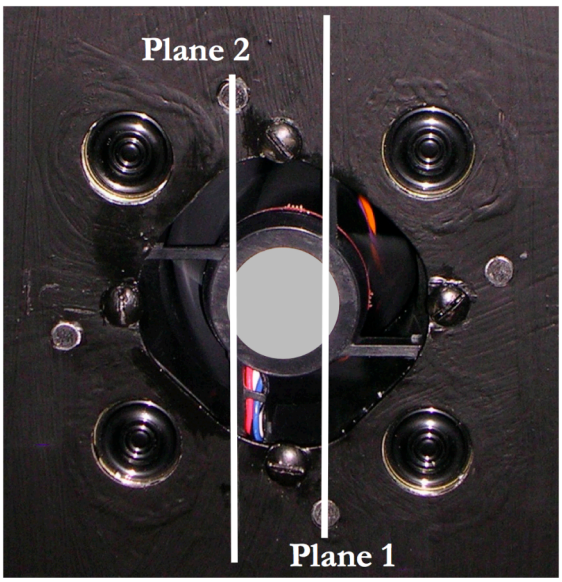


**Figure 3.5 Location of measurement planes**

### 3.3.3 Triggering System

Two different fans were investigated in these experiments. The main difference between the two fans was the driving signal of the fan. One fan used a constant DC signal. The DC signal was pulsed using the circuit internal to the fan. The second fan was a pulse width modulated (PWM) fan driven with an Agilent 33220A function generator. The PWM fan used pulses of constant voltage that change in duty cycle. That is, the longer the duty cycle, the higher the apparent voltage to the fan. The driving signals are illustrated in Figure 3.6.

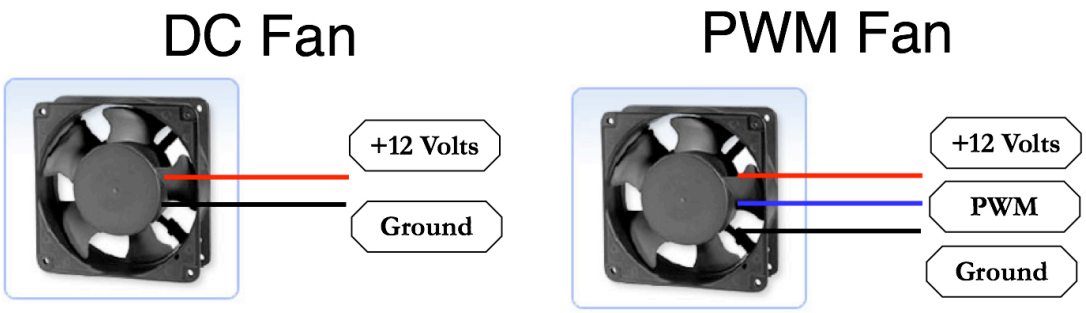


**Figure 3.6 Driving signal wiring diagram for DC and PWM-powered fans**

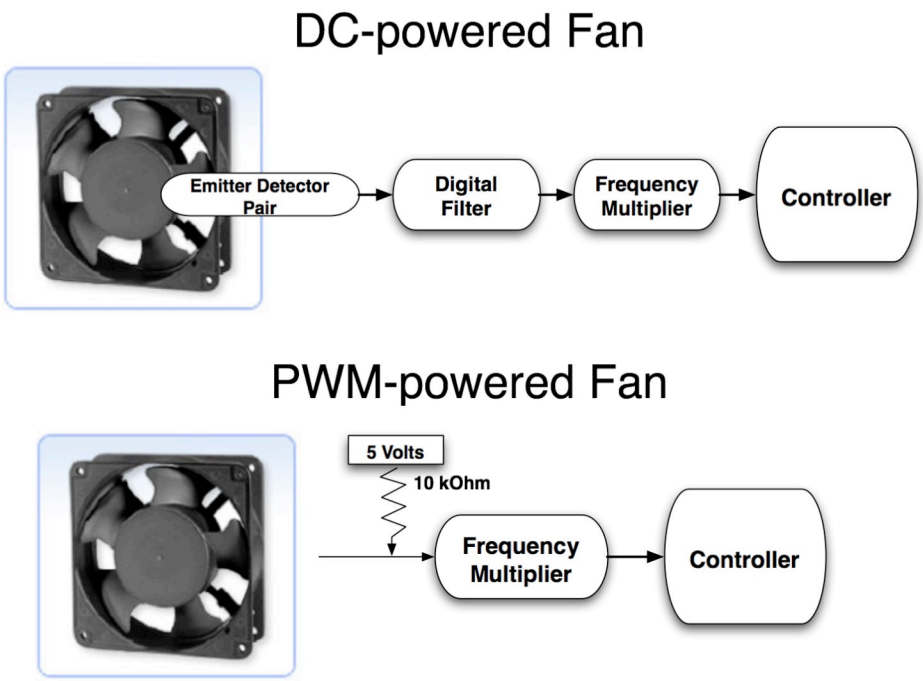


**Figure 3.7 Circuitry for trigger signals of DC (above) and PWM-powered (below) fans**

The trigger for the PIV system was different for each of the two fans. Each fan used the reference signal of the ANC system, but the ANC reference was obtained differently for the two fans. The DC fan used an emitter detector pair mounted on both sides of the blades that produced a pulse each time a fan blade passed. The PWM fan used an internal tach made up of a Hall's effect sensor that pulsed each time a pole from the internal magnet of the fan passed the sensor. The number of poles for the PWM fan was not equal to the number of blades. This necessitated the use of a frequency multiplier to obtain a signal correlated to the blade passage frequency. A circuit diagram for the trigger used for each fan is shown in Figure 3.7. The DC-powered fan used a Krohn-hite 8 pole model 3384 digital filter to remove any uncorrelated low frequency fluctuations. A pull-up resistor needed to be used on the tach signal of the PWM fan to supply the required current. The PWM did not require a digital filter. The five-volt supply and the 10 kOhm resistor pull up the voltage of the tach signal. A Trig-tek model 360C

frequency multiplier was used to convert the two pulses per rotation to five pulses per rotation to correlate with the five blades. The diagram for the trigger is shown in Figure 3.7.

The trigger signals can be seen in Figure 3.8. The rising edge of the PWM reference signal should coincide with every fifth rising edge of the trigger signal. This shows the relationship of the twice per rotation reference signal and the five times per rotation trigger signal.

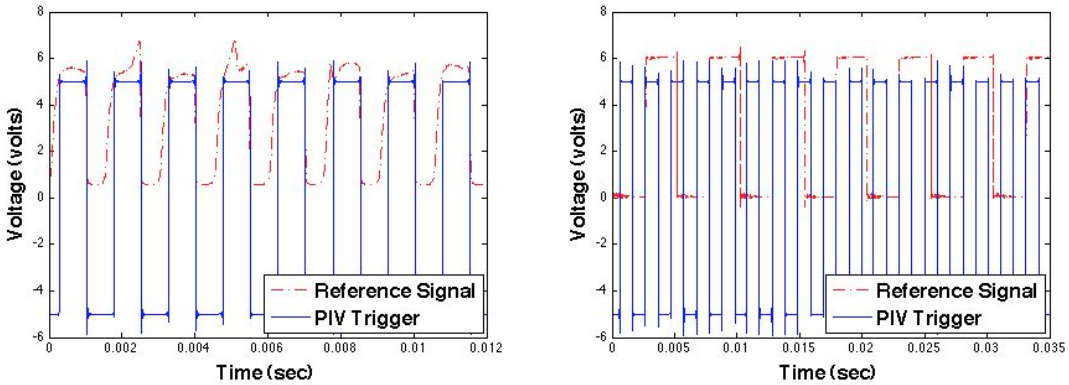


**Figure 3.8 Trigger and reference of the DC (left) and PWM-powered fans (right)**

The reference signal for the DC-powered fan should coincide with each pulse of the trigger signal. These trigger signals were verified by using synchronized PIV camera images. Both triggering techniques showed stationary blade position in the synchronized PIV images.

### 3.3.4 Vector Analysis

The images taken with the PIV system were used to obtain vector plots of the flow velocity. Vector plots of the flow field contain information such as the direction and magnitude of the air around the error sensors, the magnitude of the turbulence of the flow field, the differences and similarities between the flow fields of the two fans, and the changes in the flow field when using active noise control.

Vector plots were obtained by performing correlation analysis on the image pairs. Regions of the first image were spatially-correlated to the second image to obtain the average displacement of the particles in each region. The time increment between the two images yielded the needed information for the flow velocity of each region in the image.[51-53] Typical time intervals of 100 - 200 μsec were used for both fans. The LaVision software was used to obtain the vector plots for each image. The correlation analysis was performed using 32x32 pixel windows. A two-pass technique was utilized, first with a 32x32 window with a 25% overlap followed by a 32x32 window with a 25% overlap. For each measurement configuration approximately 400 image pairs were acquired to obtain an ensemble-averaged vector field (see Appendix 2).

Knowing the air velocity around the fan will determine whether the air flow is fast enough to cause an appreciable nonlinearity into the system by changing the frequency of the radiated sound relative to that at the error sensor. If the difference in frequency, $F_{error}$, is not negligible relative to the reference frequency radiated into the far field, $F_{ref}$, then the nonlinearities introduced could hinder the ANC system. The difference can be calculated by

$$F_{error} = F_{ref}\left(\frac{c \pm v_{turb}}{c}\right) \tag{3.1}$$

where $v_{turb}$ is the velocity of the flow field at the error sensor and $c$ is the speed of sound in air.

Knowing the turbulent nature of the flow field in the near field of the fan will also provide knowledge of areas with less turbulence for error sensor locations. The turbulence intensity of each measurement provides an estimate of the magnitude of flow velocity fluctuations. The turbulence intensity for a measurement is found by using $N$

image pairs. The ensemble average velocity, $\bar{u}$, for each vector at each position is found by averaging each vector at each position over each of the $N$ image pairs. The velocity of each image pair, $u_i$, is then used to find the turbulence intensity, $s_u$, through the equation

$$s_u = \frac{1}{u_{char}} \sqrt{\frac{1}{N-1}\left[\sum_{i=1}^{N}(u_i - \bar{u})^2\right]}, \tag{3.2}$$

where $u_{char}$ is the characteristic velocity.[54] Similar to the measurements performed by Lee *et. al*[53] in their analysis of an axial fan, the turbulence intensity of the axial component of the fan flow will be the focus of these results. The characteristic velocity used in these measurements was the manufacture-rated volumetric flow rate divided by the surface area of the orifice. The characteristic velocity used for the DC powered fan was .718 m/sec and 2.513 m/sec for the PWM powered fan.

### 3.4 Time Data Analysis

Time record data were taken of the error sensors as well as the reference signal during the PIV measurements. The time data were taken using a National Instruments system with a LabVIEW interface. Each channel was recorded for 30 seconds concurrently with the PIV measurements at a sampling frequency of 200 kHz. The frequency dependent coherence, $\gamma_{er}^2(\omega)$, of each of the error signals to the reference signal was calculated in Matlab using a Hanning window. The signal-to-noise ratio can then be calculated using the coherence function by the equation

$$SNR(\omega) = \frac{\gamma_{er}^2(\omega)}{1 - \gamma_{er}^2(\omega)}. \tag{3.3}$$

Maximizing the signal-to-noise ratio will maximize the achievable attenuation. The ratio of the power spectral density of the error signal with control $S_c(\omega)_{\min}$ (linear scale) and the power spectral density of the error signal with no control $S_n(\omega)$ (linear scale) is related to the coherence, $\gamma_{er}^2$, by

$$\frac{S_c(\omega)_{min}}{S_n(\omega)} = 1 - \gamma_{er}^2(\omega) \quad . \tag{3.4}$$

The signal to noise ratio can be compared to the turbulence intensity to see if there is a correlation between the two measurements.[15]

# Chapter 4

# Active Noise Control Methods

## 4.1 Introduction

The active noise control system that was used was developed by Brigham Young University and is a multi-channel, gradient descent-based, filtered-X algorithm control system.

## 4.2 Algorithm

The active noise control system used in this research was similar to that used in Gee and Sommerfeldt's[26-28] and Monson *et al.*'s[55] work. The algorithm used was based on a filtered-X LMS algorithm (see Figure 4.1). The system identification process was an offline procedure performed before the control algorithm was implemented. The system identification process was used to account for the transfer path of the control signal through the system. A gradient descent optimization method was used because the optimization space was quadratic in nature. The convergence of the system was dependent upon the convergence parameter, $\mu$. The magnitude of $\mu$ dictates the speed of the control convergence as well as the effectiveness of the controller in tracking a changing time reference.

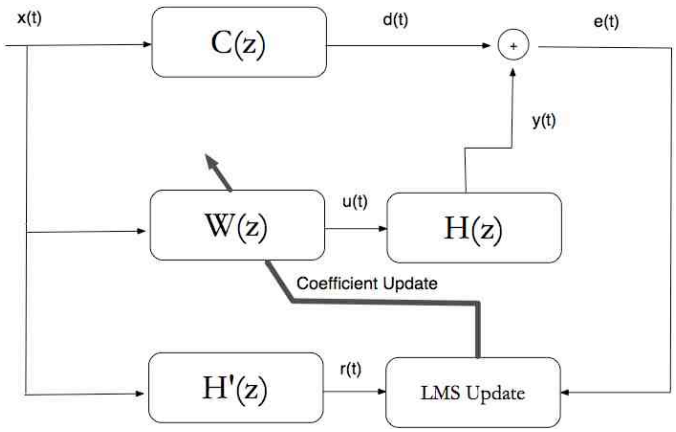


**Figure 4.1 Filtered-X algorithm block diagram**

## 4.3 Hardware

### 4.3.1 Fans

Two fans with distinct differences were used in this study. The first fan, a DC-powered, 60 mm, Mechatronics model F6025X12B was similar to that used by Monson.[29] This fan used a single DC power source, supplied to the internal circuitry of the fan. The DC-powered fan is meant to run with a 12-volt supply, but will run at slower speeds if a voltage less than 12 volts is supplied to the circuitry, as long as the circuitry has enough voltage to stay powered. DC-powered fans will typically not run with voltages lower than 5-8 volts. This fan required an emitter detector pair which was mounted on an obstruction on the inlet and outlet of the fan.

The second fan used was a pulse width modulated (PWM) powered, 60 mm, model 2415KL04W NMB fan that has stark contrasts to the first fan. The PWM signal that was used to power the fan was a high-frequency (25 kHz) signal that oscillates between 0 and 12 volts. A separate constant DC voltage was used to power the internal electronics on the fan (see Figure 4.2). The PWM fan was developed to be used more conveniently in a computer cooling system where constant voltage rails are commonly the only efficient power sources. The duty cycle of the pulse widths were modified to

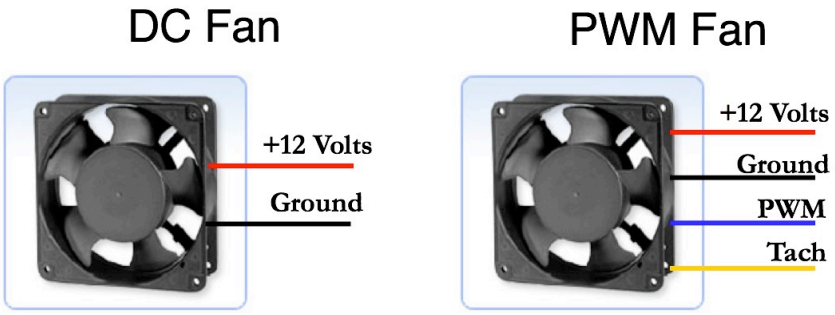


**Figure 4.2 Wiring diagrams for the DC and PWM-powered fans**

change the effective voltage that was supplied to the fan. The longer the pulses, the more equivalent voltage was "seen" by the fan. The frequency of the pulses used in the PWM signal is typically out of audible range to avoid hearing any effects from the pulses.

Another noticeable difference between the two fans was the number of fan blades used by each fan. The DC-powered fan used seven fan blades while the PWM-powered fan had only five. This resulted in different blade passage frequencies from the same rotational frequency for each fan. Another notable difference was the tachometer available on the PWM-powered fan that was not available for the DC-powered fan. This difference will be discussed more in the reference signal section. Other differences, including the blade shape, hub diameter, and the angle of attack will not be considered, even though they influenced the volumetric flow rate and radiated sound.

### 4.3.2 Reference Signal

To run active control on either fan, a reference signal was required. The reference signal for each of the two fans was obtained quite differently. The DC-powered fan had an emitter-detector mounted onto the fan that sensed when a blade passed the emitter-detector assembly. This setup was similar to that used by Gee and Sommerfeldt[26-28] and Monson.[29] To keep the emitter and detector stationary, mounting brackets were used on the inlet and outlet of the fan. The mounting brackets acted as obstructions to the fan

flow that hindered the movement of air through the fan and effectively boosted the levels of the BPF and its harmonics. The signal obtained through the emitter detector pair was not sinusoidal or a perfect square wave. The waveform had the BPF and many of its harmonics present. This allowed the active control system to use the same reference for the BPF and its harmonics. External signal conditioning equipment, including a Krohn-hite 8 pole 3384 digital filter and homemade gain stage, were used on the reference signal to avoid a DC offset, attenuate unwanted higher harmonics, and to implement any needed gain in the signal. The reference signal path is shown in Figure 4.3.

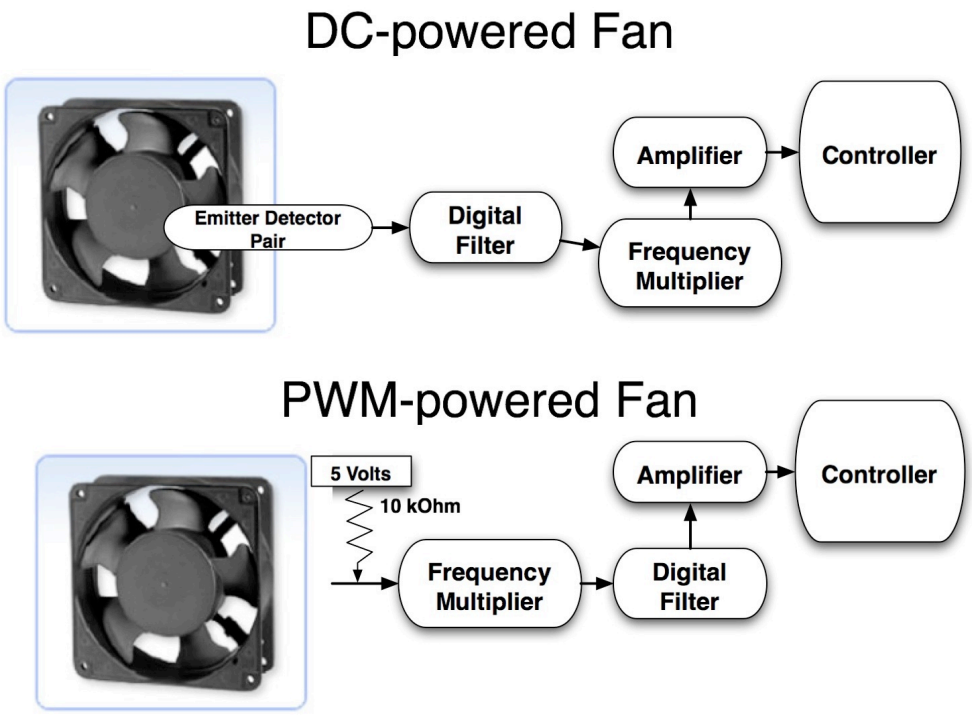


**Figure 4.3 Reference signal diagrams for DC and PWM-powered fans**

As compared to the DC-powered fan, the PWM-powered fan used a much different mechanism for the reference signal. As mentioned above, the tachometer available in the internal electronics of the fan was used. The tachometer used Hall effect sensors to track the speed of the fan. The four poles of the fan magnet caused the Hall effect sensor to give two pulses for every rotation. Since the PWM-powered fan is a five-

bladed fan, the BPF was related to the tachometer signal by a 5/2 factor. A Trig-tek model 360C frequency multiplier was used to multiply the tachometer signal to be used as a reference to the BPF. The tachometer signal also required a pull-up resistor to boost the current of the signal. The pull-up resistor gave the tachometer signal the current and the voltage that was needed for the reference. External signal conditioning equipment, including a Krohn-hite 8 pole 3384 digital filter and an in-house made gain stage, were also used to avoid a DC offset, to attenuate unwanted higher harmonics, and to implement any needed gain in the signal in the PWM-powered fan as well. An Agilent 33220A function generator was used to provide the 25 kHz PWM signal.

**Figure 4.4 Photographs of loudspeaker (left) and PVC enclosure (right)**

### 4.3.3 Control Sources

Small loudspeakers were used as control sources. The control sources used in this research were not the smallest available loudspeakers, which would reduce the distance between the control source and primary source. Instead, these 25.4 mm, high excursion drivers were chosen because of their good response and high output level at the frequencies of interest.

Small enclosures were made out of PVC caps, normally used in plumbing systems. The smallest PVC caps that could house the magnet and loudspeaker assembly

were used. The enclosures were not optimized for frequency response, but instead were optimized to fit into the required area. PVC caps were chosen to keep the radiation of the drivers as close to monopoles as possible. The inclusion of the PVC caps reduced the interaction between the rear sides of the sources inside of the enclosure.

### 4.3.4 Error Sensors

The electret microphones used in this set up were chosen for their small size, high flexibility, and low cost. Since the microphones were being used to create theoretical nulls, which are small in size, small microphones were desirable. Also small microphones also allowed the entire system to be compact. Finally, the flexibility of the microphone mounting allowed the user to easily change error sensor placement. Since the amount of control that can be achieved is strongly affected by the error sensor placement, the flexibility of the microphone placement was crucial. Small amplifier circuits were built to give the error signals the needed gain. The first gain stage implemented was a constant gain stage that was in close proximity to the microphones. After the initial gain stage, an additional variable gain stage was used further down the signal path, closer to the controller.

### 4.3.5 Filters and Gain Stages

Filtering and gain stages were used to eliminate aliasing effects, reduce noise, and to take advantage of the full dynamic range of the analog-to-digital converters. The sample rate of the DSP controller was normally set in a range that could introduce audible aliased tones if not filtered. Digital filters were also used to reduce low-frequency noise below the tonal components targeted by the active control system to keep the signals from clipping and allow the signal components of interest to dominate the

signal. Finally, variable gain stages were used on each of the input and output channels to take advantage of the 16-bit converters. The variable gain stages allowed the system to obtain better control by taking full advantage of the dynamic range of the converters.

### 4.3.6 Digital Signal Processing

A Texas Instruments TMS320C6713GDP was used for the digital signal processing. This particular board operates on a 225 MHz clock and has the capacity for 1800 million instructions per second (MIPS) or 120 million floating-point operations per second (MFLOPS). The accompanying I/O board supplies 12 channels each with a 16-bit analog-to-digital converter (ADC) or digital-to-analog converter (DAC) depending on whether the channel is an input or output channel.

# Chapter 5

# Genetic Algorithm Results

## 5.1 Genetic Algorithm Results

To analyze the results of the genetic algorithm, various factors will be investigated. First, the final generation will be presented to show the best configuration for the given constraints. When using a dynamic genetic algorithm, all of the configurations in the final generation will be similar. The fitness history will illustrate how the algorithm converged to the final configuration by showing the attenuation at the chosen frequency for the best configuration in a given generation. This can be important to show how quickly the algorithm was able to converge. Another important graph will show how much attenuation is achieved by the final configuration over a frequency range of interest. Since the genetic algorithm only uses a single frequency of interest, oftentimes it is crucial to know if the final configuration is superior to other configurations over a given frequency range.

In each of these cases, a generation size of 1000 was used and the algorithm was run for 1000 generations unless otherwise specified. The constraint for the primary source was a diameter of 9 cm and 3 cm for each control source. The frequency of interest was 500 Hz, which is in the range of a typical BPF for fans running at high speeds. Each primary source was modeled as a monopole. Dynamic parthenogenesis crossover, dynamic mutation, and a tournament style of selection were used unless otherwise specified.

### 5.1.1 Single Control Source

When a single control is used in the algorithm, the control source gets as close to the primary source as possible. This is what should be expected for a single control source since the radiated power is a function of frequency and distance. Figure 5.1 shows the design space that the algorithm is allowed to explore and the final control source configuration. The space that the algorithm was allowed to search was based upon the realistic size of a computer enclosure. Locations of the sources are only important relative to each other and could be rotated without affecting the results. The fitness history shows that the optimized sound power of the entire system, $W_o$, relative to the sound power of the primary sources, $W_{pp}$, drops quite quickly then stays steady. This means that the optimal control source configuration was quickly found.

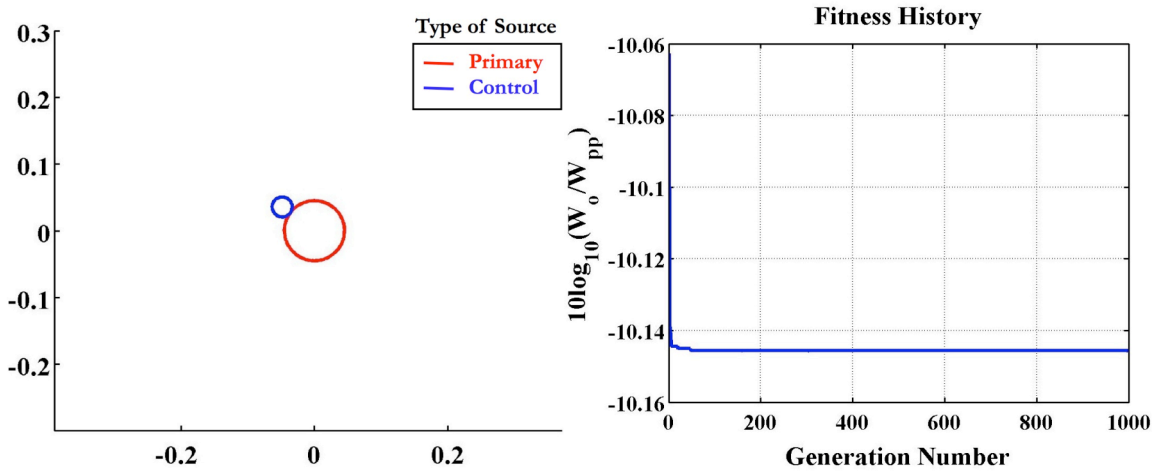


**Figure 5.1 Final generation (left) and fitness history (right) of a single control source and a single primary source**

### 5.1.2 Two Control Sources

When two control sources were used in the algorithm, the control sources formed a symmetric configuration. The two control sources get as close to the primary source as possible to maximize the source coupling between the sources, which is shown in

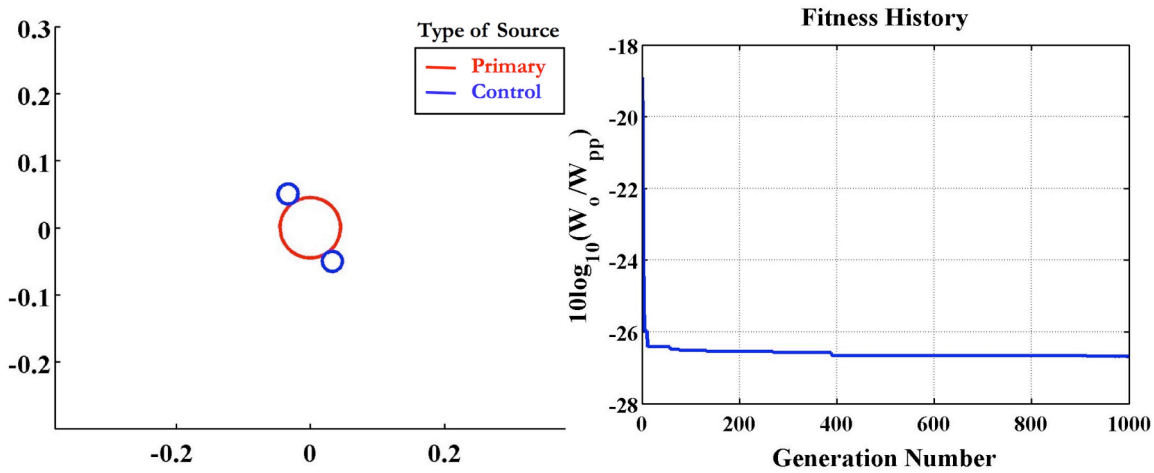


**Figure 5.2 Final generation (left) and fitness history (right) of two control sources and a single primary source**

Figure 5.2. The fitness history shows that a much better reduction is achieved when using two sources instead of one and the algorithm convergences quickly.

### 5.1.3 Three Control Sources

When using three control sources, a counter-intuitive arrangement is given as the optimal configuration. It is counter-intuitive because all of the control sources do not get as close to the primary source as possible. Looking at a specific test run done with the genetic algorithm, we can see how a mutation can help to find a global instead of a local optimum. In Figure 5.3 we see the best configuration of generation 42 and 43. A mutation in the algorithm changed the best configuration from one that was converging in a symmetric pattern to one that was linear. If we look at the fitness history in Figure 5.4, we see that the sound power output of the system from about generation 40 to generation 50 drops dramatically. This increase in attenuation shows that a linear control source configuration achieves more attenuation than a symmetric configuration at 500 Hz. The sound power continues to drop as the control sources get closer to the primary source while keeping this linear configuration.

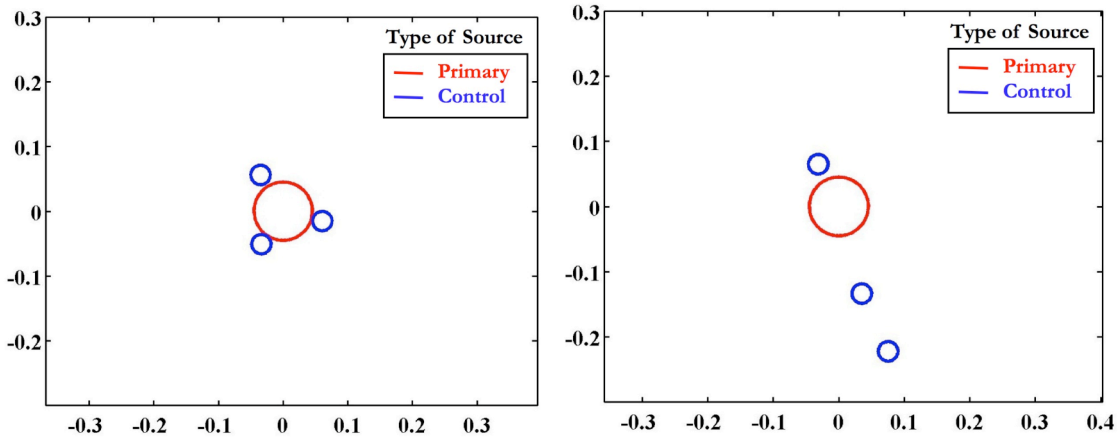


**Figure 5.3 Best configuration of generation 42 (left) and generation 43 (right)**

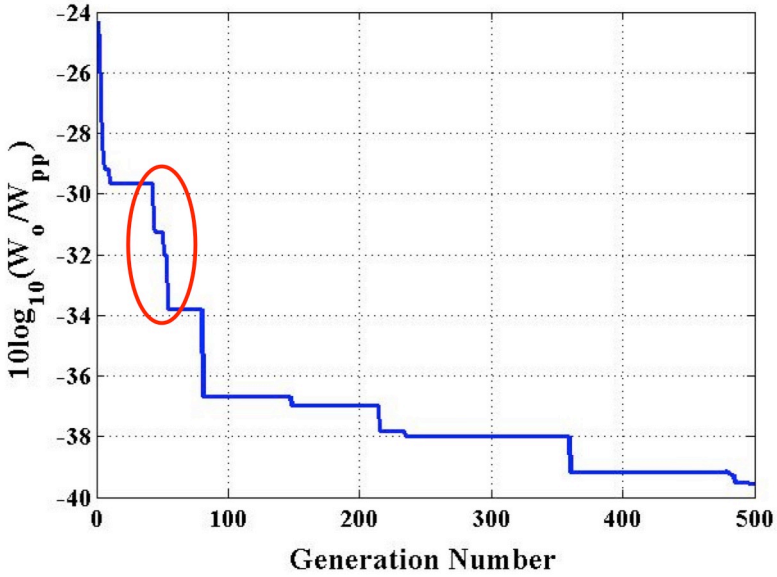


**Figure 5.4 Fitness history of three control sources changing from a symmetric to a linear configuration**

When we look at an optimization run with the default settings, we see that the three control sources converge to a linear configuration with the control sources as close to the primary source and adjacent control sources as possible (Figure 5.5). This case does not converge quite as fast as those with fewer control sources because of the much larger design space of possible configurations.

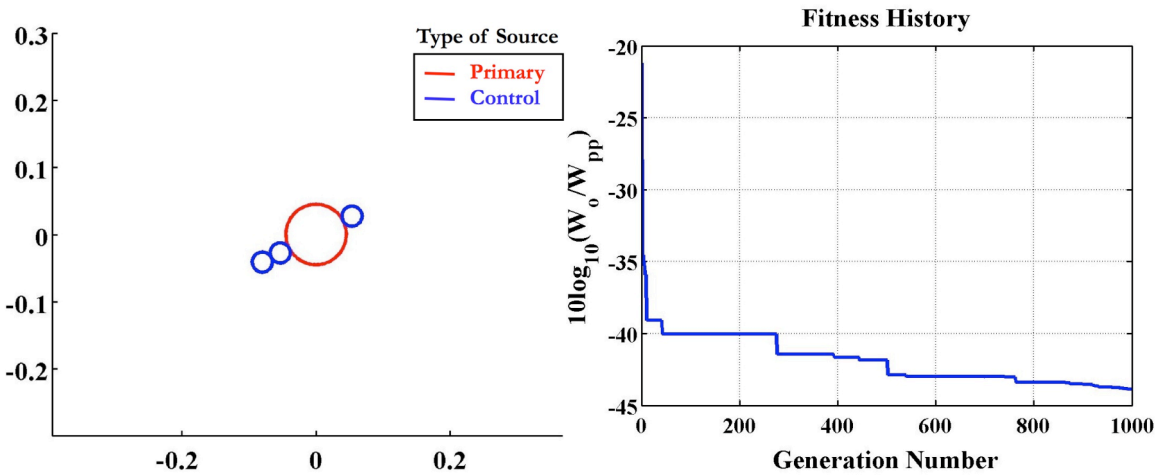


**Figure 5.5 Final generation (left) and fitness history (right) of three control sources and a single primary source**

### 5.1.4 Four Control Sources

Using four control sources with a single primary source continued to the trend of the sources forming a linear configuration rather than a symmetric pattern around the primary source. The final configuration can be seen in Figure 5.6. The fitness history shows that the convergence of these control sources did not converge as quickly as the cases with fewer control sources. Since the number of possible configurations has increased drastically, more generations were required for the algorithm to properly converge.

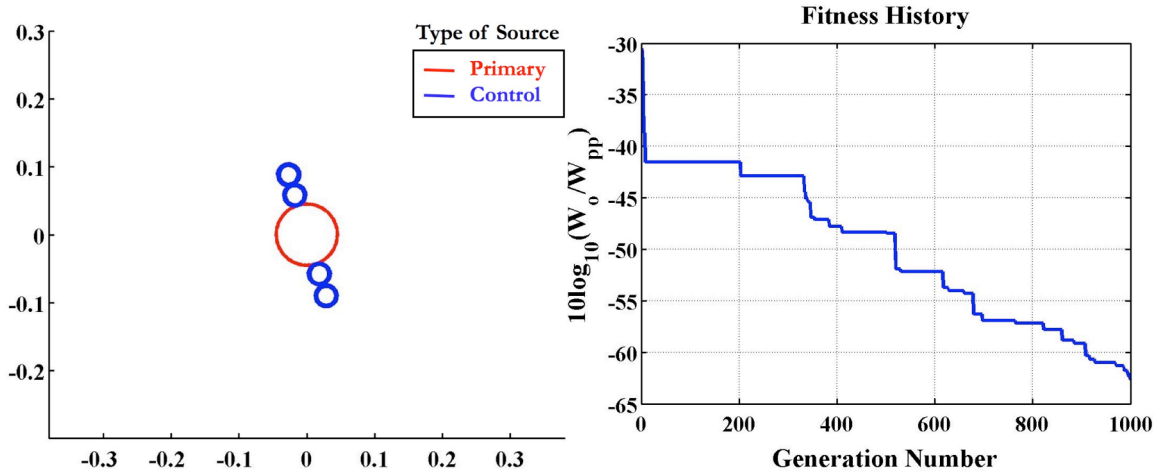


**Figure 5.6 Final generation (left) and fitness history (right) of four control sources and a single primary source**

One concern with using the genetic algorithm was that a single frequency was used to obtain a sound power output for the system. This is useful when there is a single tone or a narrow band of energy that needs to be controlled. The linear configuration showed above was optimized for 500 Hz. Figure 5.7 shows that even though the algorithm was optimizing the sound power attenuation for 500 Hz, the configuration attenuates over a broad range of frequencies and does not provide a "notch" at the frequency of interest. The strong frequency-independent nature is a desirable quality in the optimal configuration.

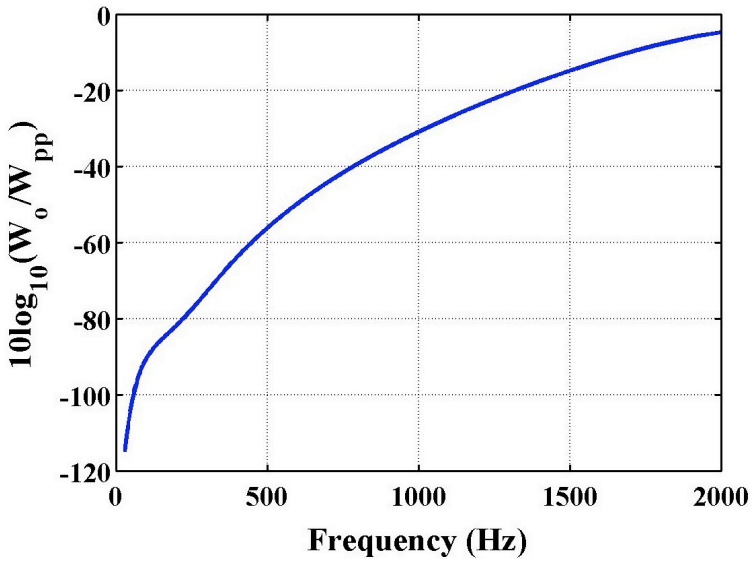


**Figure 5.7 Attenuation as a function of frequency for four control sources and a single primary source in a linear configuration**

To find the global optimum configuration, the parameters used in the genetic algorithm had to be optimized. Multiple techniques were used to find the best parameters in this algorithm. Normally, the type of crossover and selection can dramatically affect the algorithm. In all of these tests, the parthenogenesis crossover was used to allow for feasible generations. Multiple types of selection could be used. The default was a tournament selection with a tournament size of about 20, which allowed relatively less

diversity into the system. The roulette wheel selection technique allowed more diversity. The results of the roulette wheel selection can be seen in Figure 5.8. The algorithm was able to fully converge to the optimal solution, which is shown by the overlap of the configurations in the final generation. However, the computation time required was almost doubled as a result of using the roulette wheel selection rather than tournament selection.

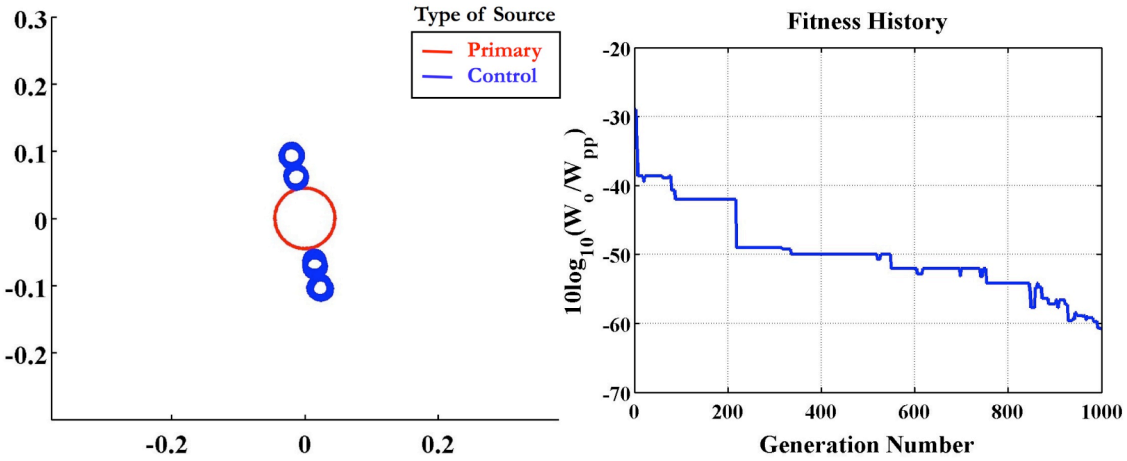


**Figure 5.8 Final generation (left) and fitness history (right) of four control sources and a single primary source with roulette wheel selection**

Since the algorithm was implemented with values over a continuous interval, a higher mutation parameter was required than would normally be used. In a binary representation, a single mutation can drastically change the chromosome. With real valued chromosomes, a single mutation will only mutate the chromosome to a certain degree. Therefore, a higher mutation probability is needed to provide the needed diversity into the system. When a low mutation was used, such as 0.05 instead of the default 0.25, the algorithm would converge to a local minimum more often. This can be seen in Figure 5.9 where the algorithm was not able to converge to the optimal configuration.

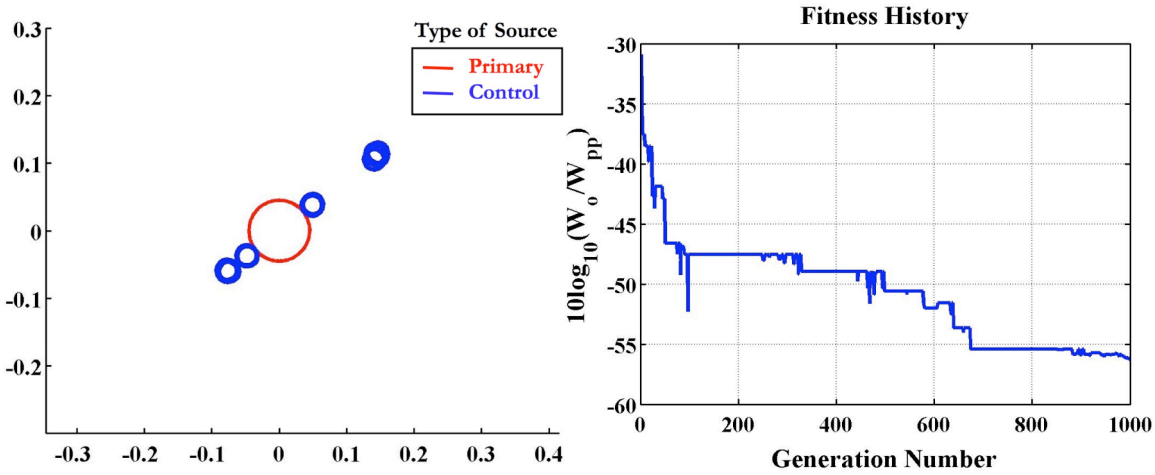


**Figure 5.9 Final generation (left) and fitness history (right) of four control sources and a single primary source with roulette wheel selection and low mutation**

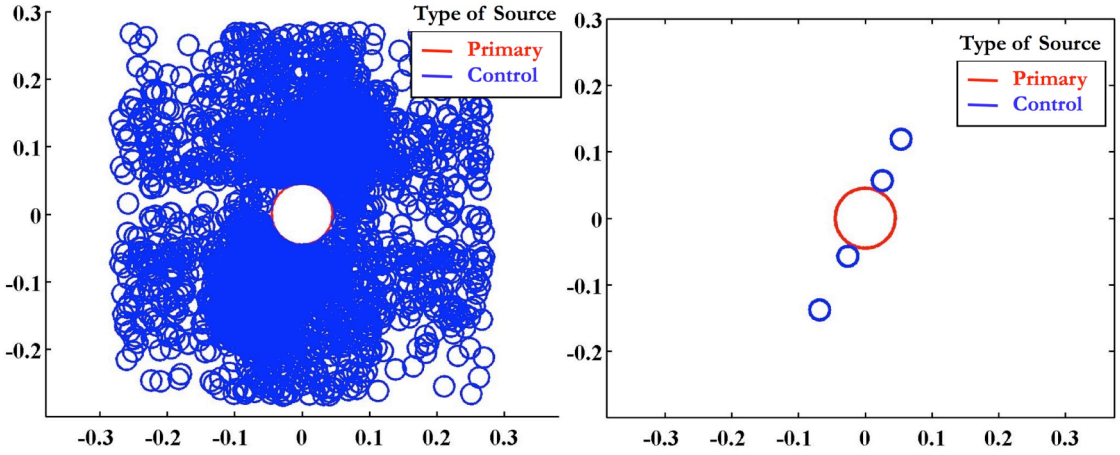


**Figure 5.10 Final generation (left) and best configuration of final generation (right) of four control sources and a single primary source with a static system**

One of the most important parameters investigated was the dynamic nature of the crossover and mutation. The default dynamic nature of the system was far superior to a static algorithm. The final generation of a static system, along with the best configuration of the final generation, are shown in Figure 5.10. Without the dynamic nature in the system, the search space of the algorithm stays too large and the probability of converging to the optimal solution is drastically reduced. Figure 5.11 shows that this type of algorithm does not converge with a quasi-slope, instead a few larger steps are

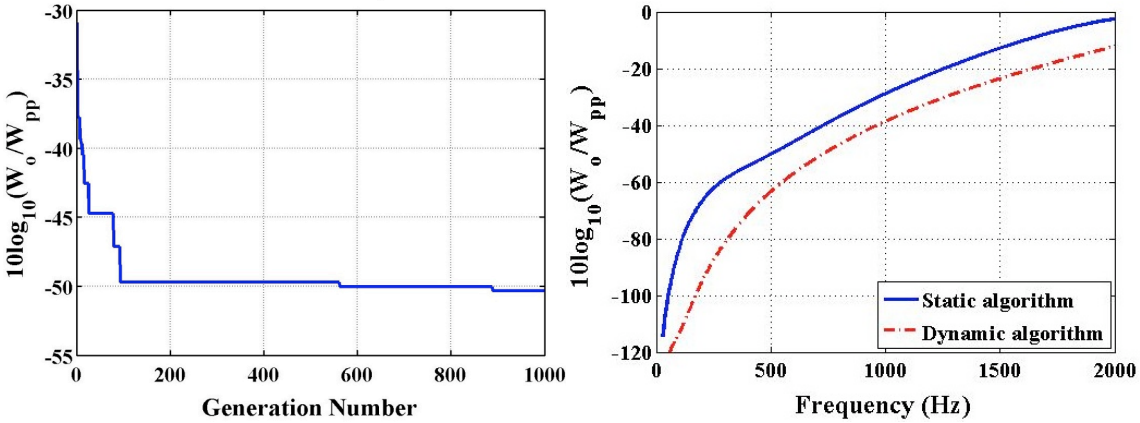


**Figure 5.11 Fitness history (left) and sound power reduction (right) of four control sources and a single primary source with a static and a dynamic system**

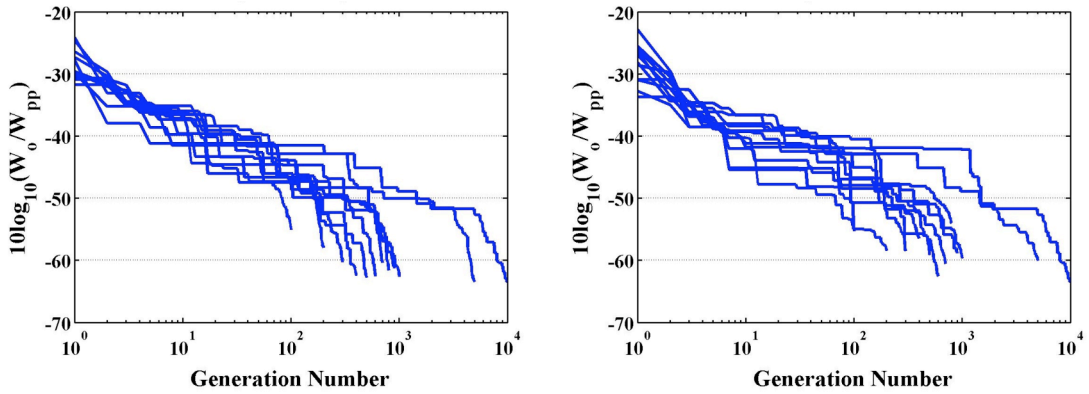


**Figure 5.12 Fitness history for multiple generation sizes with high mutation (left) and low mutation (right)**

taken. The attenuation over frequency can be seen to be less than that of the optimal solution at all frequencies.

The number of generations used was also a limiting factor in the search for the optimal configuration for a specific primary source configuration. Figure 5.12 shows the amount of attenuation achieved when using different generation sizes. These results are not comprehensive because the results depend upon a probability. However, they do show the general trend of the need for more generations and a higher mutation parameter. The final attenuation from the high mutation cases follows a general trend of better reduction with more generations. The final attenuation from the low mutation cases, on

the other hand, does not seem to follow this same trend; instead the attenuation is more monotonic in nature.

### 5.1.5 Four Control Source Configuration Comparison

Before a linear configuration of sources is finally determined to be better, further investigation of the two different configurations is warranted (Figure 5.13). Because sound power is a global flux measurement, the sound power calculations take areas of less control into account. Since the algorithm was optimized for a single frequency for given source dimensions, a comparison of attenuation over frequency is important. Figure 5.14 shows that the linear configuration achieves more attenuation at most frequencies of interest than the symmetric case. For these dimensions and at the frequency of interest, 500 Hz, the linear case will attain a maximum of 30 dB more sound power reduction as compared to the symmetric case. If we take a closer look at lower frequencies the difference is more pronounced (Figure 5.15). This does not hold true throughout the entire spectrum. In fact, the symmetric case is able to achieve more attenuation at high frequencies (Figure 5.15). The attenuation at this frequency range is already negligible and is more suited for passive control.

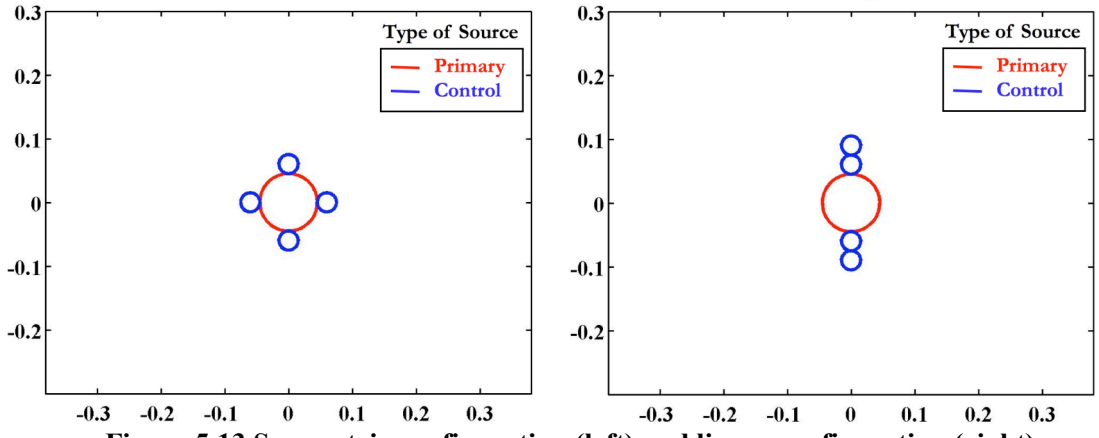


**Figure 5.13 Symmetric configuration (left) and linear configuration (right)**

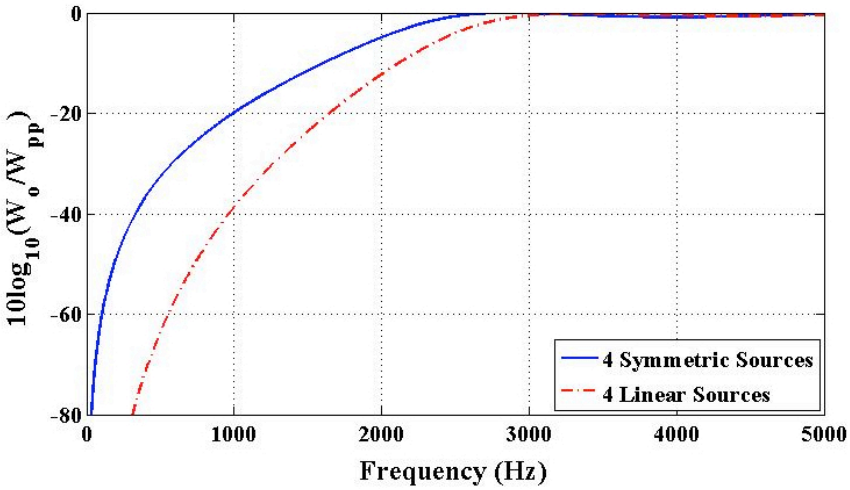


**Figure 5.14 Comparison of attenuation for the symmetric and linear configurations as a function of frequency**

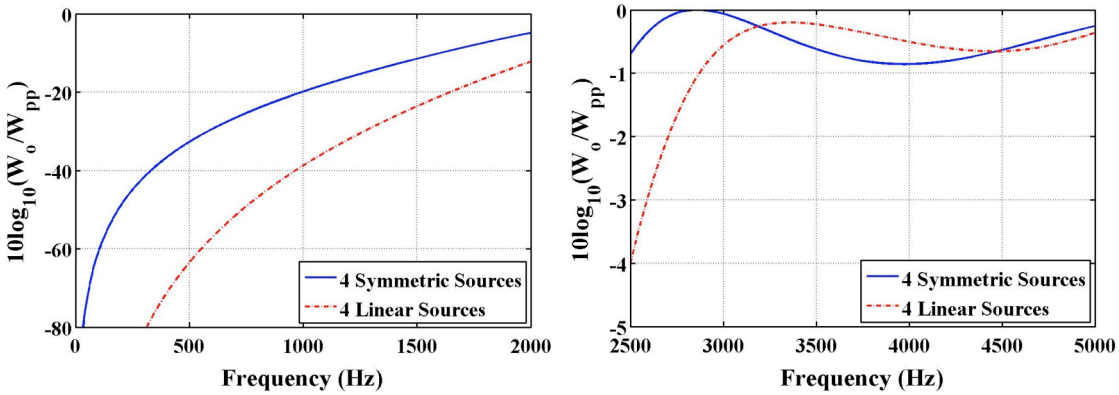


**Figure 5.15 Zoomed plots for the comparison of attenuation for the symmetric and linear configurations as a function of frequency**

To practically implement the linear design, the control sources need to be able to create the needed source strength without the introduction of distortion. When using the linear configuration, the source strength of the two control sources that are closest to the primary source is much greater than the source strength of the control sources in the symmetric configuration. A comparison of the source strength of each control source relative to the source strength of the primary source is shown in Figure 5.16. In the symmetric configuration, all of the control sources have the same source strength. In the linear case, the two closest sources have different source strengths as compared with the two sources that are farther from the primary source.

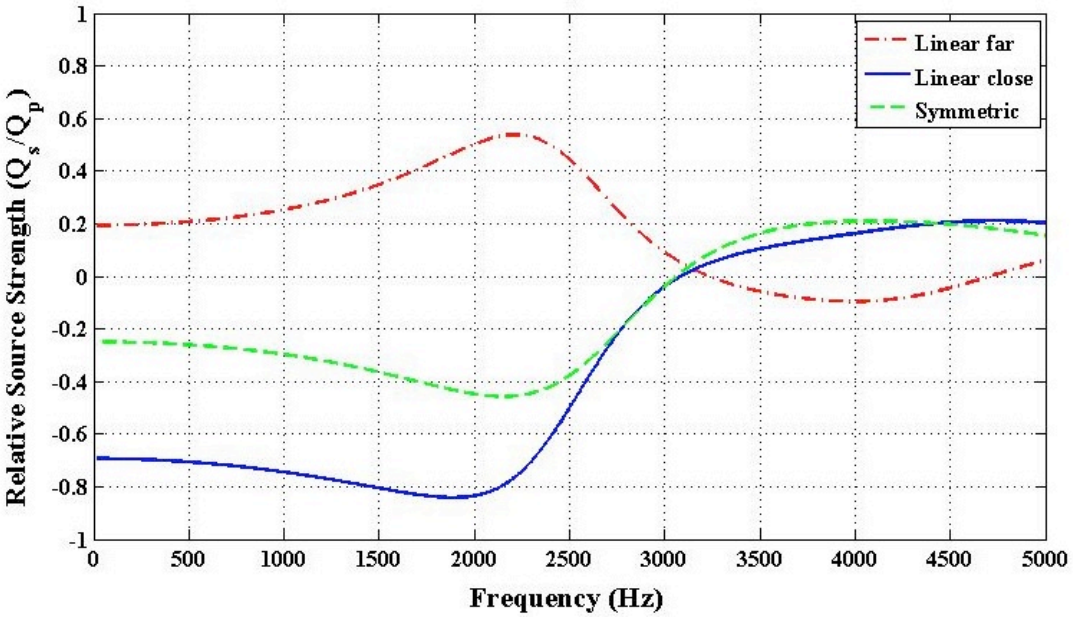


**Figure 5.16 Relative source strength of control sources for linear and symmetric configurations as a function of frequency**

## 5.2 Reflective Surfaces

The optimal configuration of control sources could be altered by the introduction of acoustically reflective surfaces near the sound sources. To find the optimal configuration for the case with primary sources near reflective surfaces, the genetic algorithm had to be adapted to include image sources. Similar results were found for a single primary source and four control sources near two perpendicular planes. In some cases, the genetic algorithm would converge to four control sources in a linear fashion parallel to one of the surfaces. In other cases, the sources would arrange in a linear fashion in a $45^\circ$ angle from both surfaces. The two configurations are illustrated in Figure 5.17. Since the results from the genetic algorithm are based upon probability, the genetic algorithm must be run multiple times to ensure that the results are in fact the global minimum, and not a similar local minimum. The comparison of the two configurations' attenuation over frequency can be seen in Figure 5.18. It must be noted that the sound power attenuation calculation is the sound power put out by the primary

source, the control sources, and all image sources. An implementation where the sources will be parallel to the reflective surfaces is superior.

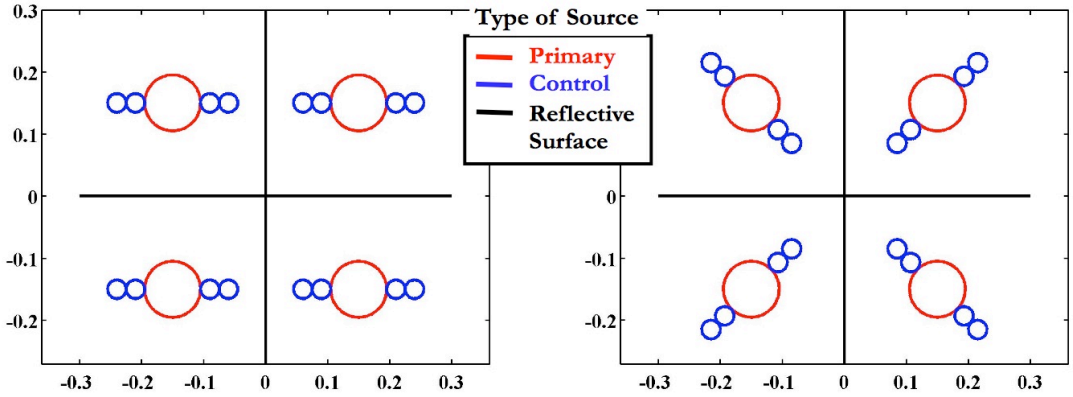


**Figure 5.17 Parallel (left) and diagonal control source configuration (right) for reflective surfaces**

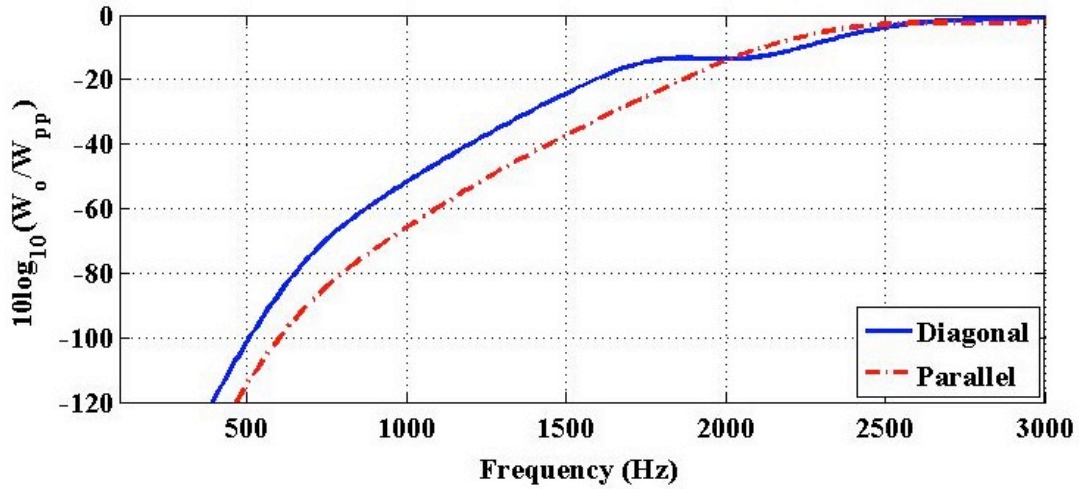


**Figure 5.18 Sound power attenuation as a function of frequency for the diagonal and parallel control source configurations with reflective surfaces**

## 5.3 Three-Dimensional Results

### 5.3.1 Four Control Sources

In cases where the mounting of control sources near a primary source is restricted to a single plane, the two-dimensional genetic algorithm is adequate. If mounting the control sources in the plane of the fan no longer becomes a constraint, another dimension can to be added to the analysis. The genetic algorithm was expanded to include a volume

around the primary source(s) instead of a plane. With the possible configurations expanded exponentially, the algorithm was not always able to converge to the same answer in a timely manner. Higher mutation probabilities were required as well as increases in generation size and the number of generations.

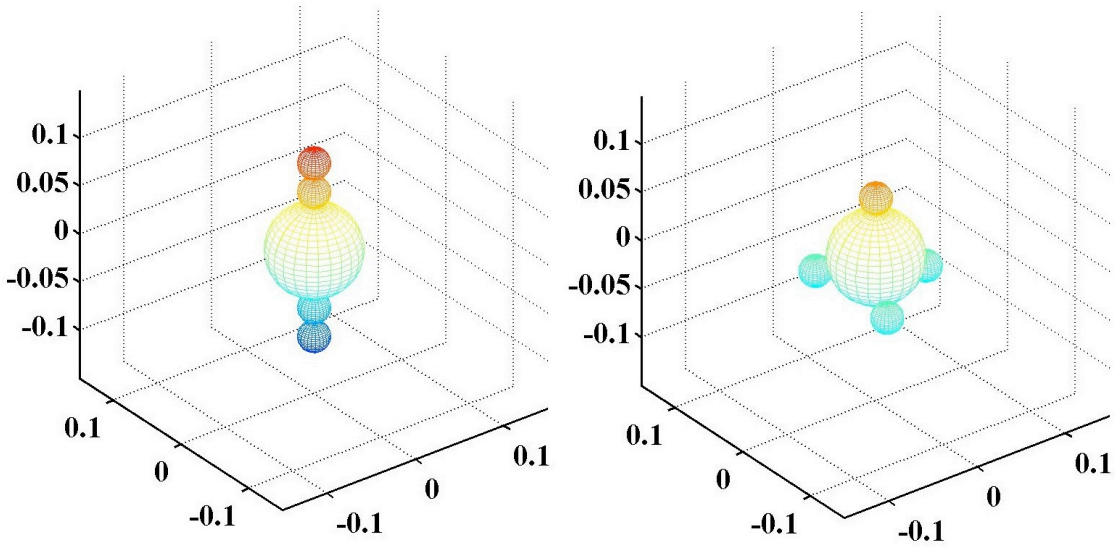


**Figure 5.19 Linear (left) and tetrahedral (right) configurations with four control sources and a single primary in three-dimensions**

When four control sources were allowed to control a single primary source, the algorithm would converge to two main configurations. These are shown in Figure 5.19. The large sphere centered at the origin is the primary source and the smaller spheres are the control sources. The color of the circles is used to show the elevation or the z component of the sphere. The first of these configurations is the same linear configuration found from the two-dimensional algorithm. The second is a tetrahedral arrangement of the control sources surrounding the primary source. For this solution, each source is the same distance from the primary source and the same distance from each of the other control sources. The algorithm is not able to converge to the same answer in all cases because the symmetric configuration is a local minimum that covers a

large portion of the design space. If the global minimum is isolated, as in this case, the algorithm will not find it without an adequate number of generations.

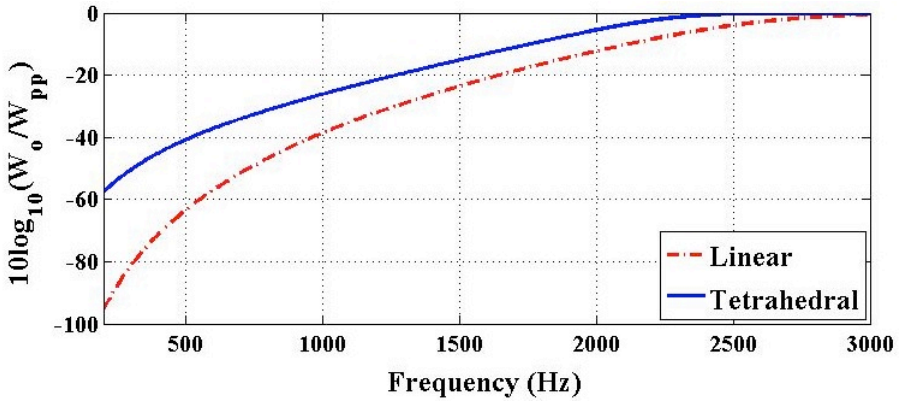


**Figure 5.20 Comparison of the sound power attenuation as a function of frequency for the linear and tetrahedral configurations**

The attenuation from the two different configurations shows that the linear case is superior to the tetrahedral configuration (see Figure 5.20). This held true for all frequencies of interest. The tetrahedral configuration is not only less practical to implement in an active noise control configuration, it also provides less sound power attenuation.

The superior attenuation achieved by the linear configuration is the result of having the two sets of control sources close to each other, allowing the control sources to have more mutual coupling. This is possible because, in this simulation, the control sources are smaller in size than the primary source. If all of the sources are the same size, the control sources in the linear configuration are farther apart and do not couple as well. The two configurations can be compared using a characteristic distance, *d*, which is also the diameter of the sources. This leads to compromised control and the linear configuration is no longer superior at all frequencies of interest. In Figure 5.21 the comparison of the attenuation is not dominated by one configuration. Instead, the linear

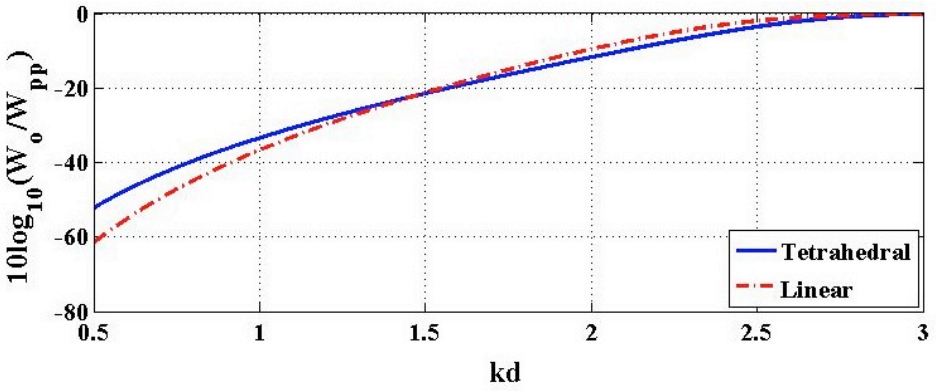


**Figure 5.21 Comparison of the sound power attenuation as a function of frequency for the linear and tetrahedral configurations using a single characteristic distance**

configuration is better for low frequency control while the tetrahedral configuration is superior at higher frequencies. The two are equal in performance when $kd = 1.468$.

The power radiation of the system for both the linear configuration and the tetrahedral configuration degenerates into a high order multipole. In the low frequency approximation ($kd < 1$) the tetrahedral configuration radiates as $kd^6$. The linear configuration radiates more like a $kd^8$ term (Figure 5.22). This high order radiation suggests that the control sources in the linear case are able to effectively cancel the monopole, dipole, and quadrupole radiation.

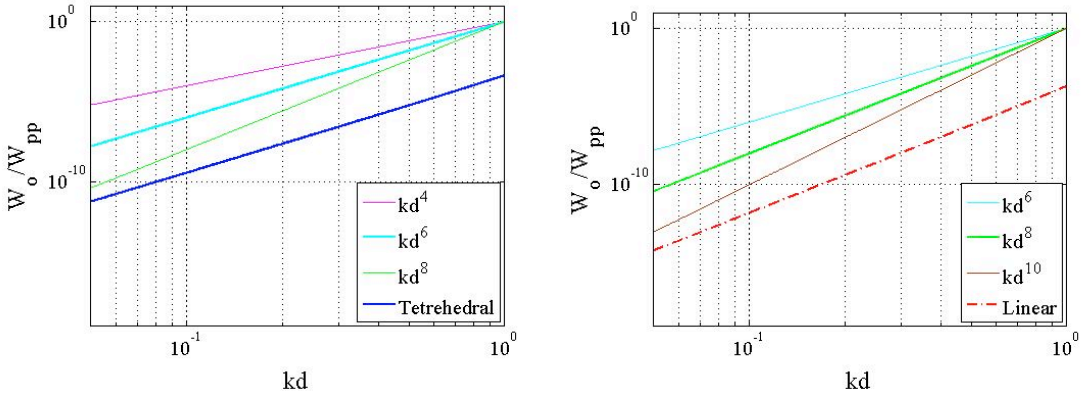


**Figure 5.22 Comparison of the sound power radiation of the tetrahedral (left) and the linear (right) configurations to powers of *kd***

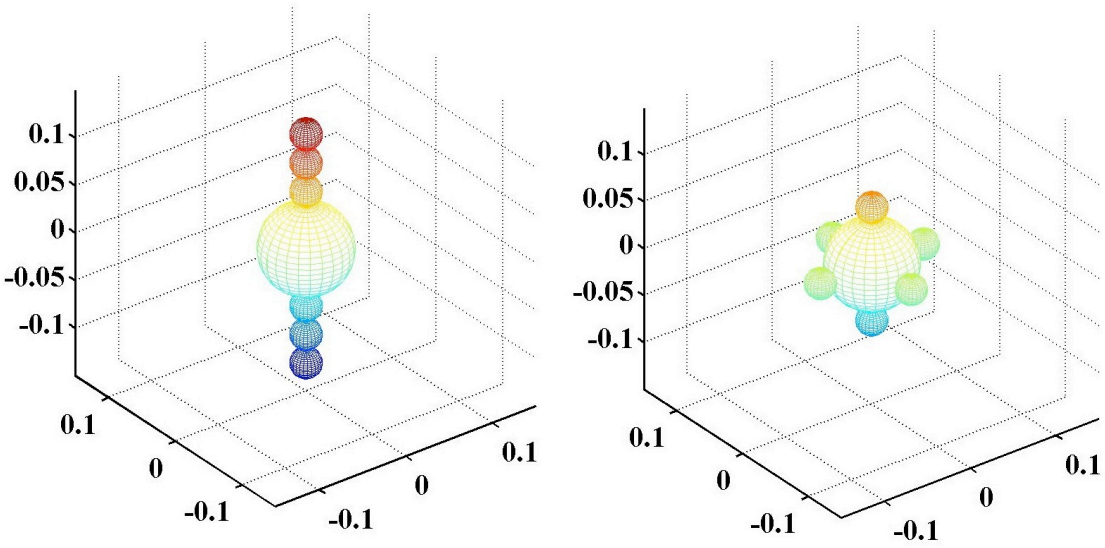


**Figure 5.23 Linear (left) and orthogonal longitudinal quadrupole (right) configurations of six control sources and a single primary source in three dimensions**

### 5.3.2 Six Control Sources

Radiation characteristics are similar for a setup with six control sources and a single primary source. The genetic algorithm will usually converge to two configurations that are quite different, shown in Figure 5.23. The linear configuration is similar to the four control sources in a linear configuration with two added sources. The second configuration is a modified orthogonal set of three longitudinal quadrupoles. When the control sources are smaller than the primary source, the linear configuration achieves better attenuation because the control sources can be closer to each other. When a single characteristic distance is used in both situations, the linear configuration has more attenuation at lower frequencies while the orthogonal quadrupoles achieve better attenuation at higher frequencies. Figure 5.24 shows the theoretical maximum attenuation achieved for both as a function of $kd$. The two configurations shown have the same achievable attenuation at $kd = 1.521$. If a low-frequency approximation is made, the linear configuration radiates as a higher-order source than the three orthogonal

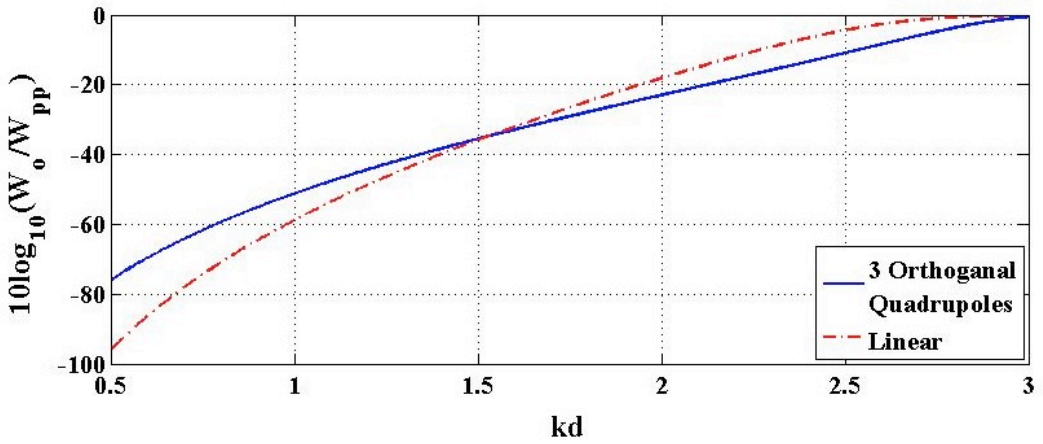


**Figure 5.24 Comparison of sound power attenuation as a function of frequency for the linear and orthogonal quadrupole configurations using a single characteristic distance**

quadrupoles. The three orthogonal quadrupole sources may be more difficult to implement than the linear configuration but the source strength required of each source at lower frequencies is much less as can be seen in Figure 5.25. The source strength of the closest sources in the linear configuration can reach a source strength almost equal to that of the primary source. If the control sources do not have the capabilities to reach these high levels without considerable distortion, the linear case may be less effective.

The power radiation characteristics of the linear six control sources has degenerated into a much higher-order source than both the four-control-source and the orthogonal-quadrupole arrangements. This higher-order source has completely eliminated the monopole, dipole, quadrupole, octupole, and beyond (Figure 5.26). This high-order source radiation is characteristic of the high levels of attenuation that are achievable using a linear configuration.

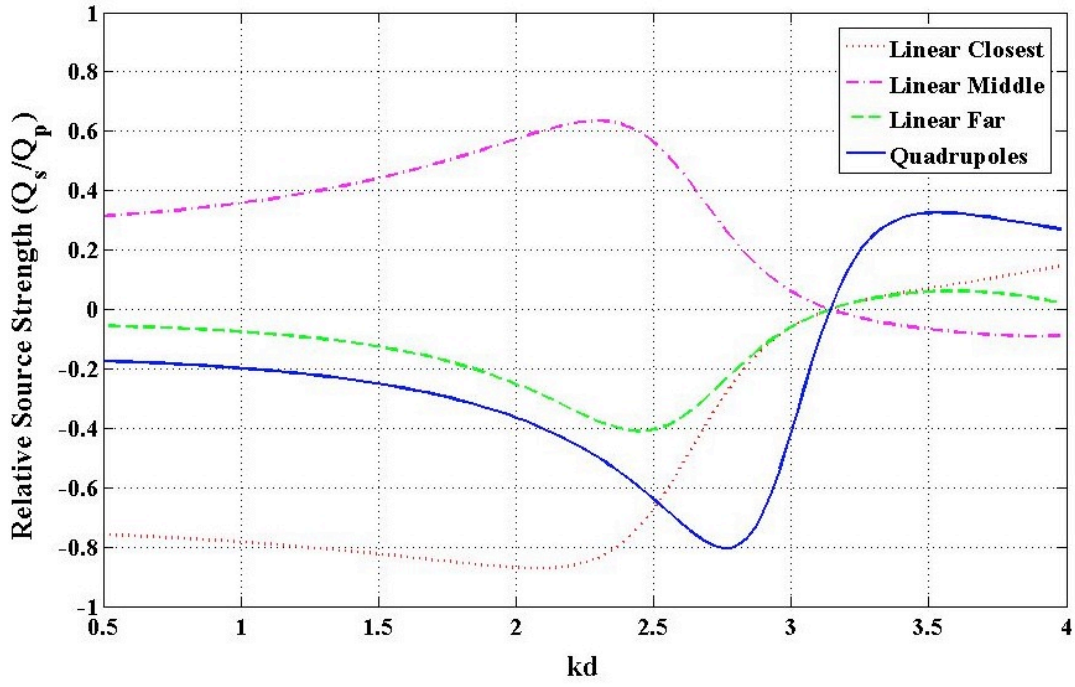


**Figure 5.25 Relative source strength required of the linear and orthogonal quadrupole configurations**

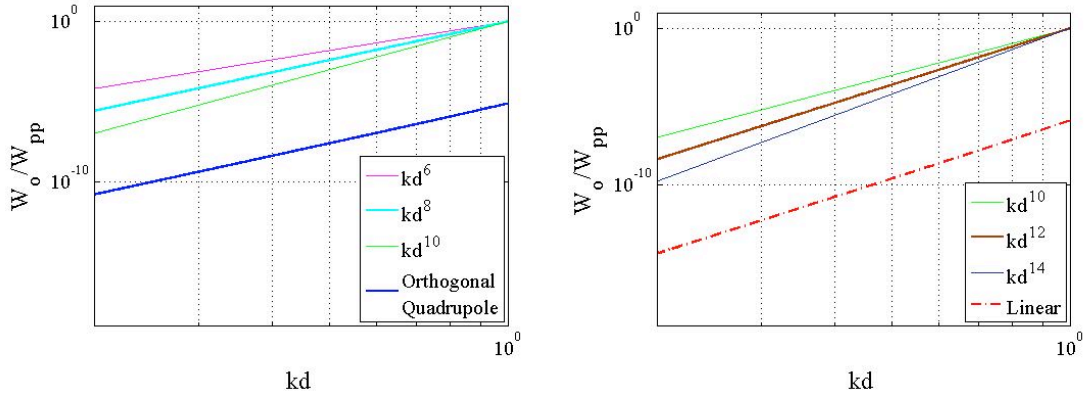


**Figure 5.26 Comparison of the sound power radiation of the orthogonal quadrupole (left) and the linear (right) configurations to powers of *kd***

## 5.4 Experimental Results

Experimental results were obtained using ANC on a single primary source. The experimental setup described in Chap. 4 was used. The acoustical measurements were taken in a hemisphere over the noise source with a 13-microphone array shown in Figure 5.27. The microphone array rotated around the system in 10-degree increments to form a

hemisphere. The radiated sound power of the system, at the frequency of interest, was calculated using the hemisphere and assuming symmetry of the measured hemisphere and the unmeasured hemisphere. The ANC system was used to control the noise from a 50 mm diameter loudspeaker radiating a sawtooth wave at 550 Hz. The symmetric configuration and the linear configuration were both used in the ANC system. Figure 5.28 shows the results of the symmetric case. A mesh grid was used to show the sound level, by distance from the center, in a given direction with no ANC system. The colored surface shows the sound radiation, by distance, from the center and color, when the ANC system is turned on. The three major frequencies of interest are shown with the sound power reduction in the title. Multiple trials were taken with a standard deviation of less than 0.1 dB.

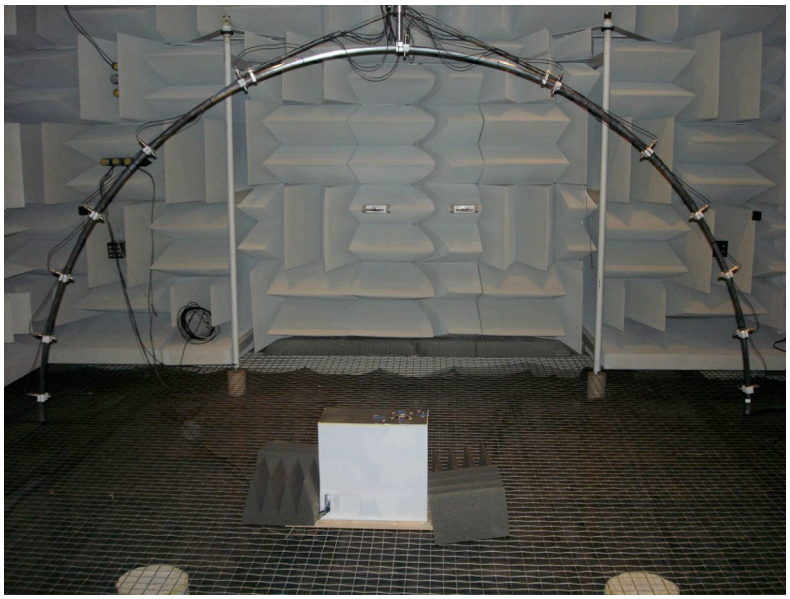

**Figure 5.27 Photograph of sound power measurement boom**

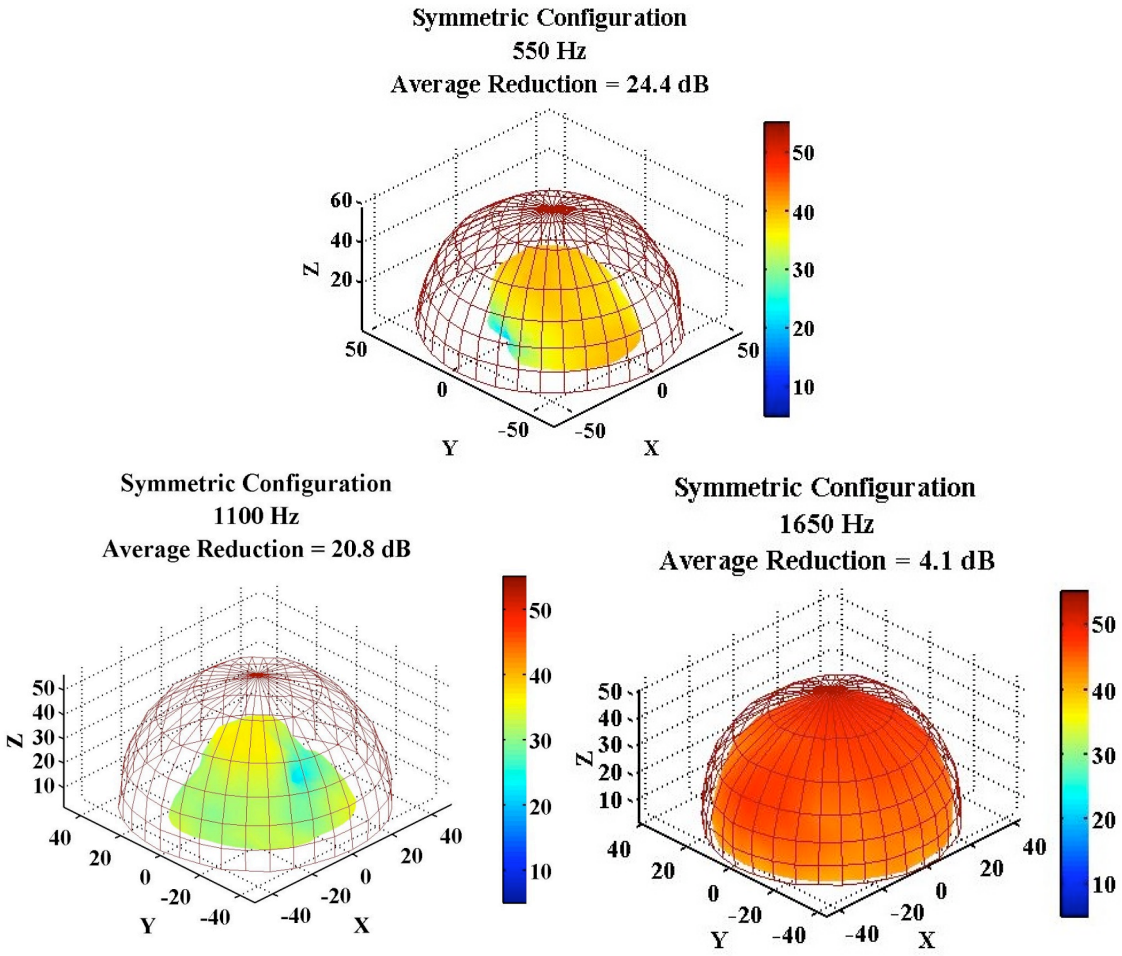


**Figure 5.28 Sound power reduction of four control sources configured symmetrically for 600 Hz (top), 1200 Hz (bottom left) and 1800 Hz (bottom right)**

Sound power reductions for the linear configuration are shown in Figure 5.29 with plotting techniques identical to the symmetric configuration. A comparison of the theoretical maximum attenuation and the experimental attenuation is shown in Tables 5.1 and 5.2. Both configurations achieved significant reductions in radiated power for the first two harmonics. In each case the linear configuration outperformed the symmetric configuration, in agreement with the theoretical results. The third harmonic showed significantly less sound power reduction due to the anti-aliasing filters with a cutoff frequency of 1400 Hz.

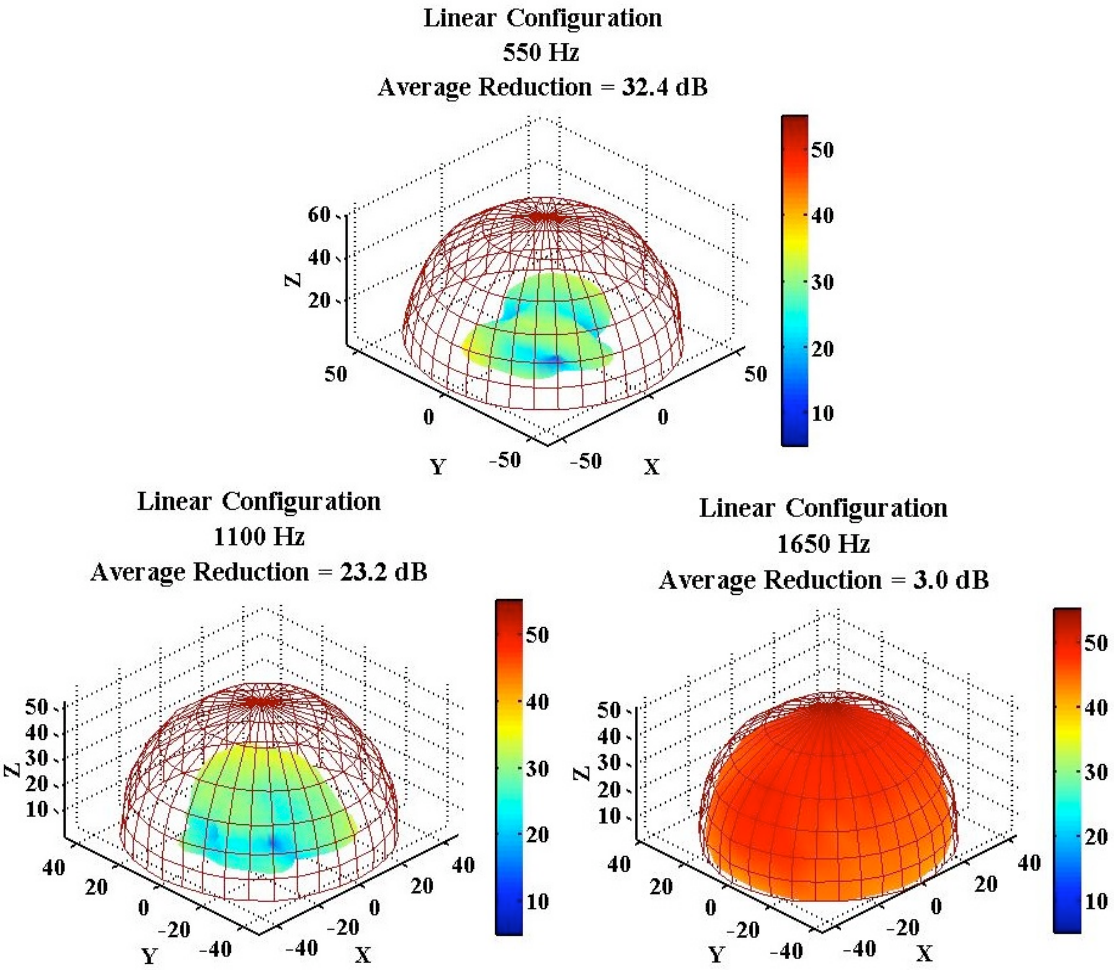


**Figure 5.29 Sound power reduction of four control sources configured linearly for 600 Hz (top), 1200 Hz (bottom left) and 1800 Hz (bottom right)**

| Theoretical Attenuation Sound Power (dB) | | | |
|---|---|---|---|
| | 550 Hz | 1100 Hz | 1650 Hz |
| Symmetric | 32.3 | 19.4 | 10.9 |
| Linear | 58.4 | 33.4 | 17.7 |

**Table 5.1 Maximum theoretical sound power attenuation for symmetric and linear configurations**

| Experimental Attenuation Sound Power (dB) | | | |
|---|---|---|---|
| | 550 Hz | 1100 Hz | 1650 Hz |
| Symmetric | 24.4 | 20.8 | 4.1 |
| Linear | 32.4 | 23.2 | 3.0 |

**Table 5.2 Experimental sound power attenuation for symmetric and linear configurations**

Further investigation was performed at other frequencies of interest. Active control was performed on sawtooth waves with these fundamental frequencies: 350 Hz, 450 Hz, 475 Hz, 525 Hz, 600 Hz, and 650 Hz. These frequencies were chosen to have little aliasing effects with the 2 kHz sample rate. The attenuation as a function for the fundamental and harmonics is shown in Figure 5.30 along with the theoretical attenuation curves by modeling each source as a point monopole. In a mid-frequency range the linear configuration did significantly better than the symmetric configuration. The amount of attenuation achieved by the linear configuration did not reach the theoretical limit, which is most likely due to the error sensor placement. Attenuation at high and low-frequency bands are due to other effects. Low-frequency attenuation was limited by the control actuators. The anti-aliasing filters used in the ANC system limited the amount of attenuation achieved at higher frequency ranges.

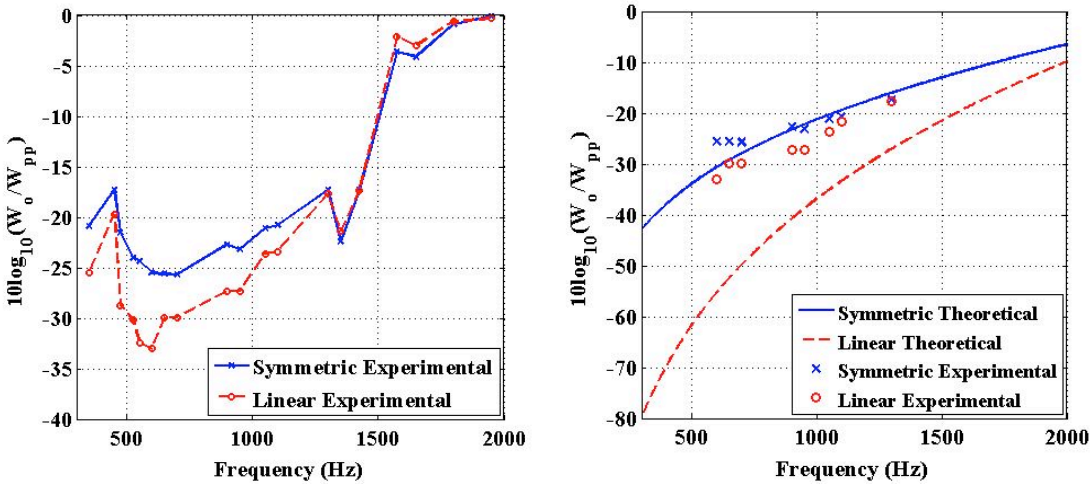


**Figure 5.30 Comparison of the experimental (left) and theoretical (right) attenuation as a function of frequency for the symmetric and linear configurations**

# Chapter 6

## Flow Field Investigation Results

### 6.1 Flow Field Investigation Introduction

The primary area of interest for the flow field investigation is along the near field null that is created by the four control sources and a single primary source. This near field null is where the error sensors must be placed in the near field to recreate the minimized sound power field.[26-28] An image of a fan with four surrounding control sources as well as a near field pressure plot is shown in Figure 6.1. One of the control sources is identified with a red arrow and a blue arrow indicates one of the error sensors. Superimposing the near field pressure plot onto the fan, we can see where the null (indicated by an area of dark blue) lies relative to the fan (see Figure 6.2). Finding the optimal area along this nodal area will provide the most attenuation.

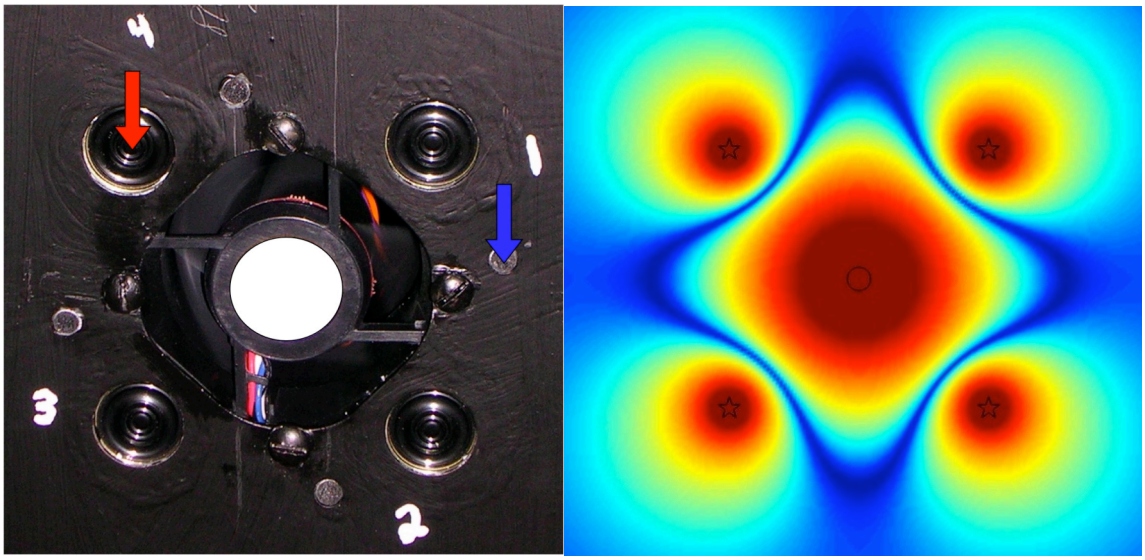


**Figure 6.1 Fan with control sources (red arrow) and error sensors (blue arrow) (left) and a near field pressure plot of four control sources surrounding a single primary source (right)**

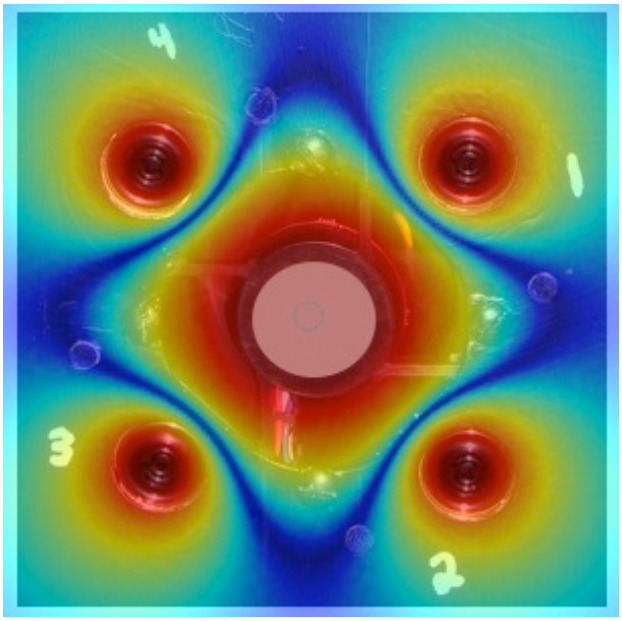


**Figure 6.2 Near field pressure plot superimposed over fan**

## 6.2 Flow Visualization Results

The qualitative flow visualization results showed that the airflow from the two fans is appreciably different. The airflow from the DC-powered fan was marked by an asymmetry due to the presence of an obstruction. The obstruction also added to the turbulent nature of the flow field in the near field of the fan. Even though the obstruction was necessary to mount the emitter-detector pair, the effects on the flow field seem to be unfavorable. The flow field of the PWM-powered fan, on the other hand, tended to be symmetric, less turbulent in the near field, and faster in flow speed. This allowed for a higher volumetric flow rate.

### 6.2.1 Flow Visualization of DC-Powered Fan

The asymmetry of the DC-powered fan flow field can be seen in Figure 6.3. This picture shows the DC-powered fan in arrangement 1 of the flow visualization with the fog introduced from inside of the enclosure. The fan then pulls the fog through the fan and out of the enclosure, from the bottom of the image toward the top of the image. The

white lines show where the outline of the main flow field lies. These lines are not symmetric which is due to the mounting of the emitter-detector pair. The top half of the emitter-detector pair is shown by the red arrow. The other half of the emitter detector pair is on the opposite side of the fan, out of view.

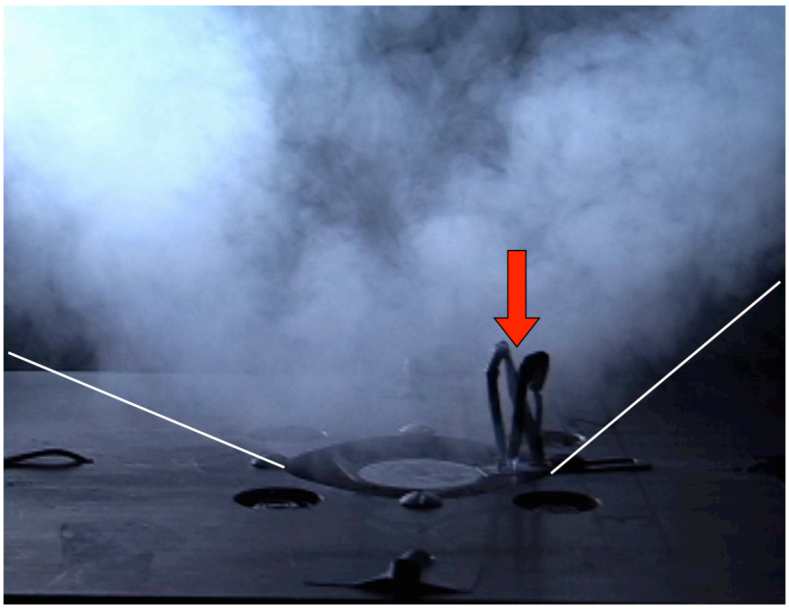

**Figure 6.3 Flow visualization of DC-powered fan in arrangement 1**

When the DC-powered fan is investigated from a different angle we see that the main flow field becomes even more asymmetric. Figure 6.4 shows the DC-powered fan in arrangement 2, again with the flow introduced from inside of the enclosure. The flow field is more asymmetrical with less airflow near the emitter-detector pair, shown by the red arrow. The airflow on the left side of the image is turbulent and stays quite close to the plate where the theoretical pressure null lies. Since the air is turbulent along the plate in this region, there may be a lower signal-to-noise ratio, resulting in lower attenuation being achievable with control.

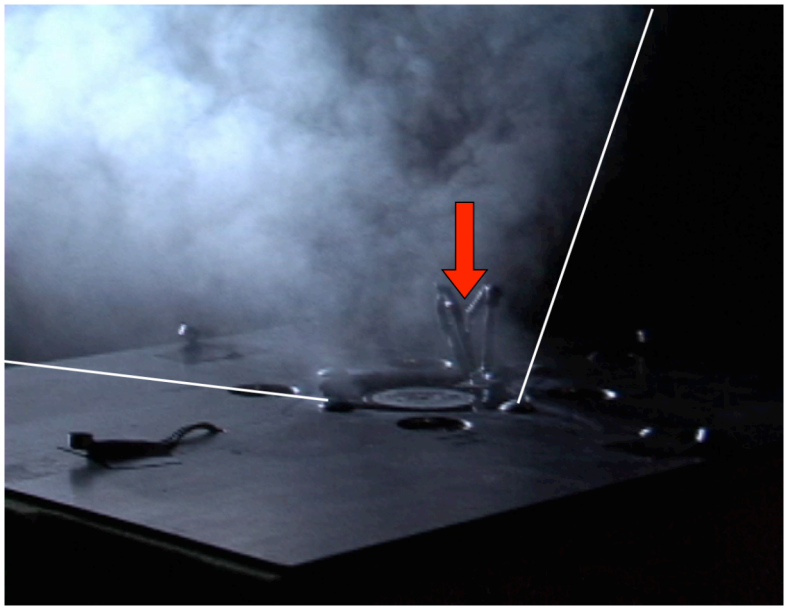

**Figure 6.4 Flow visualization of DC-powered fan in arrangement 2**

To investigate the airflow around the error sensors where the main air stream has a more vertical component and does not stay near the plate, the fog machine was used to introduce fog around the outside of the enclosure. Figure 6.5 shows the DC-powered fan in arrangement 1 with the fog machine outside of the enclosure. The air surrounding the fan originating from outside of the enclosure is entrained toward the fan in a laminar fashion, shown by the white line. Once the laminar air is pulled across some sort of obstruction (in this case a microphone) the air is disrupted, potentially causing a lower signal-to-noise ratio.

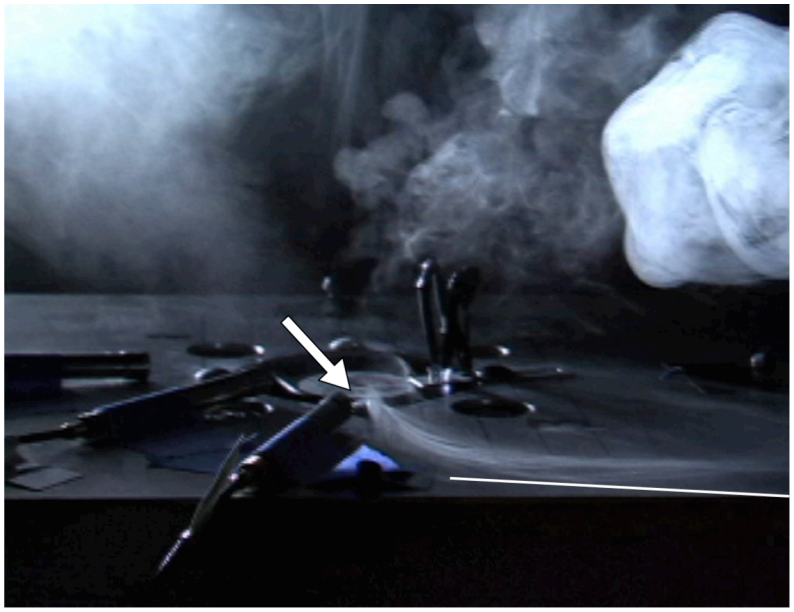

**Figure 6.5 Flow visualization of DC-powered fan in arrangement 1 with fog machine outside of enclosure**

### 6.2.2 Flow Visualization of PWM-Powered Fan

The flow field from the PWM-powered fan was more symmetric. Figure 6.6 shows the PWM fan in the flow visualization arrangement 1 with the fog machine introducing fog from inside of the enclosure. The fan is again pulling air from inside of the enclosure up through the fan, and out of the enclosure. White lines are used to outline the main column of air coming through the fan. These lines are more symmetrical and also have a more vertical component. Less air originating from inside of the enclosure created turbulent flow structures near the error sensors.

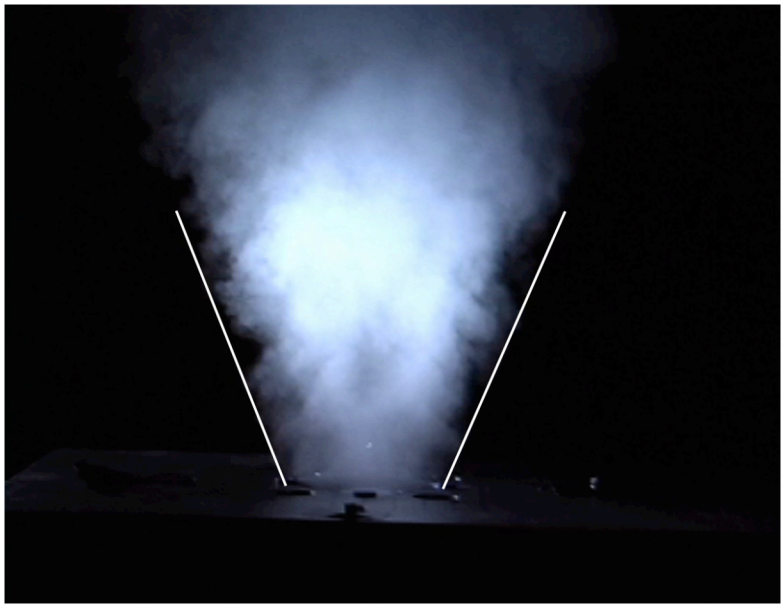

**Figure 6.6 Flow visualization of PWM-powered fan in arrangement 1**

The symmetrical nature of the main column of air coming through the fan held true for more than one angle of observation. Figure 6.7 shows the PWM-powered fan in the flow visualization arrangement 3. The main column of air coming through the fan was symmetric with little airflow staying close to the plate where the error sensors need to be mounted.

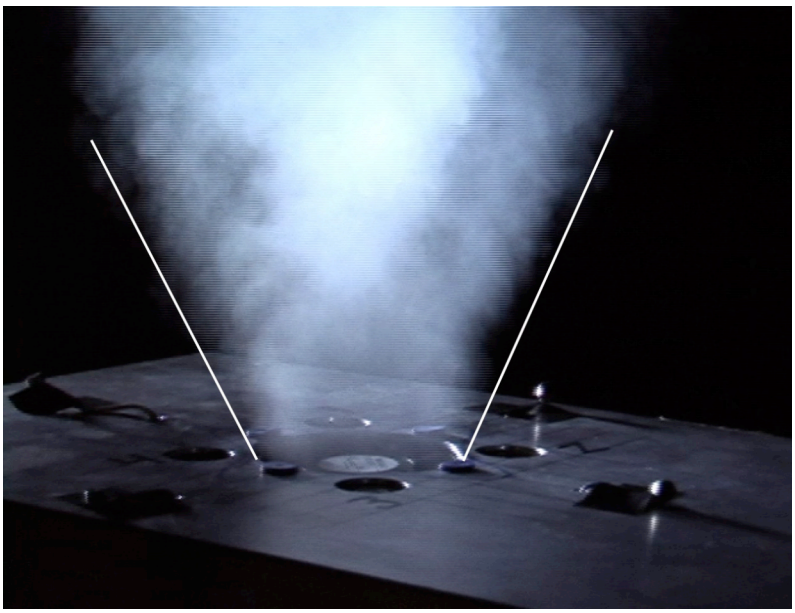

**Figure 6.7 Flow visualization of PWM-powered fan in arrangement 3**

When the fog was used to investigate the airflow originating from outside of the enclosure, entrained air can be seen. Figure 6.8 shows the PWM-powered fan in this arrangement. The entrained air tends to stay laminar until an obstruction is encountered, just as occurred with the DC-powered fan. Smaller electret microphones were used in this setup but they were still enough of a discontinuity to influence the airflow.

**Figure 6.8 Flow visualization of PWM-powered fan in arrangement 3 with fog machine outside of enclosure**

### 6.2.3 Flow Visualization Analysis

The qualitative data from the flow visualizations showed that the flow fields of the DC and PWM-powered fans are significantly different. Both fans, however, show trends toward entrained air in the region of interest. Surface mounting of the error sensors was also tested to determine if the entrained air across surface-mounted microphones would cause the air to stay laminar. The results from the surface-mounted microphones is presented in section 6.5.

## 6.3 Particle Image Velocimetry Results

The Particle Image Velocimetry (PIV) data shows quantitative information about the flow field of the two different fans. The vector plots shown are spatially down sampled for improved readability. For each image, a reference vector of 4 m/sec is shown. The length of this arrow changes as the scale of the vector plot changes. The error sensor is also shown on the vector plot by a red cylinder.

### 6-C.1 Particle Image Velocimetry of DC-Powered Fan

The DC-powered fan showed interesting characteristics in the near field, mostly due to the obstruction used to mount the emitter-detector pair. Figure 6.9 shows plane 1, the plane normal to the fan with an error sensor at the bottom of the plane, of the DC-powered fan. An image showing the flow coming out of the fan next to the PIV graph is shown. A reference arrow at the top of the PIV graph shows the equivalent length of 4 m/sec. The fan is supposed to be moving air from left to right. This does not seem to always occur, however. For the area in the vertical center of the plot, the velocity vectors are actually pointing towards the fan. Not only is the air surrounding the fan becoming entrained, a column of air extruding from the center of the fan is also becoming entrained. The main airflow exiting at a downward angle from the bottom of the fan does seem to correspond to the area along the plate where the error sensor needs to be mounted.

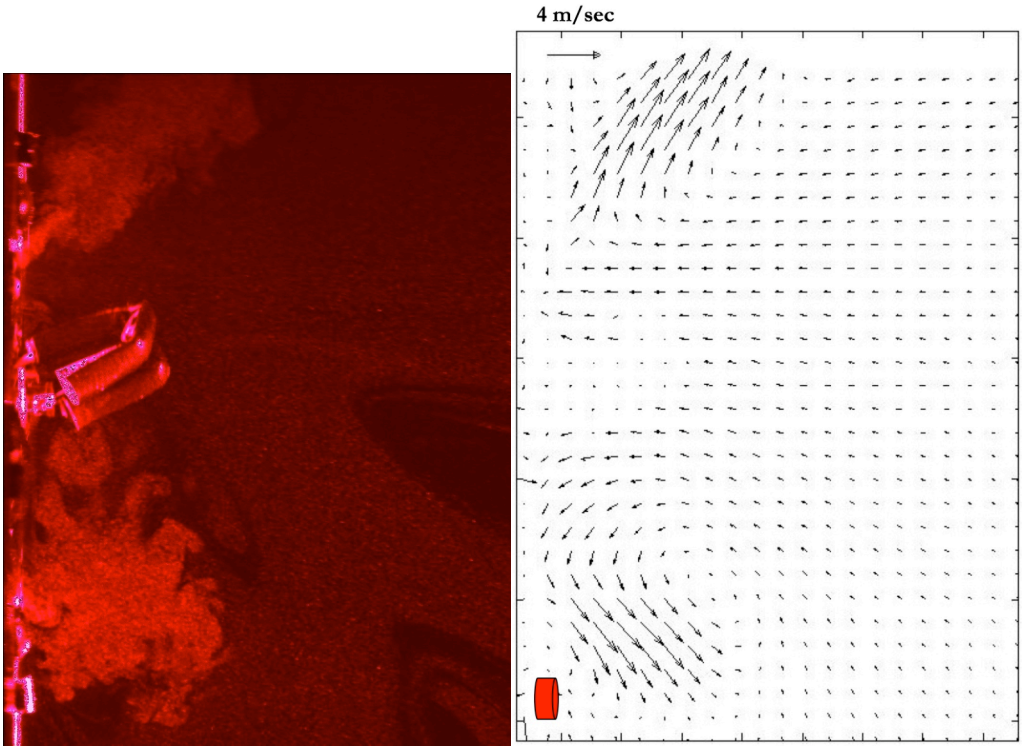


**Figure 6.9 PIV image (left) and vector plot (right) of DC-powered fan in plane 1**

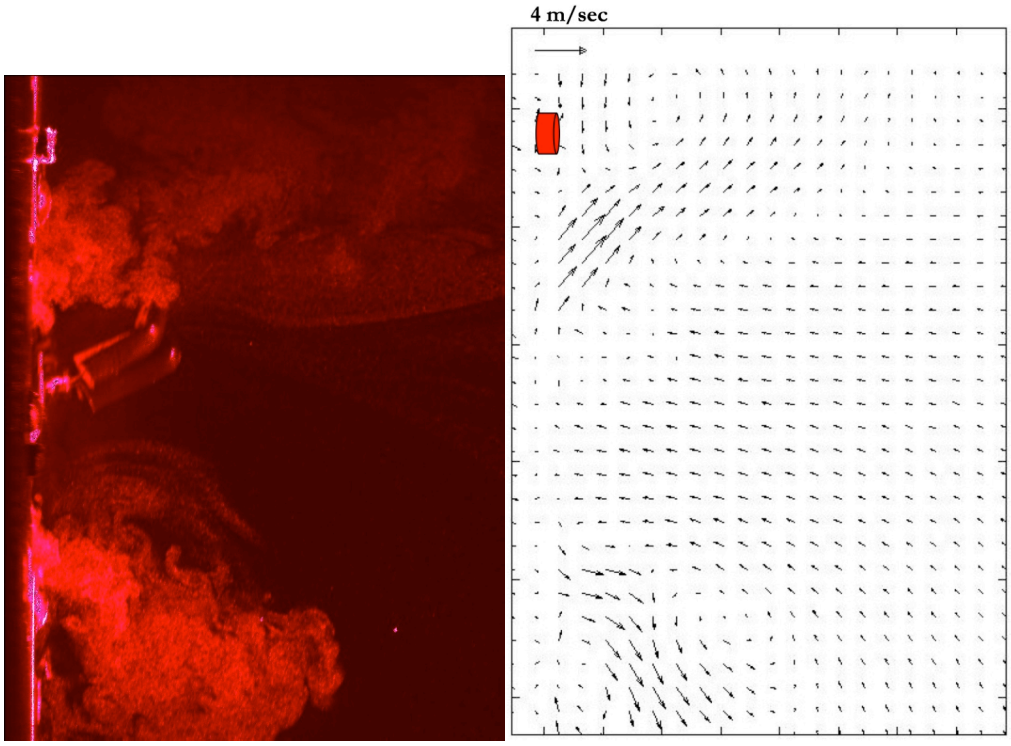


**Figure 6.10 PIV image (left) and vector plot (right) of DC-powered fan in plane 2**

Measurement plane 2, the plane normal to the fan with an error sensor at the top of the plane, shows similar entrainment from a column extruding from the center of the fan. A major difference between plane 1 and plane 2 is the vortices that are formed between the main airflow and the plane of the fan. These vortices can be seen in the top and bottom left corners of the PIV graph in Figure 6.10. They are located in the area where the error sensors need to be placed. The size of these vortices suggests that the error sensors are in the vicinity of the vortices if placed in the near field pressure null.

The third measurement plane shows other flow characteristics. Figure 6.11 shows an image of the plane of the fan, where the obstruction on the inlet of the fan stretching across the top right of the fan can be seen. The vector plots show that the obstruction causes much of the airflow in the direction of the obstruction to stay close to the plate by the large velocity vectors at the top right of the image (Figure 6.12). This holds true for air coming through the fan as well as air that is becoming entrained into the main airflow. The airflow in this area will cause the error sensors in this area to have more flow-induced noise and therefore a lower signal-to-noise ratio.

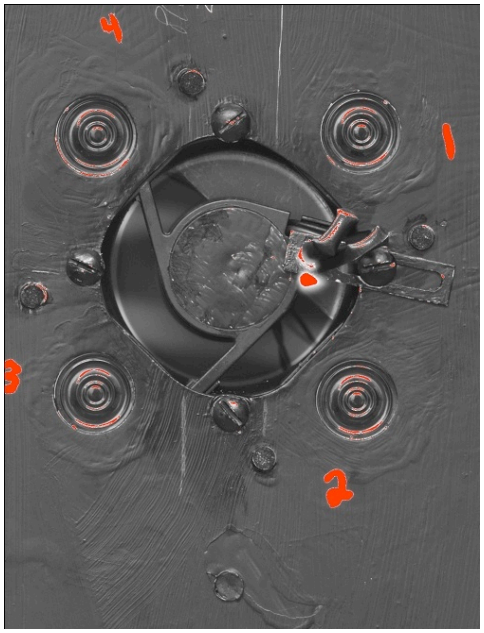


**Figure 6.11 Image of DC-powered fan in plane 3**

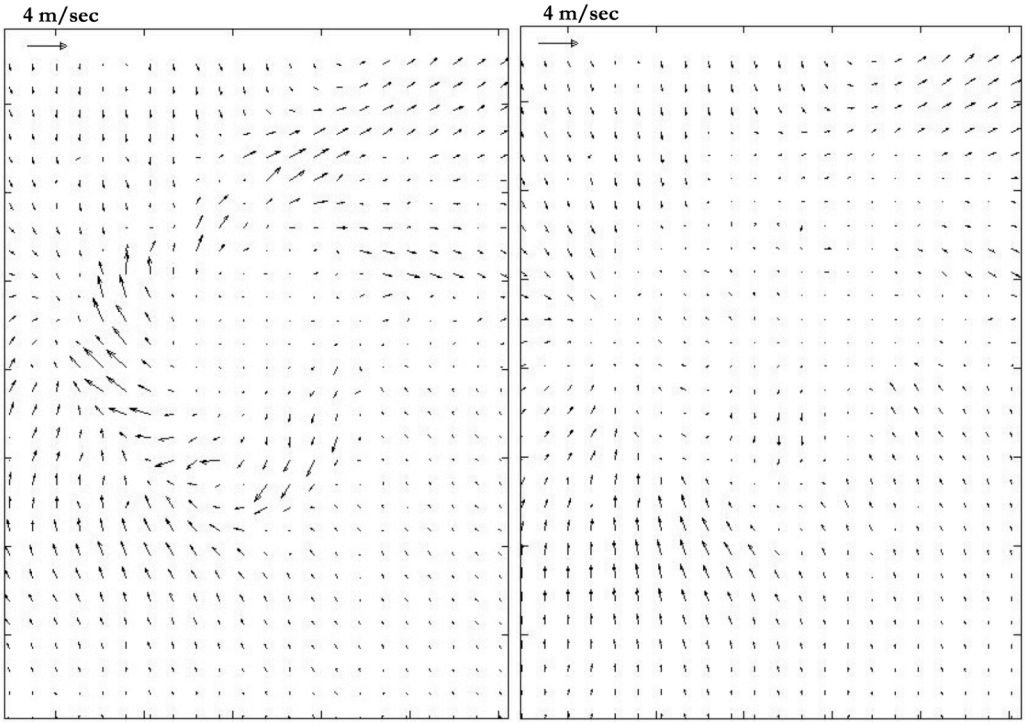


**Figure 6.12 PIV vector plot of the DC-powered fan in plane 3 with seed particles coming from inside (left) and outside (right) of the enclosure**

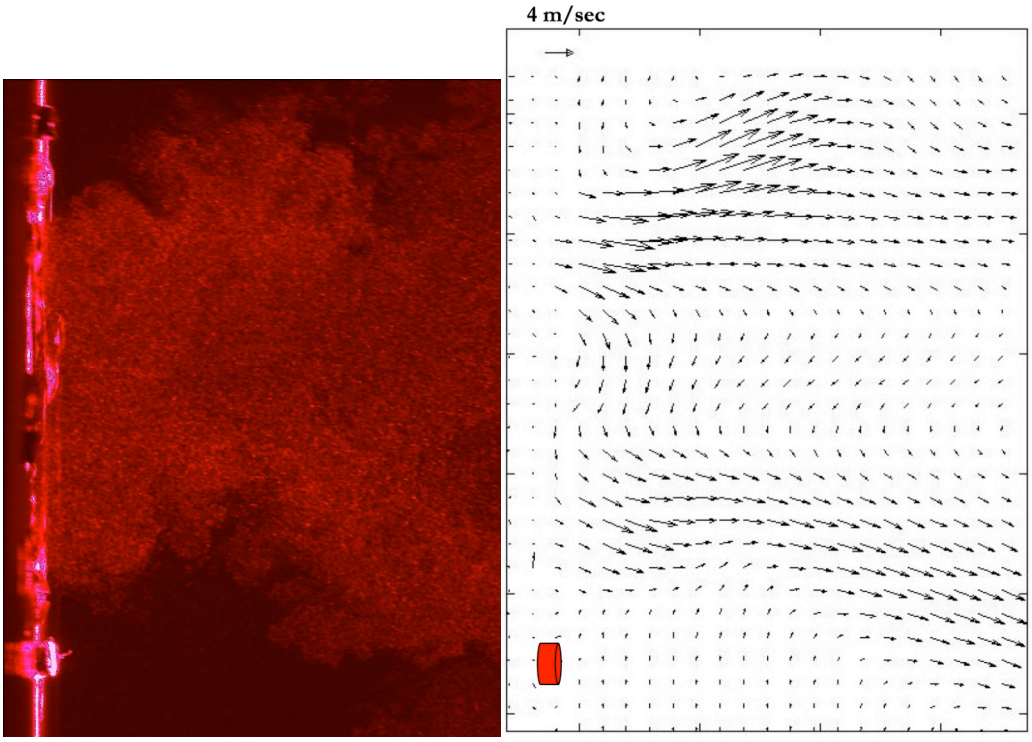


**Figure 6.13 Image (left) and PIV vector plot (right) of PWM-powered fan in plane 1**

### 6.3.2 Particle Image Velocimetry of PWM-Powered Fan

The PWM-powered fan showed stark contrasts to the DC-powered fan. With no obstruction in the main flow of air, the flow field behaves more as expected. Figure 6.13 shows an image of the PWM-powered fan in plane 1 along with the accompanying vector field. The flow field is much faster than the flow field of the DC-powered fan. This can be seen by the length of the 4 m/sec reference vector (Figure 6.13). The main airflow coming from the fan is in a column far away from the plane of the fan and the error sensor at the bottom of the image. Similar results were found for plane 2 of the PWM-powered fan.

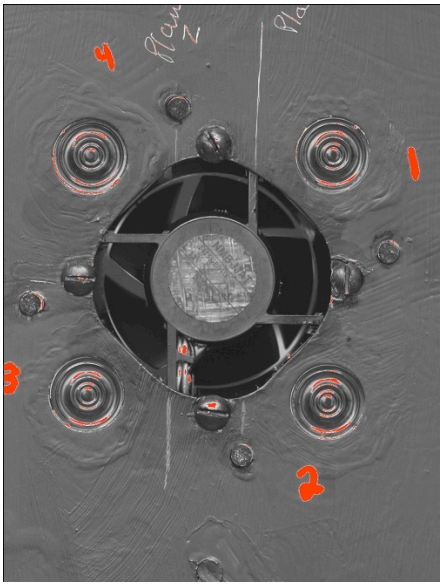


**Figure 6.14 Image of DC-powered fan in plane 3**

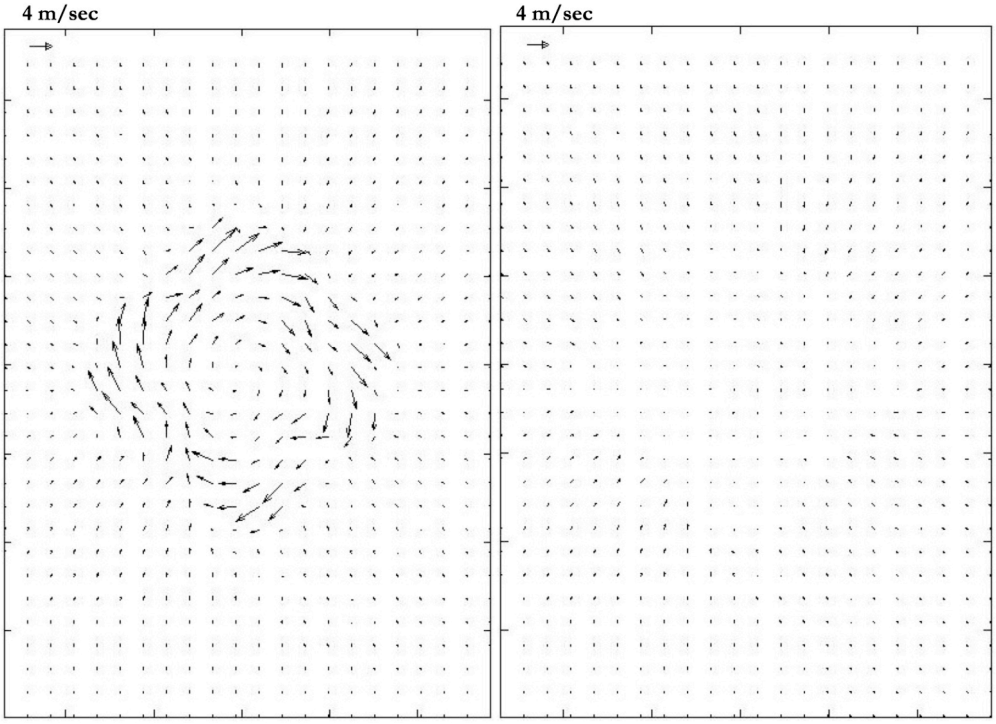


**Figure 6.15 PIV vector plot of the PWM-powered fan in plane 3 with seed particles coming from inside (left) and outside (right) of the enclosure**

Plane 3 also shows that the airflow from the PWM-powered fan does not significantly disrupt the air near the plane of the fan. Figure 6.14 shows an image of the PWM-powered fan in plane 3. Figure 6.15 shows that there is little airflow outside of the main column of air exiting the fan.

### 6.3.3 Particle Image Velocimetry Analysis

The PIV showed that the DC-powered fan creates more airflow near the error sensors, with potential for flow-induced noise along the plane of the fan where the error sensors need to be placed. The area in the direction of the obstruction is where most flow disturbances are present. The PWM-powered fan does not create significant flow in the plane of the fan.

## 6.4 Turbulence Intensity

Not only is it important to know where there is airflow, it is also important to know if the air flow is turbulent in the area of interest. If the airflow is laminar, the flow-induced noise will be minimal. If the air is turbulent, more flow-induced noise will be introduced.

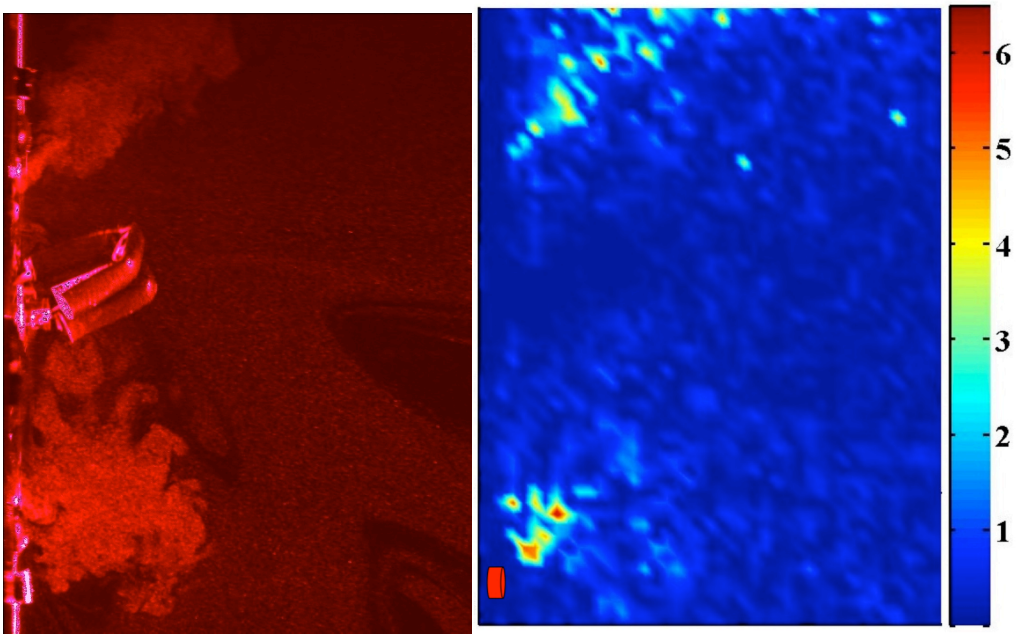


**Figure 6.16 Image (left) and turbulence intensity (right) of DC-powered fan in plane 1**

### 6.4.1 Turbulence Intensity of DC-powered Fan

The DC-powered fan showed more airflow in the potential error sensor locations. The turbulence intensity in plane 1 is greatest near the error sensor in the bottom left of the image (Figure 6.16). The highly turbulent nature of the airflow near the error sensor may result in a lower signal-to-noise ratio.

The turbulence intensity of plane 2 of the DC-powered fans shows similar results to that of plane 1 (Figure 6.17). Again, the higher amount of turbulent airflow in the area near the error sensors may result in a lower signal-to-noise ratio.

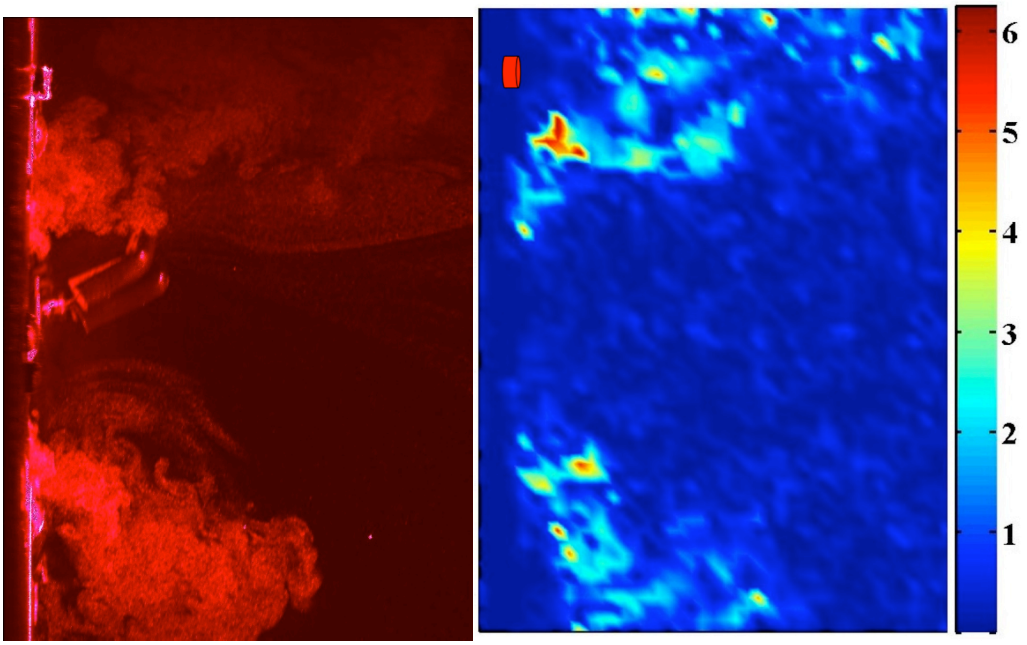


**Figure 6.17 Image (left) and turbulence intensity (right) of DC-powered fan in plane 2**

### 6.4.2 Turbulence Intensity of PWM-powered Fan

The PWM-powered fan showed that most of the turbulence intensity in the flow field occurred in the main airflow (Figure 6.18). This was not surprising after noting that little airflow was found near the plane of the fan. The low turbulence intensity shows

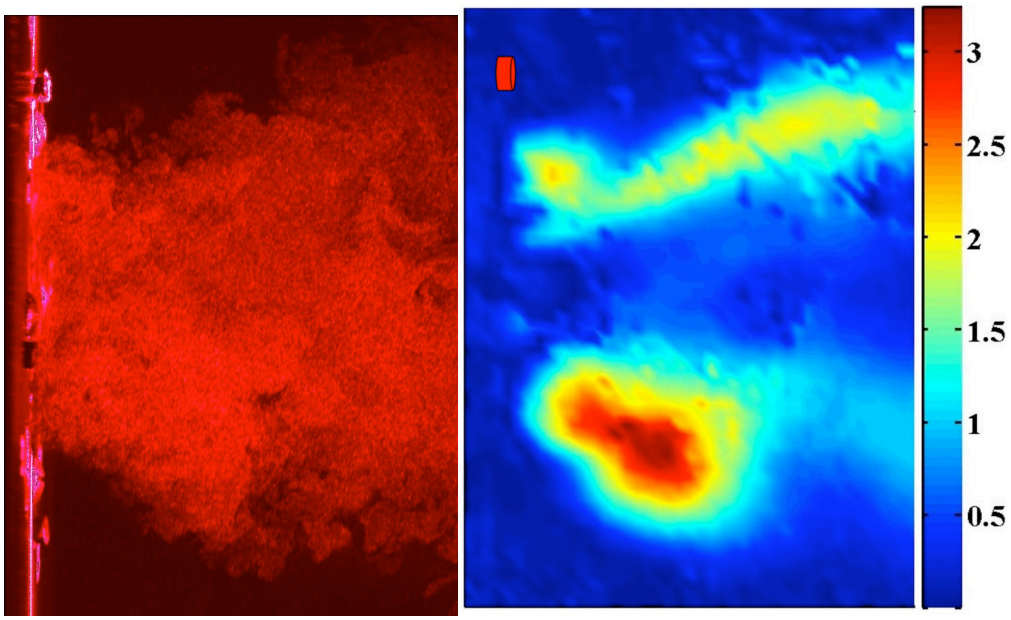


**Figure 6.18 Image (left) and turbulence intensity (right) of PWM-powered fan in plane 2**

that not only is there little airflow, but whatever airflow exists in the region near the error sensors likely does not contribute significantly to flow-induced noise.

### 6.4.3 Turbulence Intensity of Analysis

The turbulence intensity graphs show that mounting of the error sensors in the near field pressure null could introduce some flow-induced noise for the DC-powered fan. To avoid this result, the error sensors should be moved as far away from the fan while staying in the nodal area. This may help for the error sensor in plane 1 but may not have much of an effect for the error sensor in plane 2. The PWM-powered fan is not affected by the flow in the plane of the fan like the DC-powered fan. All areas along the nodal region should be nominally the same for the PWM-powered fan.

## 6.5 Surface-Mounting Error Sensors

The error sensors were surface mounted to minimize their disturbance in the entrained flow. Two images, one with regularly mounted error sensors and one with

surface-mounted error sensors, are shown in Figure 6.19. No noticeable differences were found in the PIV vector fields or the turbulence intensity plots. Time data were taken of the error sensors during the PIV data acquisition. These time data were used to calculate a signal-to-noise ratio that could be compared for the different cases. The signal-to-noise calculations were averaged over a 30-second interval using one-second subintervals.

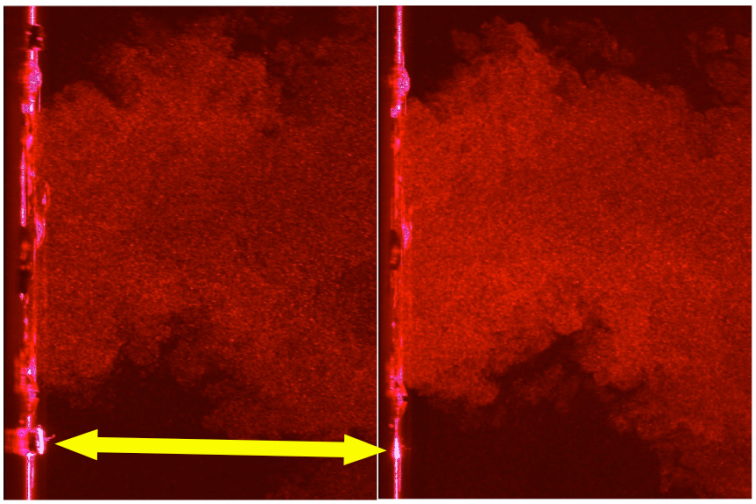

**Figure 6.19 Image of regularly-mounted (left) and flush-mounted (right) error sensor**

### 6.5.1 Surface-Mounting Error Sensors for DC-Powered Fan

Plots of the signal-to-noise ratio for the DC-powered fan are shown for regularly-mounted and flush-mounted error sensors in Figure 6.20. These plots seem to be quite similar. The peak of the BPF was quite narrow and the relative level of the signal-to-noise was similar in all cases for the four different channels of error sensors.

The average signal-to-noise ratio was taken at the BPF to obtain a single representative value of the signal-to-noise ratio of the entire test run. These averages were compared and the higher signal-to-noise ratio is highlighted in yellow in Table 6.1. The flush-mounting of the error sensors raised the average signal-to-noise ratio in every case. The average amount of signal-to-noise ratio that was gained by flush mounting the error sensors was only 1.3 dB while the fluctuation of the average signal-to-noise ratio

between tests was 0.7 dB. These data suggest, that even though flush-mounting the error sensors may partially remove them from the vicinity of the vortices created by the DC-powered fan, little will be gained in terms of the signal-to-noise ratio.

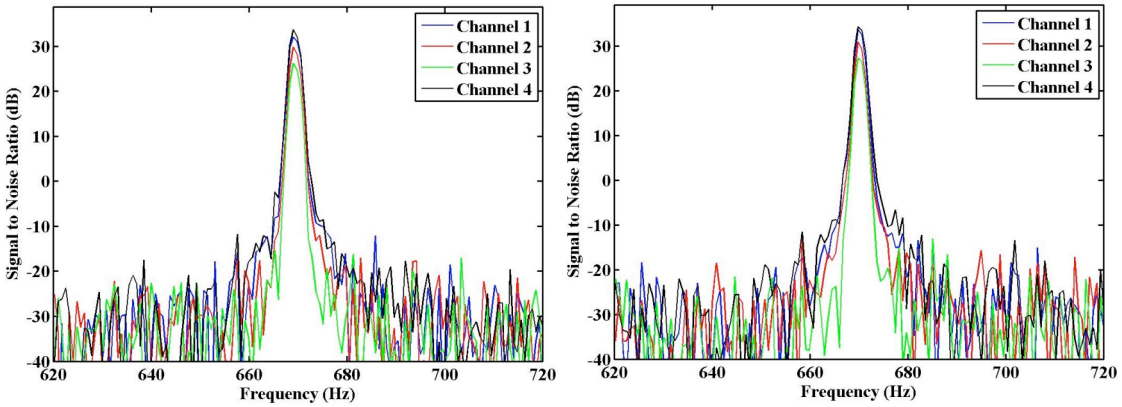


**Figure 6.20 Signal-to-noise ratio of regular (left) and flush mounted (right) error sensors for DC-powered fan**

| Average Signal to Noise Ratio for DC-Powered Fan (dB) | | |
|---|---|---|
| Test # | Flush Mounted | Regular |
| 1 | 31.6 | 30.4 |
| 2 | 30.3 | 29.5 |
| 3 | 31.4 | 29.3 |
| 4 | 31.3 | 29.8 |
| 5 | 30.9 | 30.2 |
| 6 | 31.6 | 29.9 |

**Table 6.1 Average signal-to-noise ratio (dB) for the DC-powered fan with regular and flush mounted error sensors**

### 6.5.2 Surface-Mounting Error Sensors for PWM-Powered Fan

The spectra of the signal-to-noise ratio from the PWM-powered fan was characterized by a wider frequency span for the BPF (see Figure 6.21). This suggests that the BPF was fluctuating over time. The relative signal-to-noise ratio of each of the error sensors changed more relative to one another than was the case for the DC-powered fan. The average of the signal-to-noise ratio did not show a trend as was the case for the DC-powered fan (see Table 6.2). This suggests that the flush-mounting of the error

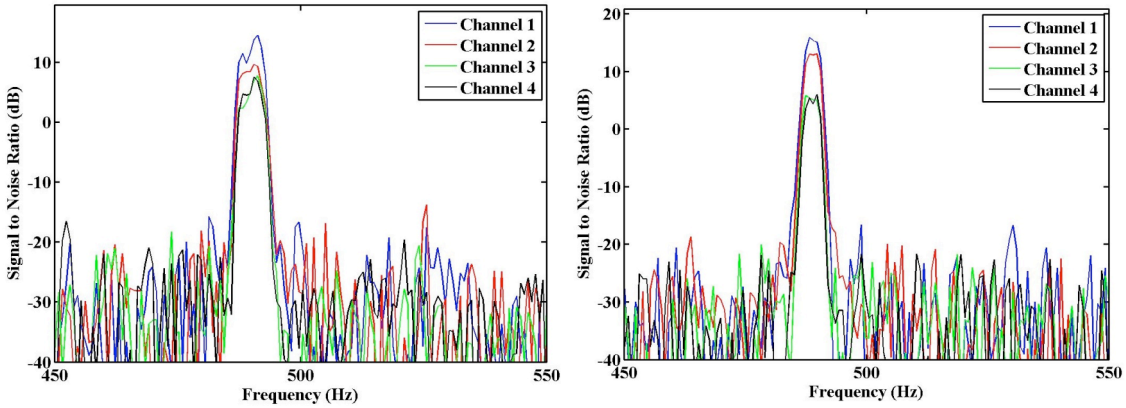


**Figure 6.21 Signal-to-noise ratio of regular (left) and flush mounted (right) error sensors for PWM-powered fan**

| Average Signal to Noise Ratio for PWM-Powered Fan (dB) | | |
|---|---|---|
| | Flush Mounted | Regular |
| 1 | 9.2 | 5.6 |
| 2 | 10.3 | 9.8 |
| 3 | 7.3 | 8.5 |
| 4 | 10.2 | 9.8 |
| 5 | 8.5 | 9.1 |
| 6 | 11.9 | 9.8 |

**Table 6.2 Average signal-to-noise ratio (dB) for the PWM-powered fan with regular and flush mounted error sensors**

sensors for the PWM-powered fan would not increase the signal-to-noise ratio. This is probably due to the lack of turbulent flow structures near the error sensors.

### 6.5.3 Surface-Mounting Error Sensors Analysis

Surface-mounting the error sensors showed consistent, but small improvement in the signal-to-noise ratio for the DC-powered fan. This is probably due to the presence of turbulent flow structures near the error sensors. The PWM-powered fan showed no gain in signal-to-noise ratio using the flush-mounted error sensors.

### 6.6 Active Noise Control Effect on Flow Field

Since the purpose of an air-moving device is to move a desired amount of air, if the noise suppression techniques adversely affect the air movement, the techniques would be counter-productive. The flow field while using an ANC system and without using an ANC system were compared. The PIV and turbulence intensity plots showed no significant differences. To get an idea of the effect on the flow through the fan, the average horizontal component of the velocity was determined for the PWM-powered fan. Figure 6.22 shows two different cases with the ANC system and without the system. These are indicative of all of the measurement runs. Significant changes in the axial component of the airflow were not created by the introduction of an ANC system. The amount of control that was achieved for these tests was marginalized due to the environment required for the PIV setup. Smaller than normal, but still significant, reductions were made to the BPF.

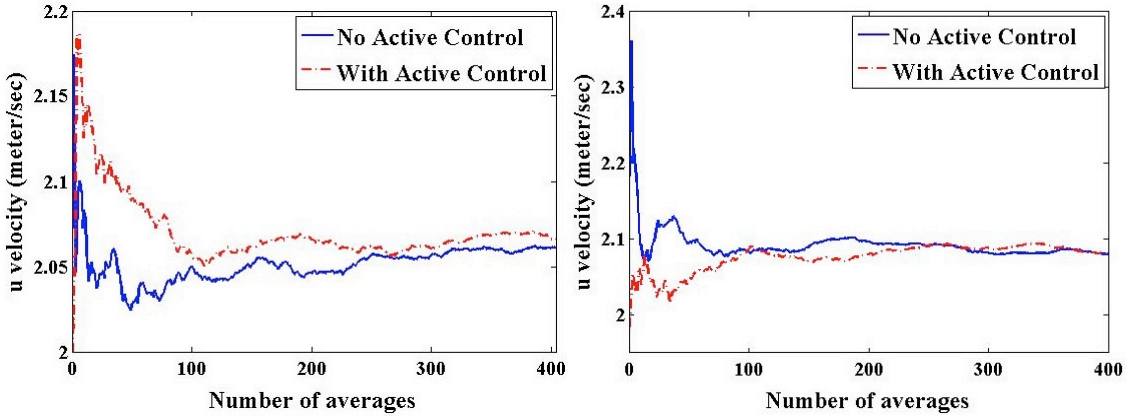


**Figure 6.22 Comparison of average axial velocity component with ANC and without ANC in two separate test runs of the PWM-powered fan**

# Chapter 7

# Conclusions and Recommendations

## 7.1 Summary

A genetic algorithm has been shown to be effective in finding the optimal control source locations for a specific primary source configuration radiating into free space. The algorithm was able to converge to a single control source configuration repeatedly when few (4 or fewer) control sources were used in two-dimensions. A modified crossover technique, referred to as parthenogenesis, was developed to obtain the global optimum with the given proximity constraints. When a single primary source system is constrained to two dimensions, the maximum sound power attenuation is achieved when using control sources in a linear configuration. The linear configuration is superior to the symmetric configurations over a broad low-frequency range. For high-frequency radiation, the symmetric configuration will obtain slightly superior attenuation; however, the frequency range where the symmetric source configuration will obtain better attenuation is not conducive to ANC. Experimental data showed that the linear configuration was superior for the fundamental and second harmonic of a loudspeaker. The increase in sound power attenuation by using the linear configuration was not as dramatic as the theoretical results. The limited increase in attenuation suggests that other limiting factors exist in the ANC system used in the experimental verification.

Expanding the search area to include three-dimensional control source configurations concludes with the linear configuration proving to be superior to other more symmetric configurations. The higher-order radiation characteristics of the linear configuration continues to hold true for four-control-source configurations as well as six-

control-source configurations. The genetic algorithm, however, was not always able to converge to the linear configuration due to the large number of possible configurations.

The introduction of reflective surfaces in the near field was modeled using image sources. The optimal control source configuration for a single primary source did not change with the introduction of the image sources.

Flow visualization techniques were used to find optimal error sensor locations along the near field pressure null created by the minimized sound power field. The two fans used in the experimentation showed dramatic differences in their respective flow fields. Neither fan, however, showed locations along the near field pressure null which would be superior to other locations. Vortex structures existed over the entire near field null of the DC-powered fan while there was little to no flow for the PWM-powered fan. The speed of the airflow near the error sensors also did not prove to be high enough to cause a dramatic Doppler shift that would introduce nonlinearities into the system. The flow field of both fans used in this experiment showed no significant change in the flow field due to the introduction of the ANC system.

The DC-powered fan, which was characterized by a more turbulent near field, showed a slight improvement to the signal-to-noise ratio by flush mounting the error sensors. Flush mounting the error sensors withdrew the error sensors from the vortices created by this fan.

### 7.2 Recommendations

This work constitutes a significant step forward in optimization of control sources for ANC in a free-field. A higher-order representation of the radiation from an axial fan

will allow the genetic algorithm used in this research to provide superior control source placement for the active control from the axial fan. A comparison of the optimal control source locations for multiple primary source models would also be valuable.

The experimental results obtained in the control source optimization did not agree well with the theoretical limits for the assumptions made. A deeper investigation into the merits of the assumptions and the limiting factors on the experimental ANC system used may lead to better agreement between the theoretical and experimental results. Experimental results from an ANC system on an axial fan in two and three dimensions would also supplement the theoretical work found in this study. Reflective surfaces could also be introduced and compared the theoretical findings in this study.

The error sensor optimization in this study has provided significant information regarding the flow field of the two fans investigated. A further study on the deviation of the flow fields created from other types of fans would be valuable. A more quantitative study on the effects of the ANC system on the volumetric flow rate could also contribute to the understanding of the effects of an ANC system on the flow field. An experimental study on how surface mounting the error sensors affects the amount of attenuation that is achieved in an ANC system would provide important information on the importance of mounting techniques.

## References


1. Maling, G.C., *Dimensional Analysis of Blower Noise.* Journal of the Acoustical Society of America, 1963. **35**(10): p. 1556-1564.
2. Maling, G.C., *Noise Generated by Small Air Moving Devices.* Inter-Noise 75, 1975: p. 275-282.
3. Maling, G.C., *Noise of Small Air-Moving Devices - State-Of-The-Art.* Proceedings of Fan Noise and International INCE Symposium, 1992: p. 57-67.
4. Bridelance, J.P., *Aeroacoustic Study of Axial Fans with Small Diameter. Analysis and Suppression of Instability Noise.* Inter-Noise 86, 1986: p. 141-146.
5. Huang, L. and J. Wang, *Acoustic Analysis of a Computer Cooling Fan.* Journal of the Acoustical Society of America, 2005. **118**(4): p. 2190-2200.
6. Neise, W., *Fan Noise - Generation Mechanisms and Control Methods.* Inter-Noise 88, 1988: p. 767-775.
7. Neise, W., *Review of Fan Noise Generation Mechanisms and Control Methods.* Proceedings of Fan Noise and International INCE Symposium, 1992: p. 45-56.
8. Shoji, S., *Sudy on the Noise Reduction in a Centrifugal Fan.* Inter-Noise 91, 1991: p. 71-74.
9. Lee, D.-J., W.-H. Jeon, and K.-H. Chung, *Development and Application of Fan Noise Prediction Method to Axial and Centrifugal Fans.* Proceedings of ASME FEDSM '02, 2002: p. 987-992.
10. Kaizer, L. and K. Wohrle, *Variable Speed Blowers - A Solution to Control the Noise of Computers.* Inter-Noise 89, 1989: p. 157-163.

11. Schmitt, J.G., D.A. Nelson, and J. Phillips, *An Automated System for the Acoutical and Aerodynamic Characterization of Small Air Moving Devices.* Noise-Con 2005, 2005.

12. Schmitt, J.G., *Alternate Construction Materials for the ISO 10302 Fan Test Plenum.* Inter-Noise 06, 2006.

13. Guedel, A., *Prediction of the Noise Installation Effect Induced by a Bend at the Inlet of an Axial Flow Fan.* Noise Control Engineering Journal, 2006. **54**(1): p. 21-26.

14. Kim, K.Y., M.G. Choi, D.J. Lee, W. Jeon, *Experimental Study of Noise Reduction and Improved Cooling Fan Performance in a PDP TV.* Noise Control Engineering Journal, 2006. **54**(1): p. 47-55.

15. Nelson, P.A. and S.J. Elliot, *Active Control of Sound*. 1992, San Diego: Academic Press Inc. 436.

16. Hansen, C.H. and S.D. Snyder, *Active Control of Noise and Vibration*. 1 ed. 1997, London: E & FN Spon. 1267.

17. Snyder, S.D., *Microprocessors for Active Control: Bigger Is Not Always Better.* Proceedings of the International Symposium on Active Control of Sound and Vibration, 1999. **1**: p. 45-62.

18. Neise, W. and G.H. Koopman, *Active Source Cancellation of the Blade Tone Fundamental and Harmonics in Centrifugal Fans.* Inter-Noise 88, 1988: p. 801-804.

19. Koopman, G.H., D.J. Fox, and W. Neise, *Active Source Cancellation of the Blade Tone Fundamental and Harmonics In Centrifugal Fans.* Journal of Sound and Vibration, 1988. **126**(2): p. 209-220.

20. Quinlan, D., *Active Control of Noise Radiated from Small Axial Flow Fans.* Inter-Noise 89, 1989: p. 479-482.

21. Quinlan, D.A., *Application of Active Control to Axial Flow Fans.* Noise Control Engineering Journal, 1992. **39**(3): p. 95-101.

22. Wang, J., L. Huang, and L. Cheng, *A Study of Active Tonal Noise Control for a Small Axial-Flow Fan.* Journal of the Acoustical Society of America, 2005. **117**(2): p. 734-743.

23. Gerard, A., A. Berry, and P. Masson, *Control of Tonal Noise from Subsonic Axial Fan. Part 2: Active Control Simulations and Experiments in Free Field.* Journal of Sound and Vibration, 2005. **288**: p. 1077-1104.

24. Lauchle, G.C., J.R. MacGillivray, and D.C. Swanson, *Active Control of Axial-Flow Fan Noise.* Journal of the Acoustical Society of America, 1997. **101**(1): p. 341-349.

25. Schulz, J., W. Neise, and M. Moser, *Active Control of the Blade Passage Frequency Noise Level of an Axial Fan with Aeroacoustic Sound Sources.* Noise Control Engineering Journal, 2006. **54**(1): p. 33-40.

26. Gee, K.L. and S.D. Sommerfeldt, *A Compact Active Control Implementation for Axial Cooling Fan Noise.* Noise Control Engineering Journal, 2003. **51**(6): p. 325-334.

27. Gee, K.L., *Multi-Channel Active Control of Axial Cooling Fan Noise*, MS Thesis in *Physics and Astronomy*. 2002, Brigham Young University: Provo. p. 126.

28. Gee, K.L. and S.D. Sommerfeldt, *Application of Theoretical Modeling to Multichannel Active Control of Cooling Fan Noise.* Journal of the Acoustical Society of America, 2004. **115**(1): p. 228-236.

29. Monson, B.B., *Optimization of Active Noise Control for Small Axial Cooling Fans*, MS Thesis in *Physics and Astronomy*. 2006, Brigham Young University: Provo. p. 63.

30. Green, M.J., *Feedback Applications In Active Noise Control for Small Axial Cooling Fans*, MS Thesis in *Physics and Astronomy*. 2006, Brigham Young University: Provo. p. 69.

31. Nelson, P.A., A.R. Curtis, S.J. Elliot, A.J. Bullmore, *The Minimum Power Output of Free Field Point Sources and the Active Control of Sound.* Journal of Sound and Vibration, 1987. **116**(3): p. 397-414.

32. GoldBerg, D.E., *Genetic Algorithms in Search, Optimization, and Machine Learning*. 1989, Reading, Massachusetts: Addison-Wesley Publishing Company, Inc. 412.

33. Hansen, C.H., M.T. Simpson, and B.S. Cazzolato, *Genetic Algorithms for ASVC Systems*, in *Active Sound and Vibration Control*, S.V. Osman Tokhi, Editor, The Institution of Electrical Engineers: London. p. 185-220.

34. Wang, B.-T., *Optimal Placement of Microphones and Piezoelectric Transducer Actuators for Far field Sound Radiation Control.* Journal of the Acoustical Society of America, 1996. **99**(5): p. 2975-2984.

35. Howard, C.Q., R. Morgans, C.H. Hansen, A.C. Zander, *A Tool for the Optimisation of Vibro-Acoustic Systems Using a Parallel Genetic Algorithm and a Distributed Computing Network.* Noise Control Engineering Journal, 2005. **53**(6): p. 256-267.

36. Martin, T. and A. Roure, *Active Noise Control of Acoustic Sources Using Spherical Harmonics Expansion and a Genetic Algorithm: Simulation and Experiment.* Journal of Sound and Vibration, 1998. **212**(3): p. 511-523.

37. Pottie, S. and D. Botteldooren, *Optimal Placement of Secondary Sources for Active Noise Control Using a Genetic Algorithm.* Inter-Noise 96, 1996: p. 1101-1104.

38. Diamantis, Z.G., D.T. Tsahalis, and I. Borchers, *Optimization of an Active Noise Control System Inside an Aircraft, Based on the Simultaneous Optimal Positioning of Microphones and Speakers, with the Use of a Genetic Algorithm.* Computational Optimization and Applications, 2002. **23**: p. 65-76.

39. Elliot, S.J., P.A. Nelson, I.M. Stothers, C.C. Boucher, *In-Flight Experiments On the Active Control of Propeller-Induced Cabin Noise.* Journal of Sound and Vibration, 1990. **140**(2): p. 219-238.

40. Simpson, M.T. and C.H. Hansen, *Use of Genetic Algorithms to Optimize Vibration Actuator Placement for Active Control of Harmonic Interior Noise in a Cylinder with Floor Structure.* Noise Control Engineering Journal, 1996. **44**(16-19): p. 16.

41. Li, D.S., L. Cheng, and C.M. Gosselin, *Optimal Design of PZT Actuators in Active Structural Acoustic Control of a Cylindrical Shell with a Floor Partition.* Journal of Sound and Vibration, 2004. **269**: p. 569-588.

42. Manolas, D.A., I. Borchers, and D.T. Tsahalis, *Simulataneous Optimization fo the Sensor and Actuator Positions for an Active noise and/or Vibration Control System Using Genetic Algorithms, Applied in a Donier Aircraft.* Engineering Computations, 2000. **17**(5): p. 620-630.

43. Li, D. and M. Hodgson, *Optimal Active Noise Control in Large Rooms Using a "Locally Global" Control Strategy.* Journal of the Acoustical Society of America, 2005. **118**(6): p. 3653-3661.

44. Baek, K.H. and S.J. Elliot, *Natural Algorithms for Choosing Source Locations In Active Control Systems.* Journal of Sound and Vibration, 1995. **186**(2): p. 245-267.

45. Katsikas, S.K., D. Tsahalis, and D. Manolas, *A Genetic Algorithm for Active Noise Control Actuator Positioning.* Mechanical Systems and Singal Processing, 1995. **9**(6): p. 697-705.

46. Tsahalis, D.T., S.K. Katsikas, and D.A. Manolas, *A Genetic Algorithm for Optimal Positioning of Actuators in Active Noise Control: Resuts from the ASANCA Project.* Aircraft Engineering and Aerospace Technology, 2000. **72**(3): p. 252-258.

47. Zander, A.C. and C.H. Hansen, *A comparison of Error Sensor Strategies for the Active Control of Duct Noise.* Journal of the Acoustical Society of America, 1993. **94**(2): p. 841-848.

48. Berry, A., X. Qiu, and C.H. Hansen, *Near field Sensing Strategies for the Active Control of the Sound Radiated from a Plate.* Journal of the Acoustical Society of America, 1999. **106**(6): p. 3394-3406.

49. Parkinson, A., *Optimization Methods in Engineering Design.* ME 575 Course Notes, 2007. Brigham Young University.

50. Sommerfeldt, S.D., *Active Noise Control.* Physics 566 Course Notes, 2004. Brigham Young University.

51. Raffel, M., C.E. Willert, and J. Kompenhans, *Particle Image Velocimetry: A Practical Guide*. Experimental Fluid Mechanics, ed. R.J. Adrian, et al. 1998, Berlin: Springer.

52. Gharib, M. and D. Daribi, *Digital Particle Image Velocimetry*, in *Flow Visualization: Techniques and Examples*, A.J. Smits and T.T. Lim, Editors. 2000, Imperial College Press: London. p. 123-147.

53. Lee, S.-J., J. Choi, and J.-H. Yoon, *Phase-Averaged Velocity Field Measurements of Flow Arround an Isolated Axial-Fan Model.* Journal of Fluids Engineering, 2003. **125**: p. 1067-1072.

54. Thomson, S., *Experimental Flow Measurements.* ME 695R Course Notes, 2006. Brigham Young Univesity.

55. Monson, B., *Optimization of Active Noise Control for Small Axial Cooling Fans.* Noise Control Engineering Journal, 2007. **55**(4).

# Appendix 1

## Particle Size Considerations

### A1 Sedimentation and Inertial Effects

The particles that are used in PIV measurements must be small enough that they will follow the flow field. If the particles become too small, they will no longer be visible for the analysis. For these purposes, the largest possible particles that will still meet the error requirements are desired. The two major reasons that particle size will add error into the measurement are sedimentation and inertial effects.

Sedimentation is due to the gravitational force causing a vertical component of velocity on the particle. The more gravitational pull on the particle, the more sedimentation will be present. If the velocity component added to the particle is not insignificant compared to the flow field velocity, the error introduced by sedimentation must be accounted for. The maximum velocity that sedimentation can cause is the terminal velocity, $u_\infty$. At the terminal velocity there is no acceleration and the sum of the net forces on the particle is zero. The gravitation force, $mg$, the buoyant force, $F_B$, and the drag force, $F_D$, can be related by the equation,

$$mg = F_D + F_B, \tag{A1.1}$$

where $m$ is the mass of the particle and $g$ is the gravitational constant. The equation,

$$F_B = \frac{4}{3}\pi a^3 \rho_f g, \tag{A1.2}$$

relates the buoyant force to the radius of the particle, $a$, and the density of the fluid, $\rho_f$. Using the coefficient of drag for a sphere, the drag force can be related to the terminal velocity, $u_\infty$, and the dynamic fluid viscosity, $\mu$, by the equation

$$F_D = 6\pi u_\infty a\mu. \tag{A1.3}$$

Substituting equations A1.2 and A1.3 into A1.1 and rearranging the terms, the terminal velocity can be related to the fluid density, $\rho_f$, and the particle density, $\rho_p$:

$$u_\infty = \frac{2}{9}\frac{a^2 g}{\mu}(\rho_p - \rho_f) \quad . \tag{A1.4}$$

Inertial effects are the other major cause of particle size-induced error. The inertial effects of the particle are the initial time delay that it takes for the stationary particle to reach the velocity of the flow field. The difference in the velocity at time, t, of the fluid, $u_f(t)$ and the velocity of the particle, $u_p(t)$, is

$$u_f(t) - u_p(t) = \left(u_f(0) - u_p(0)\right)e^{-\frac{\tau}{t}} \tag{A1.5}$$

where $u_f(0)$ and $u_p(0)$ are the initial fluid and particle velocities, respectively. The term $\tau$ is defined as

$$\tau = \frac{-2a^2\rho_p}{9\mu} \quad . \tag{A1.6}$$

The particle velocity will reach the flow velocity exponentially.

# Appendix 2

## Number of Averages

### A2 Running Average

Time and resources can limit the number of image pairs taken in an experiment. The limiting factors should not give an inadequate number of averages to obtain an accurate representation of the flow field. In this experiment, approximately 400 image pairs were used in each configuration setup. With the ability to take 5 image pairs per second, this corresponded to about 80 seconds per run. Due to storage limitations, data acquisition of the 400 image pairs was taken in consecutive runs of about 132 image pairs each. To ensure that the number of image pairs acquired was adequate, the running time average of the spatially-averaged velocity of each image pair was calculated.

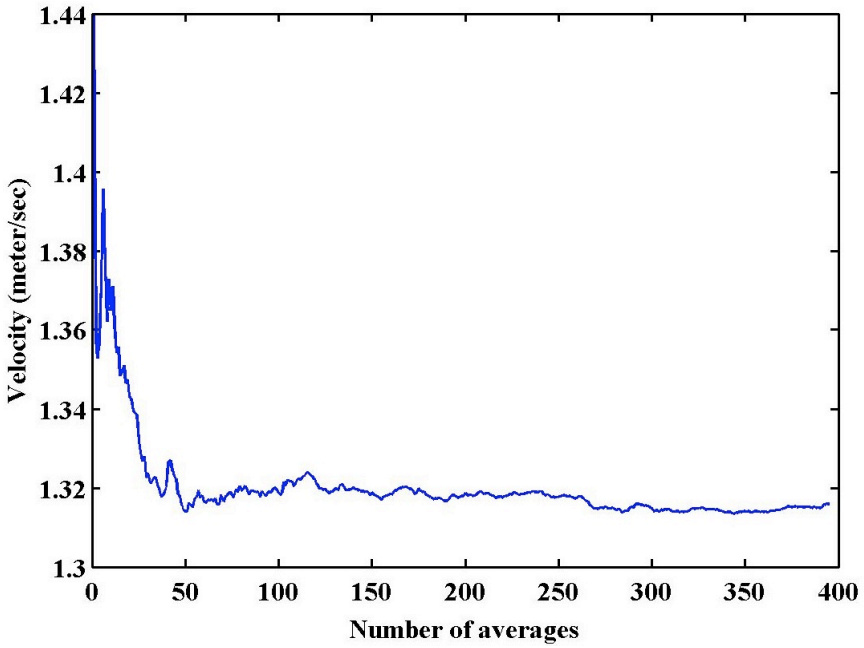


**Figure A2.1 Running average of the velocity for the DC-powered fan in plane 1**

Figure A2.1 shows a typical running average from plane 1 of the DC-powered fan. This graph shows the convergence of the running time average. The quick convergence and the steadiness of the running average for a number of averages shows

that the number of image pairs used was adequate. Similar results are found in Figure A2.2 for plane 2 of the DC-powered fan.

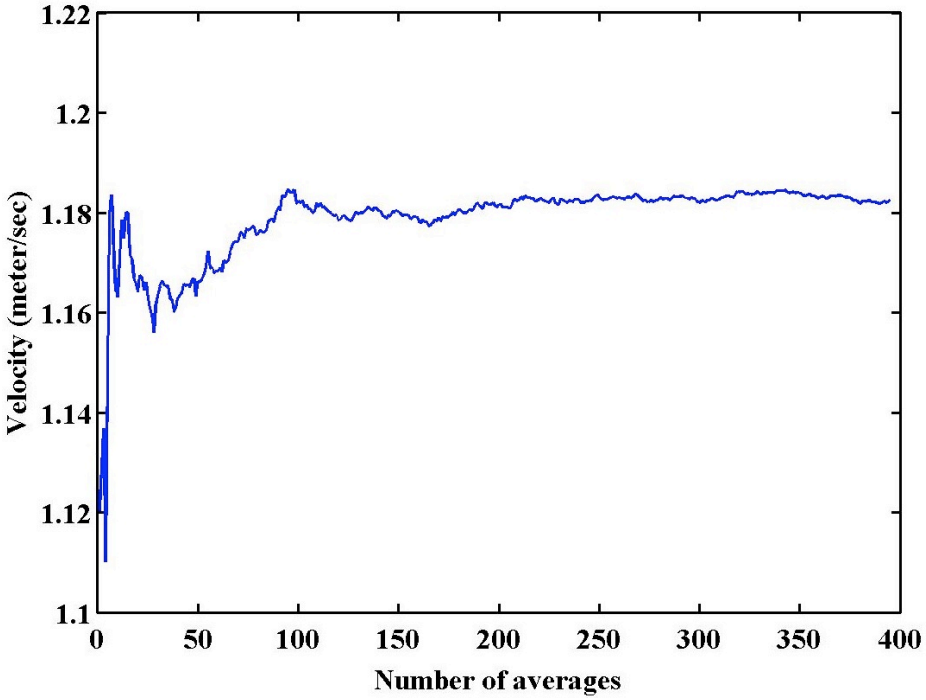


**Figure A2.2 Running average of the velocity for the DC-powered fan in plane 2**

The PWM-powered fan had a much higher spatially-averaged velocity. This was expected because the PWM-powered fan did not have an obstruction. The same convergence of the spatially-averaged velocity is also found for the PWM-powered fan as is seen in Figures A2.3 and A2.4. This analysis was done for all configurations and similar results were found for all of the experimental conditions used.

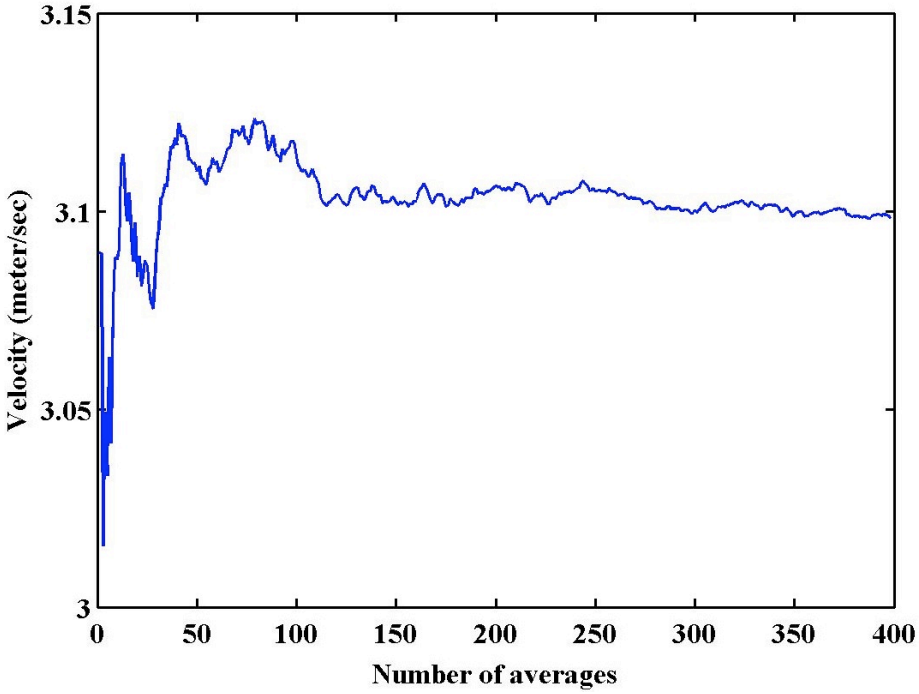


**Figure A2.3 Running average of the velocity for the PWM-powered fan in plane 1**

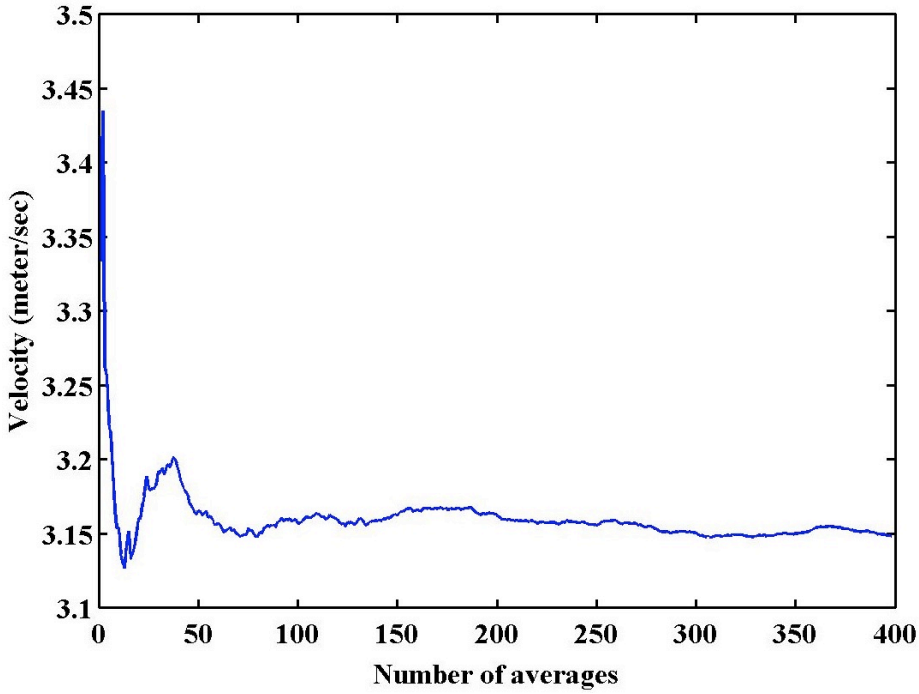


**Figure A2.4 Running average of the velocity for the PWM-powered fan in plane 2**